UNIVERSITY OF NEBR.
LIBRARY

OCT 25 1948

JOURNAL OF THE AERONAUTICAL SCIENCES

VOLUME 15 OCTOBER, 1948 NUMBER 10

CONTENTS

Wind-Tunnel Testing Problems in Superaerodynamics ..... HSUE-SHEN TSIEN 573

Primary Instability of Open-Section Stringers Attached to Sheet ..... SAMUEL LEVY AND WILHELMINA D. KROLL 581

Transient Loading of Airfoils at Supersonic Speeds ..... JOHN W. MILES 592

Plastic Flow Characteristics of Aluminum-Alloy Plate ..... L. J. KLINGLER AND G. SACHS 599

Full-Scale Free-Flight Ballistic Measurements of Guided Missiles ..... L. A. DELSASSO, L. G. DE BEY, AND D. REUYL 605

The Optimum Proportions of a Long Unstiffened Circular Cylinder in Pure Bending ..... HERBERT BECKER 616

The Relative Merits of Rotary Compressors ..... D. G. SAMARAS AND R. A. TYLER 625

Letter to the Editor 615

Published by the
INSTITUTE OF THE AERONAUTICAL SCIENCES, INC.

JOURNAL OF THE AERONAUTICAL SCIENCES

Editor: HUGH L. DRYDEN, *Director of Aeronautical Research, N.A.C.A.*

Associate Editor: ROBERT R. DEXTER *Associate Editor:* BERNEICE H. JARCK

The Institute of the Aeronautical Sciences publishes monthly the JOURNAL OF THE AERONAUTICAL SCIENCES and the AERONAUTICAL ENGINEERING REVIEW.

The JOURNAL OF THE AERONAUTICAL SCIENCES prints papers of scientific and technical interest to Institute members and subscribers. In general, it provides an opportunity for specialists to publish articles disclosing new knowledge and new applications in the field of the aeronautical sciences. The JOURNAL restricts itself to the aeronautical aspects of advances in science and engineering, and papers printed have either been submitted directly to the JOURNAL or have been previously presented at a meeting of the Institute.

The AERONAUTICAL ENGINEERING REVIEW keeps members and subscribers informed regarding the contents of new books and current periodicals in the field of aeronautics. It reviews new developments in the aircraft industry and reports on progress from house organs and catalogs published by aircraft and engine manufacturers and other companies engaged in aeronautical activities. It publishes papers on applied engineering and aircraft production. News of Institute activities is published in the REVIEW.

Statements and opinions expressed in the JOURNAL are to be understood as individual expressions of the authors and not those of the Institute.

SUBSCRIPTION RATES

Journal of the Aeronautical Sciences
Published Monthly

United States and Possessions		Foreign Countries Including Canada (American Currency Rates)	
1 Year	$12.00	1 Year	$13.00
Single Copies	1.50	Single Copies	1.50

Aeronautical Engineering Review
Published Monthly

United States and Possessions		Foreign Countries Including Canada (American Currency Rates)	
1 Year	$3.00	1 Year	$3.50
Single Copies	0.50	Single Copies	0.50

Notices of change of address should be sent to the Institute at least 30 days prior to actual change of address.

Manuscripts for publication, proofs, and all correspondence should be addressed to the Editorial Office of the JOURNAL.

Correspondence regarding subscriptions may be addressed to Publication Office, 20th and Northampton Sts., Easton, Pa., or to the Editorial Office of the JOURNAL OF THE AERONAUTICAL SCIENCES, 2 East 64th Street, New York 21, New York.

Copyright, 1948, by the Institute of the Aeronautical Sciences, Inc.

Entered as Second Class Matter at the Post Office, Easton, Pa., May 1, 1937. Acceptance for mailing at a special rate of Postage provided for in the Act of August 24, 1912. Authorized April 29, 1937.

INSTITUTE of the AERONAUTICAL SCIENCES

President
JOHN K. NORTHROP

Vice-Presidents
SMITH J. DE FRANCE
C. L. JOHNSON
R. P. LANSING
EARL D. OSBORN

Director
S. PAUL JOHNSTON

Executive Vice-President
BENNETT H. HORCHLER

Past-Presidents
J. C. HUNSAKER
CHARLES L. LAWRANCE
DONALD W. DOUGLAS
GLENN L. MARTIN
CLARK B. MILLIKAN
T. P. WRIGHT
GEORGE W. LEWIS (Deceased)
JAMES H. DOOLITTLE
FRANK W. CALDWELL
HALL L. HIBBARD
HUGH L. DRYDEN
R. H. FLEET
CHARLES H. COLVIN
ARTHUR E. RAYMOND
P. R. BASSETT

Secretary
ROBERT R. DEXTER

Treasurer
SHERMAN M. FAIRCHILD

Controller
JOSEPH J. MAITAN

Counsel
ALLAN D. EMIL

COUNCIL

E. E. ALDRIN
REX B. BEISEL
LAWRENCE D. BELL
WILLIAM BOLLAY
W. A. M. BURDEN
VICTOR E. CARBONARA
FRANK O. CARROLL
CHARLES H. COLVIN
JAMES H. DOOLITTLE
C. C. FURNAS
LEROY R. GRUMMAN
J. A. HERLIHY
JEROME LEDERER
JOHN C. LESLIE
JACK MASON
C. KENNETH RAZAK
L. B. RICHARDSON
RUSSELL G. ROBINSON
GEORGE S. SCHAIRER
ERNEST G. STOUT
A. J. THIEBLOT

ADVISORY COMMITTEE

WALTER BEECH
FRANK W. CALDWELL
RALPH S. DAMON
KENNETH S. M. DAVIDSON
R. H. FLEET
R. PAUL HARRINGTON
R. M. HAZEN
HALL L. HIBBARD
J. C. HUNSAKER
TH. VON KÁRMÁN
THOMAS A. KNOWLES
I. M. LADDON
GROVER LOENING
GLENN L. MARTIN
CLARK B. MILLIKAN
THOMAS A. MORGAN
ARTHUR E. RAYMOND
F. W. REICHELDERFER
LAURANCE S. ROCKEFELLER
T. CLAUDE RYAN
ELMER A. SPERRY, JR.
EDWARD P. WARNER
BURDETTE S. WRIGHT
T. P. WRIGHT

HONORARY MEMBERS

JOHN R. ALISON
JOHN N. BROWN
FRANK O. CARROLL
R. U. CONDON
L. C. CRAIGIE
DONALD B. DUNCAN
HARRY F. GUGGENHEIM
GEORGE C. KENNEY
THEODORE LONNQUEST
JOSEPH J. O'CONNELL, JR.
HOWARD T. ORVILLE
GEORGE B. PEGRAM
E. M. POWERS
ALFRED M. PRIDE
J. LAURENCE PRITCHARD
F. W. REICHELDERFER
DELOS W. RENTZEL
CARL SPAATZ
W. STUART SYMINGTON
J. W. TICE
HOYT S. VANDENBERG

HONORARY FELLOWS

H. H. ARNOLD
FRANK W. CALDWELL
SIR GEOFFREY DE HAVILLAND
JAMES H. DOOLITTLE
DONALD W. DOUGLAS
HUGH L. DRYDEN
W. F. DURAND
SIR RICHARD FAIREY
SIR ROY FEDDEN
J. C. HUNSAKER
SIR MELVILL JONES
GLENN L. MARTIN
GEORGE J. MEAD
SIR FREDERICK HANDLEY PAGE
D. R. PYE
IGOR I. SIKORSKY
SIR GEOFFREY TAYLOR
TH. VON KÁRMÁN
EDWARD P. WARNER
T. P. WRIGHT

BENEFACTORS

E. E. ALDRIN
HART O. BERG (Deceased)
W. A. M. BURDEN
E. L. CORD
DONALD W. DOUGLAS
SHERMAN M. FAIRCHILD
SIR RICHARD FAIREY
R. H. FLEET
FLORENCE GUGGENHEIM (Deceased)
C. D. HASCOM
JOHN P. V. HEINMULLER
ALEXANDER KLEMIN
PAUL KOLLSMAN
BELLA C. LANDAUER
WILLIAM LANDAUER
GROVER LOENING
EDMUND C. LYNCH (Deceased)
F. W. MAGIN
GLENN L. MARTIN
GEORGE J. MEAD
S. A. REED (Deceased)
LAURANCE S. ROCKEFELLER
EDWARD P. WARNER

AMERICAN FELLOWS

IRA H. ABBOTT
JOHN D. ACKERMAN
E. E. ALDRIN
HARRY G. ARMSTRONG
KARL ARNSTEIN
J. L. ATWOOD
PAUL S. BAKER
RALPH S. BARNABY
P. R. BASSETT
WELLWOOD E. BEALL
REX B. BEISEL
G. M. BELLANCA
DON R. BERLIN
HENRY A. BERLINER
WILLIAM BOLLAY
GEORGE W. BRADY
LYMAN J. BRIGGS
W. G. BROMBACHER
WILLIAM G. BROWN
CHARLES P. BURGESS
KENNETH CAMPBELL
CHARLES H. CHATFIELD
ALLAN CHILTON
FRANKLIN R. COLLBOHM
CHARLES H. COLVIN
KARL T. COMPTON
EMERSON W. CONLON
JOHN W. CROWLEY, JR.
RALPH S. DAMON
LUIS DE FLOREZ
SMITH J. DE FRANCE
J. P. DEN HARTOG
WALTER S. DIEHL
C. S. DRAPER
IVAN H. DRIGGS
WILLIAM K. EBEL
C. L. EGTVEDT
FREDERIC FLADER
CHARLES FROESCH
JACK FRYE
GARLAND FULTON
LESTER D. GARDNER
RICHARD C. GAZLEY
MICHAEL E. GLUHAREFF
MELVIN N. GOUGH
LEROY R. GRUMMAN
HAROLD R. HARRIS
R. M. HAZEN
EDWARD H. HEINEMANN
S. D. HERON
HALL L. HIBBARD
L. S. HOBBS
PAUL E. HOVGAARD
WILLIAM HOVGAARD
ROBERT INSLEY
EASTMAN N. JACOBS
C. L. JOHNSON
S. PAUL JOHNSTON
ALEXANDER KARTVELI
PAUL H. KEMMER
CARLETON KEMPER
J. H. KINDELBERGER
OTTO E. KIRCHNER
ARTHUR L. KLEIN
ALEXANDER KLEMIN
W. B. KLEMPERER
PAUL KOLLSMAN
OTTO C. KOPPEN
B. V. KORVIN-KROUKOVSKY
S. M. KRAUS
ARNOLD M. KUETHE
I. M. LADDON
E. S. LAND
CHARLES L. LAWRANCE
JEROME LEDERER
JOHN G. LEE
JOHN C. LESLIE
CHARLES A. LINDBERGH
WILLIAM LITTLEWOOD
GROVER LOENING
ALBERT E. LOMBARD
F. A. LOUDEN
W. RANDOLPH LOVELACE, II
EUGENE E. LUNDQUIST
R. D. MACCART
JOHN R. MARKHAM
ERLE MARTIN
WM. H. MCAVOY
C. J. MCCARTHY
J. S. MCDONNELL
CLARK B. MILLIKAN
ROBERT J. MINSHALL
JOSEPH S. NEWELL
ALFRED S. NILES
JOHN K. NORTHROP
ARTHUR NUTT
SHATSWELL OBER
ROBERT R. OSBORN
W. BAILEY OSWALD
GEORGE A. PAGE, JR.
F. W. PAWLOWSKI
F. W. PENNOYER, JR.
A. A. PRIESTER
ARTHUR E. RAYMOND
F. W. REICHELDERFER
ELLIOTT G. REID
H. J. E. REID
H. C. RICHARDSON
L. B. RICHARDSON
RUSSELL G. ROBINSON
LEONARD E. ROOT
C. E. ROSENDAHL
ADDISON M. ROTHROCK
W. R. SEARS
WILLIAM T. SCHWENDLER
FRANCIS R. SHANLEY
JAMES M. SHOEMAKER
IGOR ALEXIS SIKORSKY
ABE SILVERSTEIN
SELDEN B. SPANGLER
ELMER A. SPERRY, JR.
JOHN STACK
ROBERT M. STANLEY
WILLIAM B. STOUT
HARRY A. SUTTON
C. FAYETTE TAYLOR
EDWARD S. TAYLOR
PHILIP B. TAYLOR
TH. THEODORSEN
T. E. TILLINGHAST
S. TIMOSHENKO
L. B. TUCKERMAN
RALPH H. UPSON
J. PARKER VAN ZANDT
J. G. VINCENT
RICHARD VON MISES
FRANK L. WATTENDORF
P. V. H. WEEMS
FRED E. WEICK
R. D. WEYERBACHER
JOHN B. WHEATLEY
ANDREW V. WILLGOOS
DONALD H. WOOD
ROBERT J. WOODS
JOHN E. YOUNGER
ALBERT F. ZAHM
STEPHEN J. ZAND

Corporate Members

of the

Institute of the Aeronautical Sciences

Academy of Aeronautics, Inc.
Casey Jones School of Aeronautics

Aerojet Engineering Corporation

Aeroproducts Division, General Motors Corporation

Aeroquip Corporation

Agawam Aircraft Products, Inc.

Airborne Instruments Laboratory, Inc.

Airchox Company Division, Joyce Aviation, Inc.

Aircraft Radio Corporation

AiResearch Manufacturing Company, Division of The Garrett Corporation

Allis-Chalmers Manufacturing Company

Allison Division, General Motors Corporation

Aluminum Company of America

American Airlines System

American Bosch Corporation

American Overseas Airlines, Inc.
Iceland Airport Corporation (Subsidiary)

American Phenolic Corporation

Associated Aviation Underwriters

Atlas Supply Company

Beech Aircraft Corporation

Bell Aircraft Corporation

Bendix Aviation Corporation
Bendix International Division
Bendix Products Division
Bendix Radio Corporation
Eclipse-Pioneer Division
Friez Instrument Division
Pacific Division
Scintilla Magneto Company

The BG Corporation

Boeing Airplane Company
Seattle Division
Wichita Division

Breeze Corporations, Inc.
Aircraft Standard Parts Company, Inc.
Aldrich Company
Anderson Stove Company, Inc.
Federal Laboratories, Inc.
Foundry Service, Inc.

Cal-Aero Technical Institute, A Division of Grand Central Airport Company

Canadair, Ltd.

Cessna Aircraft Company

Chandler-Evans Division, Niles-Bement-Pond Company

Chase Aircraft Company, Inc.

Chase National Bank of the City of New York

The Cleveland Graphite Bronze Company

The Cleveland Pneumatic Tool Company
Automotive-Aircraft Division

Clifford Manufacturing Company, Division of Standard-Thomson Corporation

Consolidated Vultee Aircraft Corporation
Fort Worth Division
Stinson Aircraft Division

Continental Motors Corporation

Curtiss-Wright Corporation
Airplane Division
Propeller Division
Wright Aeronautical Corporation Division

Doak Aircraft Company, Inc.

Douglas Aircraft Company, Inc.
El Segundo Plant
Long Beach Plant
Santa Monica Plant

The Dow Chemical Company

Dzus Fastener Company, Inc.

Eastern Air Lines, Inc.

Eaton Manufacturing Company
Dynamatic Corporation (Subsidiary)
Eaton-Wilcox-Rich Ltd. (Subsidiary)

Thomas A. Edison, Incorporated, Instrument Division

Edo Corporation

Elastic Stop Nut Corporation of America

Electrol Incorporated

Ethyl Corporation

Fairchild Camera & Instrument Corporation
Fairchild Aerial Surveys, Inc.

Fairchild Engine and Airplane Corporation
Al-Fin Division
Fairchild Aircraft Division
Fairchild Personal Planes Division
Fairchild Pilotless Plane Division
NEPA Division
Ranger Aircraft Engines Division
Stratos Corporation (Subsidiary)

Federal Telephone and Radio Corporation
Federal Electric Manufacturing Company, Ltd.
Federal Telecommunication Laboratories, Inc. (Partial Subsidiary)

General Electric Company
Aircraft Gas Turbine Division
Aviation Divisions

General Tire and Rubber Company of California, Research and Development Division

The B. F. Goodrich Company

The Goodyear Tire & Rubber Company
Goodyear Aircraft Corporation

Grumman Aircraft Engineering Corporation

W. & L. E. Gurley

The International Nickel Company, Inc.

Irving Air Chute Company, Inc.

Jack & Heintz Precision Industries, Inc.

Johns-Manville Sales Corporation

Walter Kidde & Company, Inc.

Kollsman Instrument Division, Square D Company

Lavelle Aircraft Corporation

Lear Incorporated

Link Aviation, Inc.

The Liquidometer Corporation

Lockheed Aircraft Corporation
Airquipment Company (Subsidiary)
Lockheed Air Terminal (Subsidiary)
Lockheed Aircraft Overseas Corporation (Subsidiary)
Lockheed Aircraft Service, Inc. (Subsidiary)

Longines-Wittnauer Watch Company, Inc.

The Glenn L. Martin Company
GLM Chemical Division
Rotawings Division

Warren McArthur Corporation

McDonnell Aircraft Corporation

Minneapolis-Honeywell Regulator Company
Brown Instrument Company (Subsidiary)

Moore Drop Forging Company

National City Bank of New York

National Credit Office, Inc.

North American Aviation, Inc.
North American Aviation, Inc., of Texas

Northrop Aircraft, Inc.

Northwest Airlines, Inc.

Owens-Corning Fiberglas Corporation

Pan American World Airways System

The Parker Appliance Company

Pesco Products Division, Borg-Warner Corporation

Phillips Petroleum Company

Pure Oil Company

Radioplane Company

Republic Aviation Corporation

A. V. Roe Canada Limited

John A. Roebling's Sons Company

Rohr Aircraft Corporation

Ryan Aeronautical Company

Shell Oil Company, Inc.

Simmonds Aerocessories, Inc.

Socony-Vacuum Oil Company, Inc.

Solar Aircraft Company

Sperry Gyroscope Company Division of The Sperry Corporation

Square D Company

Standard Oil Company of California

Standard Oil Company (Indiana)

Standard Oil Company of New Jersey

The Texas Company

Thompson Products, Inc.

Tinnerman Products, Inc.

Union Carbide and Carbon Corporation
Bakelite Corporation
Electro Metallurgical Company
Haynes Stellite Company
The Linde Air Products Company
National Carbon Company, Inc.

United Air Lines, Inc.

United Aircraft Corporation
Chance Vought Aircraft Division
Hamilton Standard Propellers Division
Pratt & Whitney Aircraft Division
Sikorsky Aircraft Division
United Aircraft Export Corporation
United Aircraft Service Corporation

United States Aviation Underwriters, Inc.

United States Rubber Company
Dominion Rubber Company, Ltd.

Vickers, Inc.

Warner Aircraft Corporation

The Weatherhead Company
Angola, Indiana Division
Columbia Products Division
Houma Division
The Weatherhead Company of Canada (Subsidiary)

Westinghouse Electric Corporation
Aviation Gas Turbine Division
Industrial Electronics Division
Marine & Aviation Sales Department
Small Motor Division, Aviation Sales

Weston Electrical Instrument Corporation

Wyman-Gordon Company

Young Radiator Company

EDITORIAL COMMITTEE

HUGH L. DRYDEN, *Chairman*

Aerodynamics

Francis Clauser
Howard Emmons
R. Paul Harrington
R. T. Jones
W. B. Klemperer
Otto C. Koppen
John G. Lee
H. P. Liepmann
C. C. Lin
H. F. Ludloff
John R. Markham
Clark B. Millikan
Shatswell Ober
W. Bailey Oswald
Allen E. Puckett
Elliott G. Reid
H. J. E. Reid
Russell Robinson
L. E. Root
G. B. Schubauer
W. R. Sears
John Stack
Th. von Kármán
Richard von Mises

Air Transport

A. W. Dallas
Charles Froesch
J. A. Herlihy
Otto E. Kirchner
John C. Leslie

Aircraft Design

W. E. Beall
Rex B. Beisel
W. K. Ebel
Hall L. Hibbard
C. L. Johnson
I. M. Laddon
C. J. McCarthy
Fred E. Weick
Robert J. Woods

Physiologic Problems

H. G. Armstrong
Louis H. Bauer
Eugene Du Bois
W. Randolph Lovelace, II
Ross A. McFarland
A. D. Tuttle

Aircraft Propulsion

George W. Brady
Frank W. Caldwell
L. S. Hobbs
E. E. Johnson
Joseph Keenan
R. P. Kroon
Arthur Nutt
Hans Reissner
Abe Silverstein
C. Fayette Taylor
E. S. Taylor
P. Taylor

Structures and Materials

W. B. Bleakney
E. W. Conlon
J. P. Den Hartog
L. H. Donnell
E. C. Hartmann
N. J. Hoff
E. E. Lundquist
C. F. Nagel, Jr.
J. S. Newell
Alfred S. Niles
W. Ramberg
E. Reissner
F. R. Shanley
H. W. Sibert
C. R. Strang
S. Timoshenko
H. S. Tsien
Chi-Teh Wang

Meteorology

C. F. Brooks
D. M. Little
E. J. Minser
F. W. Reichelderfer
H. C. Willett

Fuels and Oils

A. L. Beall
J. H. Doolittle
Graham Edgar
R. T. Goodwin
S. D. Heron
A. M. Rothrock

Instruments

Allan G. Binnie
W. G. Brombacher
J. Callahan
Charles H. Colvin
C. S. Draper
O. E. Esval
David W. Moore
W. A. Reichel
C. F. Savage
O. Hugo Schuck
R. Sylvander

Rotating Wing Aircraft

Robert Coleman
K. H. Hohenemser
G. Horvay
Alexander Klemin
Ralph McClarren
R. H. Miller
R. H. Prewitt
Igor I. Sikorsky
Robert A. Wolf

Vibration and Flutter

Lee Arnold
M. A. Biot
William Bollay
Chieh-Chien Chang
J. P. Den Hartog
Manfred Rauscher

Flight Testing

W. K. Ebel
R. R. Gilruth
Melvin N. Gough
Robert Stanley
E. G. Stout

I.A.S. REPRESENTATIVES TO OTHER ORGANIZATIONS

Aircraft Industries Association of America, Inc.—CHARLES MARCUS

American Association for the Advancement of Science—J. C. HUNSAKER

American Society of Mechanical Engineers—CHARLES H. COLVIN

American Standards Association—P. R. BASSETT

Engineering Society of Detroit—DONALD C. HUNT, GEORGE TWENEY

Greater New York Safety Council—WILLIAM LITTLEWOOD

Daniel Guggenheim Medal Board of Award—PRESTON R. BASSETT, GROVER LOENING, S. PAUL JOHNSTON

Institute of Radio Engineers—L. M. HULL

Manufacturers Aircraft Association—ARTHUR E. RAYMOND

National Aeronautic Association—WILLIAM R. ENYART

National Fire Protection Association—E. E. ALDRIN

National Research Council Engineering Division—HUGH L. DRYDEN

National Safety Council—JEROME LEDERER

New York Museum of Science and Industry—LESTER D. GARDNER

Society of Automotive Engineers—STEPHEN J. ZAND

JOURNAL OF THE AERONAUTICAL SCIENCES

VOLUME 15 OCTOBER, 1948 NUMBER 10

Wind-Tunnel Testing Problems in Superaerodynamics

HSUE-SHEN TSIEN*

Massachusetts Institute of Technology

SUMMARY

The problems in the experimentation of rarefied gas are discussed. First, the extremely large viscous effects in a wind-tunnel nozzle are shown. Then the difficulties of flow measurement are surveyed, pointing out particularly the unconventional behavior of the Pitot tube in rarefied gas. The performance of a hot-wire anemometer is then studied in some detail to show its feasibility. Finally, the rules for achieving complete flow similarity of rarefied gas flow are formulated.

INTRODUCTION

WIND TUNNELS ARE, perhaps, the most useful tool in aerodynamic investigations and certainly have contributed much in the modern development of fluid mechanics. It is thus natural, when one turns to a new field of aerodynamics, the aerodynamics of rarefied gases or superaerodynamics, that one should think of using the wind tunnel again. Only here it has to be adapted to entirely new circumstances, and many new problems, both in its design and in its operation, appear. It is the purpose of this paper to discuss some of these problems so as to gain an orientation in the new field of experimentation.

(1) TUNNEL DESIGN

To test models in the wind tunnel at its test section, it is of primary importance to obtain a uniform stream at the desired temperature, pressure, and velocity. For subsonic wind tunnels with ordinary pressures, this can be achieved without much difficulty. For supersonic wind tunnels at ordinary pressure, the expansion part of the tunnel before the test section or the nozzle is first designed to obtain a uniform stream at its exit without considering the effects of the viscosity of air. Then the boundary layer along the wall of the nozzle is calculated with the pressure gradient thus determined. Finally, the displacement thickness of the boundary layer, or the needed space for the boundary layer flow at lower velocity, is provided by making the nozzle larger than the dimensions first determined by the calculated amount.[1] This design procedure is found to give satisfactory nozzles for supersonic wind tunnels.

However when one tries to apply the same design procedure to the superaerodynamics wind tunnel, one is immediately confronted with the difficulty of extremely large viscous effect. In other words, the boundary layer will be so thick as to occupy the main portion of the nozzle passage. To demonstrate this effect, let the length of the test section be L and the width of the square test section be b. Then the Reynolds Number based upon the conditions in the test section is $Re = UL/\nu$, where U is the velocity in the test section. If, as a rough estimate, we take the thickness of the boundary layer to be zero at the beginning of the test section and equal to a value δ calculated by the well-known Blasius formula for a flat plate at the end of the test section, then

$$\delta = 3.65L/\sqrt{Re} \tag{1}$$

Now, if this boundary layer actually occupies half the tunnel width $b/2$, then

$$\delta = b/2 = 3.65L/\sqrt{Re} \tag{2}$$

On the other hand, the ratio of the mean free path l and the boundary-layer thickness δ is known[2] to be

$$l/\delta = (1.255\sqrt{\gamma}/3.65)(M/\sqrt{Re}) \tag{3}$$

where γ is the ratio of specific heats and can be taken as 1.4 and M is the Mach Number in the test section. By

Presented at the Session on Aerodynamics of the Upper Atmosphere, Sixteenth Annual Meeting, I.A.S., New York, January 26–29, 1948.

* Professor of Aerodynamics, Guggenheim Aeronautical Laboratory.

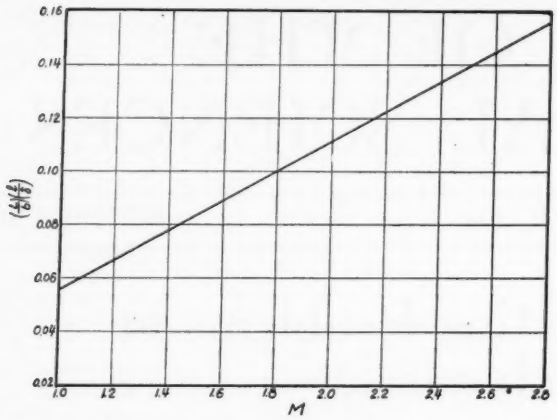

FIG. 1. l, mean free path; δ, boundary layer thickness at end of the test section of width b and length L; and M, Mach Number of the test section.

combining Eqs. (2) and (3), we have

$$(l/\delta)(L/b) = 0.0557M \tag{4}$$

This relation is shown in Fig. 1. Thus for a Mach Number M equal to 2 and $L/b = 2$, the boundary layer will completely fill up the test section, if the mean free path is equal to 5.6 per cent of the boundary-layer thickness or 2.8 per cent of the tunnel width. This means that the extremely strong viscous effect at low densities makes the ordinary concept of designing a wind tunnel totally inapplicable.

The extremely thick boundary layer where the velocity increases from a small value near the wall to some supersonic velocity at the center of the nozzle, also gives subsonic velocities in a rather large portion of the nozzle. Since pressure disturbances downstream can be transmitted upstream in subsonic flows, the flow in the test section of a low-pressure tunnel will be sensitive to changes in the diffuser even if the main stream velocity at the center of the nozzle is supersonic. This is, of course, a new phenomenon in the superaerodynamics tunnel not found in conventional supersonic wind tunnels.

The large viscous effects can also be demonstrated by calculating the ratio of frictional loss on the walls of the test section and the shock loss in the diffuser after the test section. Consider the diffuser to be a straight tube of approximately the same cross-sectional area as the test section, then the pressure loss due to friction, Δp_1, is

$$\begin{aligned}\Delta p_1 &= \text{frictional force}/b^2 \\ &= (\rho U^2/2)4bLC_f(1/b^2)\end{aligned}$$

Taking C_f to be the Blasius value or $C_f = 1.328/\sqrt{Re}$, we have

$$\Delta p_1 = 2\rho U^2(L/b)(1.328/\sqrt{Re}) \tag{5}$$

Now, if p is the static pressure in the test section, then the pressure for ideal isentropic compression in the diffuser is

$$p\{1 + [(\gamma - 1)/2]M^2\}^{\gamma/(\gamma-1)}$$

If the actual pressure rise in the diffuser is estimated as that due to a normal shock without further recovery, then the actual pressure rise is

$$\{[2\gamma/(\gamma + 1)]M^2 - [(\gamma - 1)/(\gamma + 1)]\}p$$

Therefore, the pressure loss due to shock Δp_2 is

$$\Delta p_2 = \left[\left(1 + \frac{\gamma - 1}{2}M^2\right)^{\gamma/(\gamma-1)} - \left(\frac{2\gamma}{\gamma + 1}M^2 - \frac{\gamma - 1}{\gamma + 1}\right)\right]p \tag{6}$$

By combining Eqs. (5) and (6), the ratio of these two pressure losses is

$$\frac{\Delta p_1}{\Delta p_2} = \frac{2\gamma M^2(L/b)(1.328/\sqrt{Re})}{\left(1 + \frac{\gamma - 1}{2}M^2\right)^{\gamma/(\gamma-1)} - \left(\frac{2\gamma}{\gamma + 1}M^2 - \frac{\gamma - 1}{\gamma + 1}\right)} \tag{7}$$

Introducing the mean free path ratio given by Eq. (3), we have

$$\frac{\Delta p_1}{\Delta p_2} = \left(\frac{L}{b}\right)\left(\frac{l}{\delta}\right)\frac{6.528\gamma M}{\left(1 + \frac{\gamma - 1}{2}M^2\right)^{\gamma/(\gamma-1)} - \left(\frac{2\gamma}{\gamma+1}M^2 - \frac{\gamma-1}{\gamma+1}\right)} \tag{8}$$

This relation is plotted in Fig. 2. Therefore, if the Mach Number M is 2 and $L/b = 2$ as before, then, when the ratio (l/δ) is 0.056, the ratio of frictional loss to shock loss is 0.628. Hence, the frictional loss and the shock loss are of the same order of magnitude.

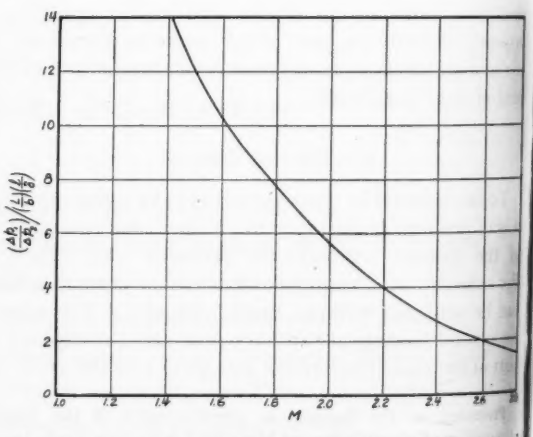

FIG. 2. l, mean free path; δ, boundary layer thickness at end of the test section of width b and length L; and M, Mach Number of the test section. Δp_1, pressure loss by friction; Δp_2, pressure loss by shock.

These large viscous effects are fully confirmed by the recent tests on the 1 by 1-in. low-pressure wind tunnel at the University of California.* The test nozzle (Fig. 3) was designed for Mach Number 4 without considering the viscous effect of the medium. During test, the static pressure on the wall at the exit of the nozzle is measured. This pressure is equal to 175 and 68 microns† for the two tests presented in Figs. 4 and 5. The apparent Mach Number M is the Mach Number calculated from the dynamic pressure measured by a Pitot tube by using the Rayleigh formula. Since there is the complication of large viscous effect in the Pitot tube reading as shown in the following section, this apparent Mach Number is only qualitative and cannot be taken as the exact value. However it is apparent from Figs. 4 and 5 that the boundary layer in the test section is indeed extremely thick and fills up the whole space. This large boundary-layer thickness makes the space available for the expansion of the central potential flow very small, if it exists at all. Therefore, the maximum Mach Number reached at the center of the nozzle is much smaller than the design Mach Number of 4. At the lower pressure, the influence of slip at the wall is also evident. This has the tendency to make the flow more uniform. However, the extremely low Mach Number at the test section indicates again the strong viscous effect in converting much of the pressure energy into heat energy.

These elementary calculations and preliminary test results make it clear that, for the design of the nozzle and test section for a superaerodynamics wind tunnel, it is no longer possible to separate the compressibility

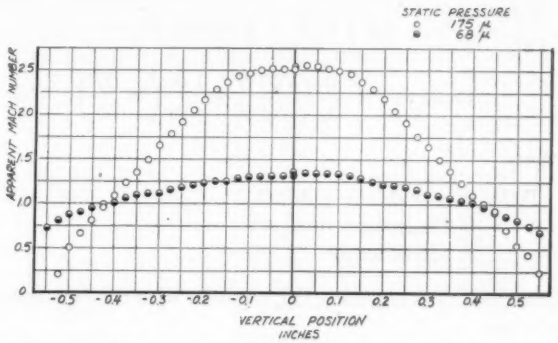

FIG. 4. Vertical velocity distribution in test section of University of California Low Pressure Wind Tunnel No. 2.

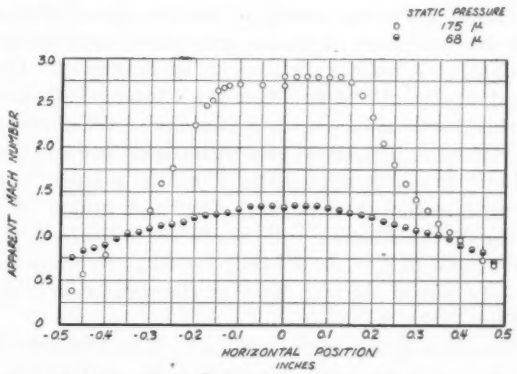

FIG. 5. Horizontal velocity distribution in test section of University of California Low Pressure Wind Tunnel No. 2.

effect and the viscous effect. In fact, the concept of boundary layer is also of doubtful value because of the extremely small Reynolds Number encountered. Therefore, to design such a nozzle to obtain the nearest approximation to the ideal uniform flow, it will be necessary to use the exact Navier-Stokes equations instead of the approximate boundary-layer equations. Of course, it may be argued that for superaerodynamics the Navier-Stokes equations are no longer exact and that additional corrections must be added.[2] However, recent investigations by Schamberg[3] have shown that these additional corrections are small in the case of the slip flows concerned here and will not essentially alter the flow pattern. Hence, for a first approximation just like the nonviscous isentropic flow is a first approximation for ordinary supersonic nozzles, we can use the Navier-Stokes equations. The simplest case to be considered is certainly the axially symmetric nozzles. If x is the coordinate in the axial direction, r is the coordinate in the radial direction, and u and v are the corresponding velocity components, the equations are:

$$(\partial \rho u/\partial x) + (1/r)(\partial/\partial r)(\rho r v) = 0 \qquad (9)$$

$$\rho(Du/Dt) = -(\partial p/\partial x) + (\text{Grad } \tau)_x \qquad (10)$$

$$\rho(Dv/Dt) = -(\partial p/\partial_r) + (\text{Grad } \tau)_r \qquad (11)$$

* Experimental work done under contract with the Office of Naval Research. The author is deeply indebted to Profs. R. G. Folsom and E. D. Kane for permission to use their unpublished results.

† 1,000 microns = 1 mm. Hg; one atmosphere = 0.760×10^6 microns.

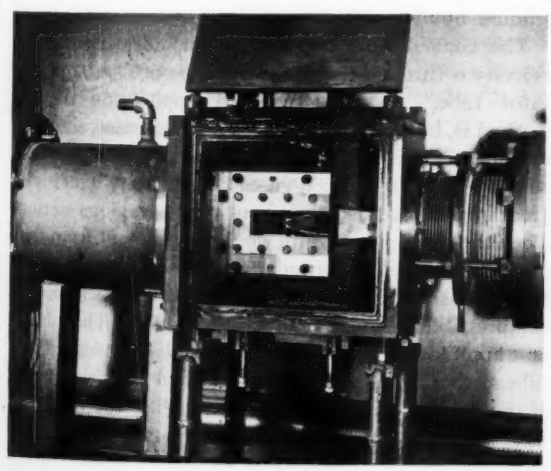

FIG. 3. Test section of University of California Low Pressure Wind Tunnel No. 2.

$$\rho \frac{D}{Dt}\left(\frac{u^2+v^2}{2} + c_pT\right) = \Phi - \{u(\text{Grad }\tau)_x + v(\text{Grad }\tau)_r\} + \frac{\partial}{\partial x}\left(\lambda \frac{\partial T}{\partial x}\right) + \frac{1}{r}\frac{\partial}{\partial r}\left(\lambda r \frac{\partial T}{\partial r}\right) \quad (12)$$

where

$D/Dt = u(\partial/\partial x) + v(\partial/\partial r)$
Φ = dissipation function
τ = stress tensor

Eqs. (9), (10), (11), and (12), together with the equation of state,

$$p/\rho = RT \quad (13)$$

then determine the five unknowns u, v, ρ, p, and T. Of course, the actual process of making this calculation will be extremely tedious, and some approximate method of solution may have to be developed. One possibility would be to adapt the Kármán-Polhausen method for boundary layer to this case: We integrate the differential equations once with respect to r and thus only try to satisfy the equations "on the average" over the cross section of the nozzle. The "distribution" of u, v over the cross section will then be set in the form of a polynomial in r. Initial study by this procedure has already been made by Schaaf[4] at the suggestion of the author.

For ordinary supersonic diffusers, high efficiency of pressure recovery can generally be achieved by using a long diffuser. However, for a superaerodynamic wind tunnel, because of the extremely large loss through friction, long diffusers are undesirable. In fact, the pressure loss can be reduced by using the shortest possible diffuser.

(2) Flow Measurement

The quantities that determine the flow field are two of the three variables p, ρ, and T and the velocity components. The quantities p, ρ, T are related by the equation of state, and therefore only two are necessary for the determination of all three. Generally, for wind-tunnel work, the quantities actually measured are p, ρ, and q, the magnitude of the velocity.

For the measurement of pressure, a manometer is used. For ordinary pressures, one uses a fluid manometer filled with water, alcohol, or mercury. However for the extremely low pressure encountered in the superaerodynamic flow, some other form of manometer is necessary. One of the most successful types is the Pirani gage. The conventional form of Pirani gage has a pressure sensitivity of about 10^{-2} micron. It utilizes the change of temperature of a wire heated with constant energy caused by a change in the pressure of the gas surrounding it. The temperature change is measured by the change in the resistance of the wire. The wire is located in a small chamber which is connected to the point of measurement by a hole, flush with the gas stream if static pressure is to be measured. The question of best design of the connecting tube for quick response has been studied by Schaaf.[5]

To measure the density ρ, the conventional method utilizes the difference in the velocity of light rays in mediums of different density. With different optical arrangements, we have the shadowgraph method, the schlieren method, and the interferometer method. However, if the density of the medium is low as in the case of superaerodynamic flow, the sensitivity of these methods becomes extremely poor. For instance in the case of the schlieren method, the percentage change in illumination I on passing through a region of thickness b is given by

$$\frac{\Delta I}{I} = k\frac{f}{e}\,0.000294\left(\frac{\rho}{\rho_0}\right)\left[\frac{b}{\rho}\frac{\Delta\rho}{\Delta n}\right] \quad (14)$$

where ρ_0 is the air density at 32°F. and 1 atmosphere pressure and where $\Delta\rho/\Delta n$ is the density gradient normal to the light ray. f and e are the focal length and the normal unobscured width of the light source image perpendicular to the knife edge. k is a factor of order 1, determined by the particular optical path used. Therefore the sensitivity of the schlieren method decreases in proportion to the factor (ρ/ρ_0). Some improvement can be made by altering the quantities f and e, but practical limitations and diffraction difficulties do not allow the increase of sensitivity to satisfactory values.

A new approach to this problem of density measurement is the method of absorption. It is found for instance, that oxygen at low pressures shows a strong absorption band at wave lengths around 1,470Å. or ultraviolet light. The percentage absorption is proportional to the number of molecules that meet the light ray and is, therefore, proportional to the density of the gas. The measurement is then similar to that of the interferometer method where the density is determined. A similar method is the utilization of the afterglow of nitrogen. These methods are now being studied by Evans.[6]

The conventional method for the measurement of velocity is through the use of dynamic pressure rise in a Pitot tube. A straightforward application of this method is, however, difficult for rarefied gases, since the formula used is based upon the neglect of viscosity effects. But for rarefied gases the viscosity effect is of great importance, as pointed out in the previous section. Then the dynamic pressure would be different from that given by the usual formula. To estimate this effect, let us consider the case of low Mach Number so that compressibility effects can be neglected. Then, as a first approximation, take the flow field around the Pitot tube as that of a source of strength S in nonviscous flow of uniform velocity U. The "radius" of the tube a is

$$a = \sqrt{S/\pi U}$$

and the stagnation point is located at

$$R = \sqrt{S/4\pi U} = a/2 \tag{15}$$

The velocity introduced by the source is then

$$-U(1/4)(a^2/R^2)$$

By calculating the viscous stress from this approximate disturbance velocity, we have, for flow along the axis,

$$u\frac{\partial u}{\partial r} + \frac{1}{\rho}\frac{\partial p}{\partial r} = \nu U a^2 \frac{1}{2}\frac{1}{r^4} \tag{16}$$

Hence, if p_0 is the stagnation pressure and p° is the static pressure,

$$p_0 - p^\circ = \frac{1}{2}\rho U^2 + \mu U a^2 \frac{1}{2}\int_\infty^R \frac{dr}{r^4} = \frac{1}{2}\rho U^2 - \frac{1}{2}\mu U\frac{a^2}{R^3}$$

or

$$p_0 - p^\circ = \frac{1}{2}\rho U^2\left(1 - \frac{8}{9\sqrt{3}}\frac{\nu}{aU}\right) \tag{17}$$

For rarefied gases, the value of ν/aU or the reciprocal of the Reynolds Number of the Pitot tube could be of the order of unity. Then the dynamic pressure rise $p_0 - p^\circ$ is not the usual value $^1/_2\rho U^2$ but a value much less than that. In fact, previous investigations by Barker[7] and Homann[8] indicate that the Reynolds Number $a'U/\nu$, where a' is the radius of the mouth of tube, must exceed 30 in order to reach the usual dynamic pressure rise $^1/_2\rho U^2$.

TABLE 1

The Functions F_1 and F_2 [cf. Eq. (21)]

U/c	F_1	F_2
0	1.77245	0
0.2	1.73751	0.07020
0.4	1.63880	0.27269
0.6	1.49248	0.58560
0.8	1.32021	0.97843
1.0	1.14328	1.42053
1.2	0.97825	1.88555
1.4	0.83480	2.35492
1.6	0.71628	2.81812
1.8	0.62153	3.27117
2.0	0.54683	3.71356
2.2	0.48790	4.14672
2.4	0.44090	4.57300
2.6	0.40268	4.99395
2.8	0.37100	5.41117
3.0	0.34420	5.87498

When the velocity of flow is high, we have an added complication due to the shock. The conventional Rayleigh formula for Pitot tubes in supersonic flow is based upon the assumption of a thin shock wave ahead of the Pitot tube. Now the thickness of the shock is proportional to the mean free path. Hence, in rarefied flows, the thickness of the shock will be so increased as to cause interference with flow in the neighborhood of the Pitot tube. This, together with the viscous effect mentioned in the previous paragraph, definitely shows the inapplicability of the Rayleigh formula for supersonic velocity of rarefied gases.

(3) Hot-Wire Anemometer

With the great complications in applying the conventional velocity-measuring device to superaerodynamic flows, one is naturally led to the thought of other avenues of approach. One possibility is the use of hot wires. If the wire diameter is of the order of 0.0001 in. and if the pressure of the gas stream is approximately 100 microns, the ratio of the mean free path to the wire diameter will be approximately 180. Therefore, the flow around the wire is definitely the free molecule flow.[2] Thus we have a simple physical situation, which is an improvement over the rather uncertain circumstances of mixed dynamic and viscous effects for the measurement of velocity by a Pitot tube. It therefore seems worth while to explore this possibility by a trial calculation of the performance of such a hot-wire anemometer.

If θ is the inclination of the solid surface to a gas stream that has a macroscopic velocity U and a Maxwellian molecular velocity distribution, the translational energy of molecules E_{tr} incident upon the unit area is

$$E_{tr} = \rho\frac{c}{2\sqrt{\pi}}\left\{e^{-(U/c)^2\sin^2\theta}\left(c^2 + \frac{1}{2}U^2\right) + \sqrt{\pi}\frac{U}{c}\sin\theta\left(\frac{5}{4}c^2 + \frac{1}{2}U^2\right)\left[1 + erf\left(\frac{U}{c}\sin\theta\right)\right]\right\} \tag{18}$$

where $c^2 = 2RT$, T is the temperature of the gas stream, and *erf* is the error function. Now let r be the radius of the hot wire. Then the total energy E_t incident upon a unit length of the wire is the sum of translational energy and internal energy. If c_v is the specific heat at constant volume, this total energy per unit length of wire is

$$E_t = \rho\frac{c}{\sqrt{\pi}}r\left\{\left[\frac{1}{2}U^2 + \left(\frac{1}{2}R + c_v\right)T\right]\int_{-\pi/2}^{\pi/2} e^{-(U/c)^2\sin^2\theta}\,d\theta + \sqrt{r}\left[\frac{1}{2}U^2 + (R + c_v)T\right]\int_{-\pi/2}^{\pi/2}\frac{U}{c}\sin\theta\left[1 + erf\left(\frac{U}{c}\sin\theta\right)\right]d\theta\right. \tag{19}$$

The integrals in Eq. (19) can be expressed in terms of tabulated functions (see Appendix). Thus,

$$E_i = \rho c r \left\{\left[\frac{1}{2}U^2 + \left(\frac{1}{2}R + c_v\right)T\right]F_1\left(\frac{U}{c}\right) + \left[\frac{1}{2}U^2 + (R + c_v)T\right]F_2\left(\frac{U}{c}\right)\right\} \tag{20}$$

where

$$F_1\left(\frac{U}{c}\right) = \frac{1}{\sqrt{\pi}}\int_{-\pi/2}^{\pi/2} e^{-(U^2/c^2)\sin^2\theta}\, d\theta = \sqrt{\pi}\, e^{-(1/2)(U/c)^2} I_0\left(\frac{1}{2}\frac{U^2}{c^2}\right) \tag{21}$$

$$F_2\left(\frac{U}{c}\right) = \int_{-\pi/2}^{\pi/2}\left(\frac{U}{c}\sin\theta\right)\left[1 + erf\left(\frac{U}{c}\sin\theta\right)\right]d\theta = \sqrt{\pi}\left(\frac{U}{c}\right)^2 e^{-(1/2)(U/c)^2}\left[I_0\left(\frac{1}{2}\frac{U^2}{c^2}\right) + I_1\left(\frac{1}{2}\frac{U^2}{c^2}\right)\right] \tag{22}$$

The I_0 and I_1 are the modified Bessel functions of the first kind of orders zero and one, respectively. The functions F_1 and F_2 are tabulated in Table 1.

If T_w is the wall temperature and α is the accommodation coefficient, the difference between the energy E_i incident upon the surface and the energy E_r carried by the molecules re-emitted from the surface is given by

$$E_i - E_r = \alpha(E_i - E_w)$$

where E_w is the energy that would be carried away by the molecules if the re-emission were at the temperature T_w of the wire. Therefore,

$$E_i - E_r = \alpha\rho c r\left\{\left[\frac{1}{2}U^2 + \left(\frac{1}{2}R + c_v\right)(T - T_w)\right]F_1\left(\frac{U}{c}\right) + \left[\frac{1}{2}U^2 + (R + c_v)(T - T_w)\right]F_2\left(\frac{U}{c}\right)\right\} \tag{23}$$

This difference of energy is then the net energy input to the wire per unit length of the wire by the air stream.

If i is the electric current heating the wire and Ω is the resistance of the wire per unit length at the wire temperature, the heat input per unit length of wire by the heating current is $i^2\Omega$. Heat is lost from the wire by radiation. If σ is Stefan-Boltzmann constant and ϵ is the emissivity of the wire surface, the radiation heat loss per unit length is $2\pi r\epsilon\sigma T_w^4$. Therefore, if the wire has reached a steady condition, the heat balance requires

$$\alpha\rho\sqrt{2RT}\, r\left\{F_1\left(\frac{U}{c}\right)\left[\frac{1}{2}U^2 + \left(\frac{1}{2}R + c_v\right)(T - T_w)\right] + F_2\left(\frac{U}{c}\right)\left[\frac{1}{2}U^2 + (R + c_v)(T - T_w)\right]\right\} + i^2\Omega = 2\pi r\epsilon\sigma T_w^4 \tag{24}$$

This equation can be put into somewhat simpler form by using the following relation:

$$R = c_p - c_v = c_v(\gamma - 1) \tag{25}$$

Furthermore, if we take T_0 as the reference temperature at which the resistance Ω is Ω_0 and the corresponding temperature coefficient of the resistance is β, the resistance Ω can be expressed as

$$\Omega = \Omega_0[1 + \beta(T_w - T_0)] \tag{26}$$

Now let

$$\lambda = \Omega/\Omega_0 \tag{27}$$

Then, from Eq. (26),

$$T_w/T_0 = [(\lambda - 1)/\beta T_0] + 1 \tag{28}$$

Now introduce ρ_0 as the reference density and i_0 as the reference heating current; then Eq. (24) can be written as

$$\left(1 + \frac{\lambda - 1}{\beta T_1}\right)^4 = \left[\frac{\alpha\rho_0(RT_0)^{3/2}}{\pi\sqrt{2}\epsilon\sigma T_0^4}\right]\left(\frac{\rho}{\rho_0}\right)\left(\frac{T}{T_0}\right)^{3/2}\left\{F_1\left(\frac{U}{c}\right)\left[\frac{U^2}{c^2} + \frac{1}{2}\frac{\gamma + 1}{\gamma - 1}\left(1 - \frac{1 + \frac{\lambda - 1}{\beta T_0}}{T/T_0}\right)\right] + F_2\left(\frac{U}{c}\right)\left[\frac{U^2}{c^2} + \frac{\gamma}{\gamma - 1}\left(1 - \frac{1 + \frac{\lambda - 1}{\beta T_0}}{T/T_0}\right)\right]\right\} + \left(\frac{i_0^2\Omega_0}{2\pi r\epsilon\sigma T_0^4}\right)\lambda\left(\frac{i}{i_0}\right)^2 \tag{29}$$

The particular values of the reference temperature T_0, the reference density ρ_0, and the reference current i_0 are not yet fixed. We fix these quantities now by requiring that

$$\beta T_0 = 1 \tag{30}$$

$$\alpha\rho_0(RT_0)^{3/2}/\pi\sqrt{2}\epsilon\sigma T_0^4 = 1 \tag{31}$$

$$i_0^2\Omega_0/2\pi r\epsilon\sigma T_0^4 = 1 \tag{32}$$

Then Eq. (29) simplifies into

$$\lambda^4 = \left(\frac{p}{p_0}\right)\left(\frac{T}{T_0}\right)^{1/2} \times \left\{F_1\left(\frac{U}{c}\right)\left[\left(\frac{U}{c}\right)^2 + \frac{1}{2}\frac{\gamma+1}{\gamma-1}\left(1 - \frac{\lambda}{T/T_0}\right)\right] + F_2\left(\frac{U}{c}\right)\left[\left(\frac{U}{c}\right)^2 + \frac{\gamma}{\gamma-1}\left(1 - \frac{\lambda}{T/T_0}\right)\right]\right\} + \lambda\left(\frac{i}{i_0}\right)^2 \tag{33}$$

This is then the performance equation of the hot wire in free molecular flow.

Now let us investigate in greater detail the case of a bright platinum wire. To satisfy Eq. (30), $T_0 = 492°\text{R}$. The value for ϵ and α can be taken to be 0.08 and 0.90, respectively. Then Eq. (31) gives the corresponding pressure p_0 for ρ_0 and T_0 as

$$p_0 = \pi\sqrt{2}^4\sigma T_0^4/\alpha\sqrt{RT_0} = 3.37 \text{ microns}$$

Let the radius r of the wire be 0.0001 in. Then Eq. (32) gives the reference heating current i_0 as

$$i_0 = \sqrt{2}\pi r\epsilon\sigma T_0^4/\Omega_0 = 0.274 \text{ milliamp.}$$

where the resistivity of the platinum is taken as 10.96×10^{-6} ohm-cm. Therefore the order of magnitude of the different quantities is entirely satisfactory.

If the wire is used with a constant heating current, then Eq. (33) can be used to calculate the relation between the resistance ratio λ and the velocity ratio (U/c) at constant air-stream density and temperature.* This is done for $p/p_0 = 1$, $T/T_0 = 1$, and $i/i_0 = 1$,* and the result is given in Fig. 6. It is seen that the sensitivity of the instrument is good. Of course, the behavior of the hot-wire anemometer will be actually determined by calibration for any experiment. Since the performance of the wire is strongly influenced by the accommodation coefficient α, as shown by Eq. (29), it will be necessary to find materials that can hold this coefficient constant for a considerable period of time so that no frequent calibration is required. However, the present analysis seems to indicate the feasibility of such an instrument for measurements in rarefied gases, and further research is definitely desirable.

* The author is indebted to L. Mack for the numerical computations.

(4) Parameters of Flow

The two parameters that are directly connected with the flow field are the Reynolds Number Re, defined as $Re = UL/\nu^\circ$ (where ν° is the kinematic viscosity, L is the typical linear dimension of the body), and the Mach Number M° of the free stream. This is true even for slip flows and free molecule flows because of the fact that the ratio of mean free path to the typical dimension can be also expressed in terms of the Reynolds Number and the Mach Number.

However, as the pressure or density is reduced, the solid boundary of the flow enters actively into the flow conditions by requiring not only that the microscopic stream velocity be tangential to the surface but that the interaction of the molecules and the wall be considered and that the radiation of energy to and from the wall be taken into account. The interaction of the molecules with the wall is so far expressed through the fraction s of molecules that are diffusely re-emitted from the wall and the accommodation coefficient α. It is known that both s and α are functions of the temperature of the wall, and there is reason to believe that they are also functions of the molecular velocity distribution. Therefore the interaction of the molecules with the wall is the same only if the wall temperature, the gas tem-

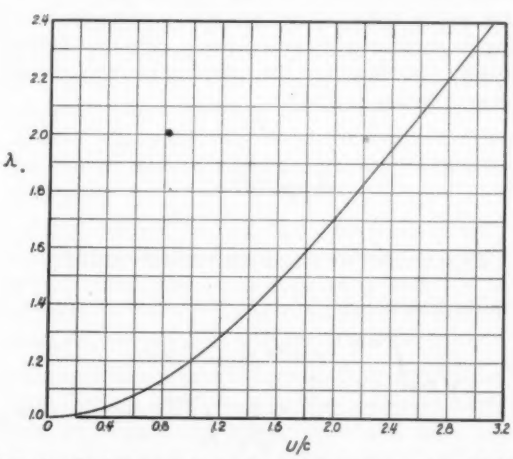

Fig. 6. Resistance ratio λ of a round platinum wire of 0.0002 in. diameter, heated by a constant current of 0.274 milliamp. in a wind stream of 3.37μ static pressure and 492°R. static temperature. $U/c = \sqrt{\gamma/2}\,M$; M = Mach Number of air stream.

perature, and the Mach Number of the gas above the wall are the same. These considerations seem to indicate then that for the model test to be similar to the prototype, the model must be made of same surface material as the prototype, the fluid must be the same, and, furthermore, the following parameters must be the same: (1) Reynolds Number, Re; (2) Mach Number, $M°$; and (3) free-stream temperature $T°$.

The radiation heat loss from the surface is equal to $\epsilon\sigma T_w^4$ per unit area. However, if the model is surrounded by the walls of the test chamber, there is also a heat input due to radiation from walls of the test section to the model. Let us call this quantity q_c. Then the net heat loss per unit area of the surface of the model is $\epsilon\sigma T_w^4 - q_c$. This quantity can be rendered nondimensional by dividing it by $\rho° U c_p T°$. Call this new parameter Λ_m; then

$$\Lambda_m = [(\epsilon\sigma T_w^4 - q_c)/\rho° U c_p T°]_m \tag{34}$$

For the prototype, the heat from the walls of the test chamber is absent, but there may be solar radiation and the radiation from the earth and surrounding atmosphere.[9] Denoting this amount by q, the parameter Λ for the prototype is then

$$\Lambda = (\epsilon\sigma T_w^4 - q)/\rho° U c_p T° \tag{35}$$

In order for the flow also to be same with respect to the radiation heat transfer,

$$\Lambda = \Lambda_m \tag{36}$$

Because of the previous conditions on the Reynolds Number and free-stream temperature, Eq. (36) is the same as

$$(\epsilon° T_w^4 - q)/(\epsilon° T_w^4 - q_c) = L_m/L \tag{37}$$

where L_m is the typical linear dimension of the model and L is the typical linear dimension of the prototype. This means that the wall temperature of the test chamber must be so controlled that q_c satisfies Eq. (37).

This set of rather strict similarity rules for model testing in superaerodynamic flows is certainly difficult to satisfy. In what way the rules can be relaxed is the problem of future research.

Appendix

Evaluation of the Functions F_1 and F_2

For the function F_1,

$$F_1(z) = \frac{1}{\sqrt{\pi}} \int_{-\pi/2}^{\pi/2} e^{-z^2 \sin^2\theta}\, d\theta = \frac{2}{\sqrt{\pi}} \int_0^{\pi/2} e^{-(z^2/2)(1-\cos 2\theta)}\, d\theta$$

$$= \frac{1}{\sqrt{\pi}} e^{-z^2/2} \int_0^{\pi} e^{(z^2/2)\cos\varphi} d\varphi = \sqrt{\pi}\, e^{-z^2/2} I_0\left(\frac{z^2}{2}\right)$$

where I_0 is the modified Bessel function of first kind and under zero. The last step is made possible by the substitution $2\theta = \varphi$.

For the function F_2,

$$F_2(z) = \int_{-\pi/2}^{\pi/2} (z \sin\theta)\,[1 + erf\,(z \sin\theta)]\, d\theta = \int_{-\pi/2}^{\pi/2} (z \sin\theta)\, erf\,(z \sin\theta)\, d\theta$$

By the definition of the error function, we have

$$F_2(z) = (z/\sqrt{\pi}) \int_{-\pi/2}^{\pi/2} 2 \sin\theta \left(\int_0^{z \sin\theta} e^{-s^2}\, ds\right) d\theta$$

This form can be simplified by partial integration. Thus

$$F_2(z) = (4/\sqrt{\pi})\, z^2 \int_0^{\pi/2} \cos^2\theta\, e^{-z^2 \sin^2\theta}\, d\theta$$

$$= (2/\sqrt{\pi})\, z^2 \int_0^{\pi/2} (1 + \cos 2\theta)\, e^{-z^2 \sin\theta}\, d\theta$$

$$= \sqrt{\pi}\, z^2\, e^{-z^2/2} \times \left[I_0\left(\frac{z^2}{2}\right) + \frac{1}{\pi} \int_0^{\pi} \cos\varphi\, e^{+z^2/2 \cos\varphi}\, d\varphi \right]$$

Therefore

$$F_2(z) = \sqrt{\pi}\, z^2 e^{-z^2/2} \left[I_0\left(\frac{z^2}{2}\right) + I_1\left(\frac{z^2}{2}\right) \right]$$

where I_1 is the modified Bessel function of first kind and order one.

References

[1] Puckett, A. E., *Supersonic Nozzle Design*, Journal of Applied Mechanics (A.S.M.E.), Vol. 13, p. A-265, 1946.

[2] Tsien, H.-S., *Superaerodynamics, Mechanics of Rarefied Gases*, Journal of the Aeronautical Sciences, Vol. 13, No. 12, p. 653, December, 1946.

[3] Schamberg, R., *The Fundamental Differential Equations and the Boundary Conditions for High Speed Slip-Flow, and their Application to Several Specific Problems*, Thesis, California Institute of Technology, 1947.

[4] Schaaf, S. A., *Viscosity Effects in Wind Tunnel No. 2*, University of California, Department of Engineering Report No. HE-150-16, 1947.

[5] Schaaf, S. A., *The Theory of Minimum Response Time for Vacuum Gages*, University of California, Department of Engineering Report No. HE-150-21, 1947.

[6] Evans, R. A., *Flow Visualization at Low Pressures*, University of California, Department of Engineering Report No. HE-150-21, 1947.

[7] Barker, M., *On the Use of Very Small Pitot-tubes for Measuring Wind Velocity*, Proc. Royal Society (A), Vol. 101, pp. 435-445, 1922.

[8] Homann, F., *Einfluss grosser Zahigkeit bei Stromung um Zylinder*, Forschung Ingews., Vol. 7, pp. 1–10, 1936.

[9] Johnson, H. A., and Possner, L., *A Design Manual for Determining the Thermal Characteristics of High Speed Aircraft*, Chapt. 4, A.A.F. Technical Report No. 5632, 1947.

Primary Instability of Open-Section Stringers Attached to Sheet

SAMUEL LEVY* AND WILHELMINA D. KROLL†
National Bureau of Standards

ABSTRACT

A method is presented for predicting the primary instability of open-section stringers attached to sheet. The method extends the torsion bending theory to take account of the stabilizing effect of the sheet to which the stringer is fastened. The effects of the sheet in restraining twisting and warping of the stringer, as well as in forcing the center of twist to lie in the plane of the sheet, are considered. The method is checked by comparing computed and observed values of maximum load for sheet-stringer panels reinforced by Z-section stringers. The load carried by the sheet in these panels was computed from a nomogram derived for a previous investigation. Experimental data from two groups of unpublished test results and from three other investigations are included in the comparison.

(1) INTRODUCTION

THE ANALYSIS DESCRIBED in this report was conducted for the Bureau of Aeronautics, Navy Department, to provide a convenient method for estimating the stabilizing effect of the sheet on the buckling load in compression of open-section stringers in sheet-stringer panels and to check this method against observed values of maximum load for such panels.

Open-section stringers in a sheet-stringer panel under uniform end compressive stress may fail as follows:

(1) Primary instability by twisting about an axis parallel to the centroidal axis of the stringer without cross-sectional distortion. (The type of failure goes from combined twisting and bending to pure bending as the axis of twist is moved from the neighborhood of the stringer to infinity.)

(2) Secondary instability by local buckling in which the cross section is distorted.

(3) Primary instability by a combination of twisting and cross-sectional distortion.

The mode of failure to be expected in any given case is that associated with the lowest computed critical stress. The analysis in this report is confined to relatively heavy cross sections of sufficient length to fail by primary instability as defined by (1). The possibility of modifying the analysis to take account of primary instability as defined by (3) is discussed.

The theory of primary instability of columns by bending (i.e., twisting about an axis far from the column) is based on the early work of Euler and is well understood. The theory of primary failure by twisting about an axis close to the centroid of the column has received thorough investigation in recent years.[1–6] In references 3 and 4, particular attention has been given to the effect of attached sheet on the location of the center of twist. Additional information on the effect of sheet on the location of the center of twist is given in reference 7 for the analogous problem of bending of sheet-stringer panels.

The effect of sheet on the load for primary failure of open-section stringers is discussed by Lundquist and Fligg[3] for the case of an I-section stringer. The results take account of the thickness of the sheet and are applicable to stringers of symmetrical cross section with center of twist either directly under the stringer or at infinity. Goodier[4] presents an analysis applicable to both symmetrical and unsymmetrical open-section stringers attached to sheet. His analysis takes into account the stiffness of the sheet in its own plane, which requires the center of twist to lie in the plane of the sheet. Weibel[7] considers in detail the restraint of stringers by the attached sheet in connection with the problem of bending of sheet-stringer panels.

References 3 and 7 neglect the effect of buckling of the sheet between stringers on the primary instability of the stringer. This omission is probably not a source of serious error for the following reasons. In the case of thin sheet, for which sheet buckling may occur early, the principal effect of the sheet is considered—namely, to force the center of twist into the plane of the sheet. The theory takes account of this effect. For thick sheet, for which sheet buckling may either not occur at all or be of negligible amplitude, the bending stiffness of the sheet is approximately taken into account by the theory.

In the present report, the theory of primary instability of open-section stringers of arbitrary cross section will be extended to take account of both the bending stiffness of the sheet and the axial restraint that the sheet provides against warping of the stringer.

The condition that the center of twist must lie in the sheet conveniently reduces the necessary number of stringer section constants from the nine used by Kappus[2] to six; at the same time, three new section constants must be added to take account of the sheet.

Received March 12, 1948.

* Physicist.

† Aeronautical Engineer.

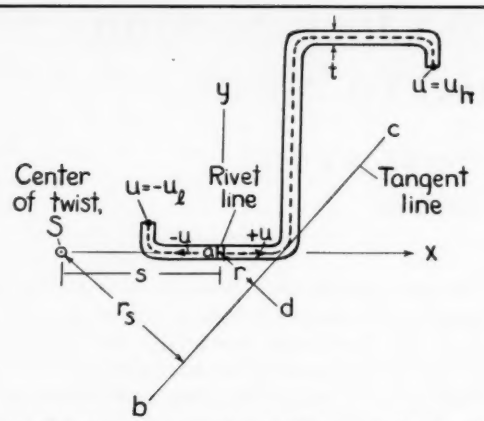

FIG. 1. Notation for computing section constants J_T, C_o, R, I, M_y.

(2) TORSIONAL INSTABILITY OF OPEN-SECTION STRINGER ATTACHED TO SHEET

The critical compressive stress for torsional instability of an open-section stringer attached to sheet will be computed from the equation[2]

$$\sigma_{cr} = [GJ_T + G(J_T)_{sh} + (C\pi^2E/L^2)]/J_p \qquad (1)$$

where

E = Young's modulus
G = shear modulus $= E/2(1+\nu)$
L = effective length of panel (one-half the actual length in the case of panels loaded between flat ends)
ν = Poisson's ratio, taken as 0.3 in this analysis

J_T, $(J_T)_{sh}$, C, J_p are section constants to be discussed.

(2.1) *Evaluation of J_T, $(J_T)_{sh}$*

The constants J_T and $(J_T)_{sh}$ in Eq. (1) take account of the stabilizing effect due to torsional rigidity of the stringer and the sheet, respectively. J_T can be calculated by the formula

$$J_T = (1/3) \int_{u=-u_l}^{u=u_h} t^3\, du \qquad (2)$$

where

u = coordinate along the mid-thickness of the cross section (shown dotted in Fig. 1); $u = -u_l$ at one end of the cross section, $u = u_h$ at other end of cross section, and $u = 0$ at rivet line
t = thickness of cross section

If a more exact value of J_T is desired, the value obtained above may be corrected as outlined in Eqs. (5a) to (5d) of reference 6. Formulas for J_T for Z-stringers, in terms of the dimensions, are given in Appendix E.

The constant $(J_T)_{sh}$ depends on the rotation of the stringers relative to the sheet. In Fig. 2a, all of the stringers rotate in the same sense about their centers of twist S, and in so doing cause the sheet to deflect laterally as shown by the dotted line. This type of deformation is characteristic of asymmetrical stringers. In the case of certain symmetrical stringers of short length, on the other hand, the stringers tend to alternate in their direction of rotation, as indicated in Fig. 2b. The lateral deflections, shown dotted in Fig. 2, vary as a sine wave along the length of the panel with nodal points at the ends of the effective panel length L.

The stiffness of the sheet in its own plane forces the center of twist, S, Fig. 2, to lie in the original plane of the sheet at a distance s to the left of the rivet line.

The number of stringers in the sheet-stringer panel is considered to be large enough so that the effect of edge conditions along the edges of the panel parallel to the load may be neglected.

The contribution of the sheet to the stiffness may be determined approximately by calculating the amount of energy stored in the sheet for a given twist θ_m at the mid-length of the stringer using an approximate expression for the sheet deflection. In the case of deflections of the types shown in Fig. 2, it is shown in Appendix A that the sheet contributes

$$(J_T)_{sh} = B_0 + B_s s^2 \qquad (3)$$

For deflections of the type shown in Fig. 2a,

$$\left.\begin{aligned} B_0 &= bh^3\,[0.0952 + 0.289\,(L/b)^2] \\ B_s &= 2.35\,(bh^3/L^2) \end{aligned}\right\} \qquad (3a)$$

and, for deflections of the type shown in Fig. 2b,

$$\left.\begin{aligned} B_0 &= bh^3\left[0.238 + 0.119\left(\frac{L}{b}\right)^2 + 0.119\left(\frac{b}{L}\right)^2\right] \\ B_s &= \frac{bh^3}{L^2}\left[1.175 + 2.35\left(\frac{L}{b}\right)^2 + 1.175\left(\frac{L}{b}\right)^4\right] \end{aligned}\right\} \qquad (3b)$$

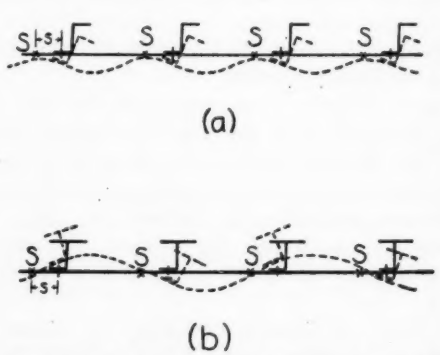

FIG. 2. Twisting of stringers and accompanying deformation of sheet. (a) Stringers all rotate in same direction, characteristic of asymmetrical stringers. (b) Stringers alternate in direction of rotation, characteristic of some nearly symmetrical stringers.

where

b = stringer spacing
h = sheet thickness
s = distance from center of twist S to rivet line of stringer (to be discussed below)
L = effective length of panel

Either Eqs. (3a) or (3b) are applicable, whichever leads to the lower critical stress according to Eq. (1). Eqs. (3a) give the lower critical stress for most asymmetrical (e.g., Z- and C-section) and for symmetrical stringers for which s and L are large compared to b (e.g., I- and U-sections). Eqs. (3b) give the lower critical stress for some nearly symmetrical stringers of short length.

(2.2) *Evaluation of C*

The term C in Eq. (1) is the "torsion-bending" constant. It corresponds to that part of the critical compressive stress caused by the resistance to nonuniform twist of portions of the stringer having bending stiffness. The value of C depends on the location of the center of twist of the stringer and upon the geometry of the stringer.

A convenient method of computing C for a given axis of twist is presented in references 2 and 6. The method is used in Appendix B, together with the assumption that the center of twist lies in the plane of the sheet. Appendix B leads to the following procedure for computing C:

(1) Draw a line along the mid-thickness of the stringer cross section (shown dotted in Fig. 1). Let u be the coordinate along this line. Let the value of u be zero at the rivet line and let u increase to the right as viewed at the rivet line.

(2) Determine, as a function of u, the distance r (Fig. 1) from the rivet line a to the tangent line bc. The direction of the tangent line is the same as the direction of u. The value of r is taken as positive when line ad must be rotated counterclockwise 90° to assume the direction of the tangent line bc; it is taken as negative when line ad must be rotated clockwise 90° to assume the direction of the tangent line. The value of r shown in Fig. 1 is positive.

(3) Compute the unit warping displacement w as a function of u from

$$w = \int_0^u r\,du \tag{4}$$

(4) Compute the torsion-bending constant C_0 for twisting about a, Fig. 1, from

$$C_0 = \int_{u=-u_l}^{u=u_h} w^2 t\,du - \frac{1}{A+a}\left(\int_{u=-u_l}^{u=u_h} wt\,du\right)^2 \tag{5}$$

where

$-u_l$ = lowest value of u
u_h = highest value of u
t = thickness of stringer
A = cross-sectional area of stringer
a = cross-sectional area of sheet per stringer (for unbuckled sheet in a wide panel, $a = bh$; for buckled sheet in a wide panel, $a = bh/2$. b = stringer spacing; h = sheet thickness).

(5) Compute the warping moment R from

$$R = \int_{u=-u_l}^{u=u_h} wyt\,du - \frac{1}{A+a}\left(\int_{u=-u_l}^{u=u_h} wt\,du\right)\times\left(\int_{u=-u_l}^{u=u_h} yt\,du\right) \tag{6}$$

where y = coordinate perpendicular to sheet at rivet line, Fig. 1.

(6) Compute the moment of inertia I from

$$I = \int_{u=-u_l}^{u=u_h} y^2 t\,du - \frac{1}{A+a}\left(\int_{u=-u_l}^{u=u_h} yt\,du\right)^2 \tag{7}$$

x = coordinate parallel to sheet at rivet line. The x-axis is tangent to the mid-thickness line at $u = 0$.

(7) The torsion-bending constant C required in Eq. (1) is given by the equation

$$C = C_0 + 2Rs + Is^2 \tag{8}$$

where s = the distance along the x-axis from the center of twist to the rivet line, Fig. 1. The value of s is positive if the center of twist is to the left of the rivet line as shown in Fig. 1. The determination of s will be discussed below.

Formulas for C_0, R, and I for Z-stringers are given, in terms of the dimensions, in Appendix E.

(2.3) *Evaluation of J_P*

The term J_p in Eq. (1) is the polar moment of inertia about the center of twist. It is shown in Appendix C that J_p may be computed from:

$$J_p = J_{p0} + 2M_y s + (A+a)s^2 \tag{9}$$

where

$M_y = \int_{u=-u_l}^{u=u_h} tx\,du$ (9a)

J_{p0} = polar moment of inertia of stringer cross section about rivet line
t, A, a defined in connection with Eq. (5)
s defined in connection with Eq. (8)

Appendix E gives formulas for M_y, J_{p0}, and A for Z-stringers in terms of the dimensions.

(2.4) *Evaluation of s and of σ_{cr}*

The critical compressive stress for a given location of the center of twist is given by Eq. (1). In that equation $(J_T)_{sh}$, C, and J_p are quadratic functions of s determined by Eqs. (3), (8), and (9), from the panel dimensions; L is the effective length of the panel; E is Young's modulus; and G is taken as $E/2.6$. After substituting for J_T, $(J_T)_{sh}$, C, J_p and factoring out E, it is found that Eq. (1) can be expressed as

$$\frac{\sigma_{cr}}{E} = \frac{\left(0.385J_T + 0.385B_0 + 9.87\frac{C_0}{L^2}\right) + \left(19.74\frac{R}{L^2}\right)s + \left(0.385B_s + 9.87\frac{I}{L^2}\right)s^2}{J_{p0} + 2M_y s + (A + a)s^2} \tag{10}$$

In Appendix D, it is shown that the buckling stress σ_{cr} will be a maximum or a minimum if the distance s to the center of twist is a root of the equation

$$\left(\frac{s}{L}\right)^2\left[9.87R\,(A + a) - M_y\,(0.385B_sL^2 + 9.87I)\right] + \left(\frac{s}{L}\right)\left[(A + a)\left(0.385\,J_TL + 0.385B_0L + 9.87\frac{C_0}{L}\right)\right.$$
$$\left. - J_{p0}\left(0.385B_sL + 9.87\frac{I}{L}\right)\right] + \left[M_y\left(0.385J_T + 0.385B_0 + 9.87\frac{C_0}{L^2}\right) - J_{p0}\left(9.87\frac{R}{L^2}\right)\right] = 0 \tag{11}$$

The roots s of Eq. (11) can be determined algebraically. Substitution of s into Eq. (10) gives σ_{cr}/E.

(2.5) *Plastic Buckling*

It has been shown by Shanley,[8] in the case of columns, that plasticity causes the effective modulus to drop to a value between the tangent modulus and von Kármán's reduced modulus. Stowell[9] shows how the effective modulus in the case of plates depends on the stress-strain curve of the material and the geometry of the structure. The difficulty of extending these theories to take account of instability of the type considered here made it necessary to choose the effective modulus in the plastic range on some other basis. It is shown in Fig. 10, reference 6, that, for 125 unsupported open-section columns that failed by torsional instability, buckling stresses computed with the reduced modulus agreed, within the experimental scatter, with the measured buckling stresses. On the assumption that stringers attached to sheet have a similar behavior, the buckling stress σ_{cr} in the plastic range may be estimated from that in the elastic range $(\sigma_{cr})_{\text{elastic}}$, given by Eq. (1), by solving

$$\sigma_{cr} = (\sigma_{cr})_{\text{elastic}}(E_r/E) \tag{12}$$

where E_r = reduced modulus corresponding to stress σ_{cr} and E = Young's modulus. An approximate value of E_r/E can be computed knowing Young's modulus and two secant yield strengths σ_1, σ_2. These two yield strengths are defined as the stresses at the intersections of the stress-strain curve and lines through the origin with slopes of $0.7E$ and $0.85E$, respectively.

The computation is made with the help of the nomogram taken from reference 6 and shown in Fig. 3a or 3b, proceeding as follows:

Draw a line from $(\sigma_{cr})_{\text{elastic}}/\sigma_1$ on scale 1 through the value σ_1/σ_2 on scale 2. From the intersection of this line with scale 3, draw a line through the value σ_1/σ_2 on scale 5. The intersection of the last line with scale 4 is the desired value of E_r/E.

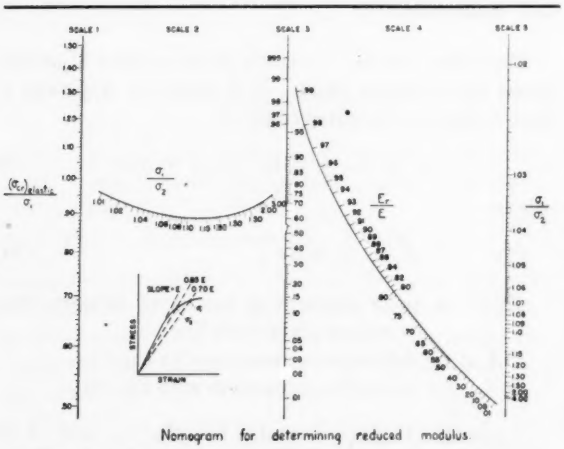

FIG. 3a. Nomogram for determining reduced modulus.

(3) COMPARISON OF COMPUTED WITH EXPERIMENTAL RESULTS

A comparison of computed critical stresses with experimental values was made in view of the simplifying assumptions made in the preceding analysis. Foremost among these assumptions are: (1) that the stringer is sturdy so that failure is by primary twisting instability with little or no cross-sectional distortion, and (2) that the effect of the bending stiffness of the sheet in torsionally restraining the stringer is adequately accounted for by the simplified analysis in Appendix A.

An additional assumption, frequently made in using analyses of the type presented here, is (3) that the critical stress for primary instability and the failing stress are the same. This assumption will be essentially correct for Z-section stringers but may give a conserva-

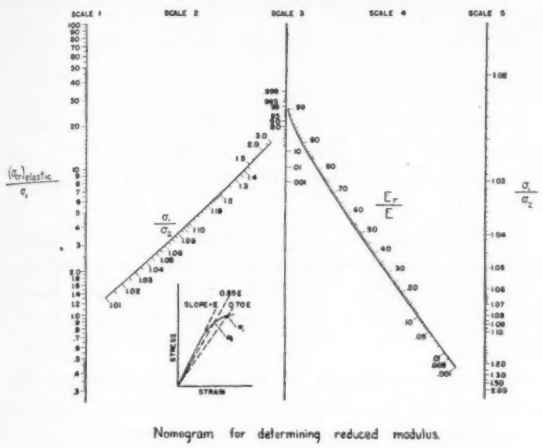

FIG. 3b. Nomogram for determining reduced modulus.

tive value for other types of stringers, such as thin-walled angles, for which the critical stress can be considerably less than the maximum stress (reference 6, Figs. 11 and 12).

Values of critical stress were computed for the comparison not only as outlined above but also taking $(J_T)_{sh} = 0$. This was done for panels with relatively stiff sheet to approximate the effect of a type of cross-sectional distortion localized in the web of the stringer in which the free flange of the stringer rotates relative to the flange attached to the sheet. For panels with sheet that is not so stiff, the effect of $(J_T)_{sh}$ should be small, and the calculations were intended to show whether the error due to neglecting $(J_T)_{sh}$ for such panels was negligible.

The comparison was extended over a sufficient number of references among the many available in the literature to cover the range of panel dimensions and stringer shapes most commonly used. The results of the comparison are given below for each reference in turn.

(3.1) *Unpublished Test Results—Group A*

Tests were made of 18 24S-T aluminum-alloy panels with Z-section stringers. The panels covered a range of lengths from 8 to 24 in.; stringer spacings of 2, 4, and 8 in.; and sheet thicknesses of 0.025-, 0.051-, and 0.081-in. The stringer cross section is shown in Fig. 4a. The panel dimensions are given in Table 1. The panel constants, computed as outlined in this paper, are listed in Table 2. The area of sheet acting with each stringer, when the sheet was unbuckled, was taken as the total sheet area divided by the number of stringers and, when the sheet was buckled, as one-half this area. The load carried by the stringers, computed by considering σ_{cr} to be the maximum stress of the stringers, was calculated from the panel constants and Eqs. (11), (10), and (12). Sheet loads were obtained by use of the nomogram of reference 10.

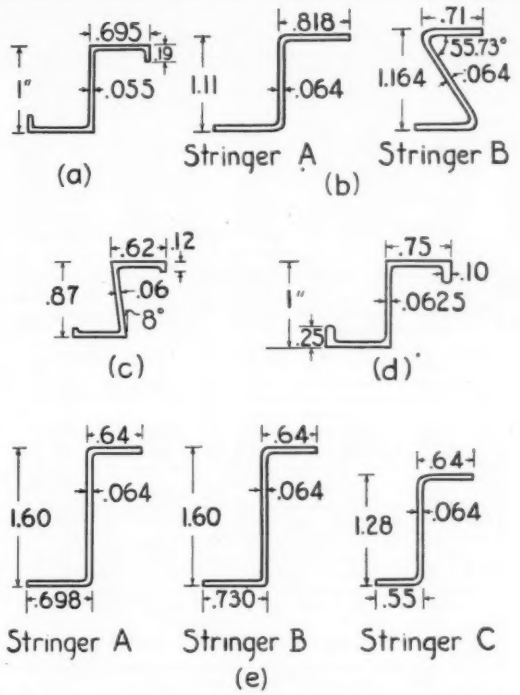

FIG. 4. Cross sections of stringers used in panels for which maximum loads or stresses were computed. All dimensions in inches. (a) unpublished tests, Group A; (b) reference 11; (c) reference 12; (d) unpublished tests, Group B; (e) reference 13.

Table 1 – Dimensions of panels

Unpublished test results – Group A

Panel	Length (in.)	Width (in.)	Thickness (in.)	No. of stringers	Stringer spacing (in.)	Rivet spacing (in.)	Area of sheet (in²)	Area of each stringer (in²)	Area of panel (in²)
1	8.02	16.82	0.0253	5	4	0.5	0.426	0.196	1.108
2	11.96	17.04	.0246	5	4	.5	.419	.137	1.102
3	16.05	16.83	.0266	5	4	.5	.448	.135	1.122
4	20.00	16.89	.0249	5	4	.5	.421	.139	1.114
5	24.05	16.84	.0250	5	4	.5	.421	.136	1.099
6	12.06	16.90	.0249	3	8	.5	.421	.133	.819
7	24.05	16.91	.0264	3	8	.5	.446	.136	.853
8	12.07	16.92	.0250	2	2	.5	.423	.138	1.664
9	24.05	16.87	.0250	9	2	.5	.422	.138	1.667
10	24.04	16.90	.0518	9	2	1.0	.875	.137	2.105
11	24.04	16.81	.0512	5	4	1.0	.860	.141	1.567
12	24.05	16.80	.0510	3	8	1.0	.857	.135	1.261
13	23.93	16.87	.0813	9	2	1.0	1.372	.136	2.593
14	24.05	16.87	.0810	5	4	1.0	1.366	.137	2.050
15	24.01	16.87	.0814	3	8	1.0	1.373	.131	1.767
16	24.03	12.91	.0253	4	4	.5	.327	.139	.862
17	24.03	8.74	.0248	3	4	.5	.217	.135	.623
18	24.02	4.86	.0250	2	4	.5	.121	.136	.394
Reference 11									
Stringer A, Figure 4(b)									
PB-1	16	8.8	.025	3	4	.75	.234	.152	.589
PB-14	24	16 8	.025	3	8	.75	.429	.152	.585
PB-15	24	20.8	.025	3	10	.75	.535	.153	.995
Stringer B, Figure 4(b)									
PC-1	16	8.7	.025	3	4	.75	.220	.159	.698
PC-12	24	12.7	.025	3	6	.75	.321	.156	.792
Reference 12									
1	19	16	.070	3	4	.875	1.12	.13	1.51
6	19	16	.025	3	4	.875	.80	.13	.79

Unpublished test results – Group B

Panel	Length (in.)	Width (in.)	Sheet Thickness (in.)	No of stringers	Stringer spacing (in.)	Rivet spacing (in.)	Area of sheet (in²)	Area of each stringer (in²)	Area of panel (in²)
3	15.97	16.04	0.7617	3	4.00	1.00	0.829	0.192	1.404
4	19.97	16.04	.0618	3	4.00	1.00	.821	.193	1.410
5	23.92	16.01	.0506	3	4.00	1.00	.810	.196	1.395
Reference 13									
Stringer A, Figure 4(c)									
1	23.24	26.10	0.1016	6	5.08	1.25	2.652	.180	3.73
2	41.52	26.10	.1016	6	5.08	1.25	2.652	.180	3.73
3	58.24	26.10	.1016	6	5.08	1.25	2.652	.180	3.73
4	80.56	26.10	.1016	6	5.08	1.25	2.652	.180	3.72
Stringer B, Figure 4(c)									
5	17.66	32.10	.1256	6	6.278	1.25	4.029	.182	5.12
6	31.60	32.10	.1258	6	6.278	1.25	4.029	.182	5.12
7	44.92	32.10	.1255	6	6.278	1.25	4.029	.182	5.12
8	58.16	32.10	.1256	6	6.278	1.25	4.029	.182	5.12
Stringer C, Figure 4(c)									
9	35.20	11.75	.064	6	2.24	0.75	.752	.150	1.65
10	70.64	11.78	.064	6	2.24	.75	.752	.150	1.68

Table 2 - Values of constants for panels
Unpublished test results - Group A

Panel	Sheet constants B_0	Sheet constants B_s	Combined constants C_0	Combined constants B	Combined constants I	Stiffener constants J_T	Stiffener constants b_y	Stiffener constants J_{ro}
1	0.0050747	0.00009316	0.004010	0.000124	0.02892	0.0001425	0.04623	0.08587
2	.0000841	.00000932	.004010	.000331	.02903	.0001425	.04623	.08587
3	.0000946	.00000276	.004011	.000342	.02922	.0001425	.04623	.08587
4	.0001176	.00000145	.004011	.000349	.02934	.0001425	.04623	.08587
5	.0001692	.00000102	.004010	.000326	.02892	.0001425	.04623	.08587
6	.0000320	.00000800	.004006	.000507	.03202	.0001425	.04623	.08587
7	.0001101	.00000239	.004023	.000553	.03279	.0001425	.04623	.08587
8	.0000852	.00000202	.004001	.000176	.02639	.0001426	.04623	.08587
9	.0003794	.00000951	.004001	.000178	.02643	.0001425	.04623	.08587
10	.002928	.00000452	.004015	.000385	.02995	.0001425	.04623	.08587
11	.001852	.00000873	.004029	.000648	.03451	.0001425	.04623	.08587
12	.0007938	.00001724	.004041	.000857	.03795	.0001425	.04623	.08587
13	.01122	.00001765	.004043	.000892	.03854	.0001426	.04623	.08587
14	.005795	.00003465	.004040	.000843	.03771	.0001425	.04623	.08587
15	.0032159	.00002756	.004054	.001075	.04164	.0001425	.04623	.08587
16	.0001751	.00000106	.004010	.000340	.02919	.0001425	.04623	.08587
17	..0001549	.00000099	.004006	.000270	.02800	.0001425	.04623	.08587
18	..0001688	.00000102	.004004	.000229	.02730	.0001425	.04623	.08587
Reference 11								
Stringer A, Figure 4(b)								
PB-1	.0000782	.00000310	.004613	.000242	.03919	.0002288	.06585	.12606
PB-14	.0000932	.00000204	.004767	.004200	.04610	.0002288	.06585	.12606
PB-15	.0000719	.00000255	.005821	.004278	.04779	.0002288	.06585	.12606
Stringer B, Figure 4(b)								
PC-1	.0000782	.00000329	.004673	.001983	.08122	.0002146	-.00616	.09851
PC-12	.0001171	.00000153	.004760	.004499	.09430	.0002146	-.00616	.09851

Reference 12

Panel	Sheet constants B_0	Sheet constants B_s	Combined constants C_0	Combined constants B	Combined constants I	Stiffener constants J_T	Stiffener constants b_y	Stiffener constants J_{ro}
1	0.002367	0.00003873	0.001731	0.001266	0.02960	0.0001319	0.03835	0.08017
6	.0001078	.00000163	.001869	.000317	.01800	.0001519	.03835	.08017
Unpublished test results - Group B								
3	.0006892	.00002037	.007330	-.001728	.04641	.0003309	.06217	.1222
4	.001084	.00001311	.007330	-.001728	.04641	.0003309	.06217	.1222
5	.001288	.00000801	.007330	-.01728	.04641	.0003309	.06217	.1222
Reference 13								
Stringer A, Figure 4(c)								
1	.008564	.00003293	.009821	.03008	.12733	.0002455	.05750	.1386
2[1]	.03629	.00002908	.009821	.03008	.12733	.0002455	.05750	.1386
3[1]	.08112	.00001476	.009821	.02108	.12733	.0002455	.05750	.1386
4	.02731	.00000772	.01242	.02715	.14282	.0002455	.05750	.1386
Stringer B, Figure 4(c)								
8	.008282	.0003737	.01098	.03436	.13733	.0003483	.05969	.2007
9[2]	.02391	.0001108	.01098	.03436	.13733	.0003483	.05969	.2007
10[2]	.0671	.0000879	.01098	.03436	.13733	.0003483	.05969	.2007
8	.1081	.0000281	.01158	.02709	.15034	.0003483	.05969	.2007

[1] Combined constants same as for panel 4 when $(J_T)_{sh} = 0$ as sheet fully effective
[2] Combined constants same as for panel 8 when $(J_T)_{sh} = 0$ as sheet fully effective

Reference 13 (continued)
Stringer C, Figure 4(c)

Panel	Sheet constants B_0	Sheet constants B_s	Combined constants C_0	Combined constants B	Combined constants I	Stiffener constants J_T	Stiffener constants b_y	Stiffener constants J_{ro}
9[3]	0.01053	0.0000045	0.004001	0.003016	0.06582	0.0003046	0.04206	0.1154
10	.04229	.0000011	.004114	.004074	.06820	.0003046	.04206	.1154

[3] Combined constants same as for panel 10 when $(J_T)_{sh} = 0$ as sheet fully effective

Comparison between the calculated and experimental maximum loads (Table 3) shows that the calculated total loads were from 5 per cent too low to 17 per cent too high. For those panels where the sheet thickness is considerably less than the stringer thickness, 0.025-in. sheet, 0.055-in. stringer, however, calculated and experimental loads differed by 8 per cent or less, with the exception of the shortest panel (8 in.) in which the correction for reduced modulus is relatively large, leading to a relative large effect of errors in reduced modulus.

For those panels for which the sheet thickness was approximately equal to, or greater than, the stringer thickness, the calculated loads were from 10 to 17 per cent higher than the experimental loads. These panels, after failure, showed that appreciable cross-sectional distortion accompanied primary failure. This distortion probably accounts for the lower experimentally observed stress at failure.

The total maximum loads were also computed with the assumption $(J_T)_{sh} = 0$. The resulting values are also given in Table 3. Comparison of these values with those obtained when $(J_T)_{sh}$ was determined by Eq. (3) shows that the neglect of $(J_T)_{sh}$ changed the computed load less than 8 per cent for the twelve panels using 0.025-in. sheet. For the remaining six panels with 0.051- and 0.081-in. sheet, the neglect of $(J_T)_{sh}$ leads to much better agreement between calculated and experimental loads. For these six panels, appreciable cross-sectional distortion of the stringer accompanied failure. The distortion was of such a nature that the lower edge of the web acted like a hinge. Apparently, the neglect of $(J_T)_{sh}$ can approximately account for this type of distortion.

(3.2) *Reference 11*

In reference 11, results are presented for aluminum-alloy panels with 24S-T aluminum-alloy sheet and Z-, S-, C-, and U-section stringers of 24S-RT aluminum alloy.

Calculated results were obtained for several panels with Z- and S-section stringers for comparison with experimental results. The dimensions of these panels are given in Table 1; the stringer sections are shown in Fig. 4b.

The panel constants for the Z- and S-stringers were computed by the simplified formulas in Appendix E, considering a to be one-half the sheet area per stringer. Values are given in Table 2. The computed total maximum loads, using the nomogram of reference 10 to get the sheet loads, are given in Table 3. Reference 11 does not contain compressive stress-strain curves for the 24S-RT stringer material which might be used for determining the reduced modulus. Compressive stress-strain curves for typical 24S-RT material could not be used, since the tensile properties of the stringer material were considerably lower than those for typical 24S-RT material. The tensile properties approximated those for 24S-T material. Hence, it was decided to determine the reduced modulus from compressive stress-strain curves of 24S-T material with the same tensile yield strength as the stringer material.

Comparison of the computed and experimental maximum loads for these panels shows that for panel PB-15, which was experimentally observed to fail by torsional instability, the computed load was 7 per cent too high; for panels PB-14 and PB-12, which were observed to fail by a combination of torsional and local instability, the computed loads were 3 per cent high and 6 per cent low, respectively; while, for panels PB-1 and PC-1, which were observed to fail by local instability, the computed loads were 10 and 2 per cent high, respectively. Thus it is seen that the computed loads for the three panels that failed entirely or partially by torsional instability agree with the experimental loads within 7 per cent. For the two panels that failed by local instability, the computed loads for torsional instability in one case, panel PB-1, is definitely higher than the observed load and, in the other case, panel PC-1, agrees within the possible errors. The results for these two panels are in agreement with the condition that the computed load for torsional instability should exceed the observed load when the failure is due to another type of instability.

When $(J_T)_{sh}$ was neglected, the computed loads for these five panels were from 10 per cent higher to 9 per cent lower than the experimental values. The neglect of $(J_T)_{sh}$ had only a minor effect on the computed loads.

Table 3 – Comparison of Computed and Experimental Results for Panels
Unpublished test results – Group A

Panel	Experimental maximum loads: Sheet, lb	Stringer, lb	Total, lb	Calculated loads, $(J_T)_{sh}$ considered: Sheet, lb	Stringer, lb	Total, lb	Difference in total load, %[1]	Calculated loads, $(J_T)_{sh} = 0$: Sheet, lb	Stringer, lb	Total, lb	Difference in total load, %[1]
1	6,100	29,200	35,300	5,600	33,200	38,800	9.9	5,600	33,100	38,700	9.6
2	6,200	28,000	34,200	5,300	29,900	35,200	2.9	5,300	30,000	35,300	3.2
3	7,700	23,700	31,400	6,000	25,600	31,600	.6	6,000	25,800	31,800	1.3
4	6,800	23,200	30,000	5,500	24,000	29,500	- .2	5,500	23,500	29,000	- 3.3
5	5,600	22,900	28,500	5,500	22,100	27,600	- 3.2	5,500	20,900	26,400	- 7.4
6	3,500	15,600	19,100	3,500[2]	16,700	20,200	5.8	3,500[2]	16,600	20,100	5.2
7	3,000	14,000	17,000	3,000[2]	13,100	16,100	- 5.1	3,000[2]	12,600	15,600	- 8.2
8	8,700	51,400	60,100	8,400	51,700	60,100	0.0	8,400	51,800	60,200	.2
9	9,200	40,300	49,500	8,400	42,500	50,900	2.8	8,400	38,400	46,800	- 5.5
10	24,800	39,700	64,500	26,700	47,200	73,900	14.6	26,700	37,900	64,600	.2
11	17,500	21,200	38,700	17,200	27,100	44,300	14.5	17,200	22,200	39,400	1.8
12	10,100	12,600	22,700	10,100[2]	15,200	25,300	11.5	10,100[2]	13,200	23,300	2.6
13	49,300	42,200	91,500	49,400	51,400	100,800	10.2	49,400	40,300	89,700	- 2.0
14	33,100	23,400	56,500	36,700[2]	29,300	66,000	16.8	36,700[2]	22,300	59,100	4.6
15	21,100	11,400	32,500	21,100[2]	15,200	36,300	11.7	21,100[2]	12,900	34,000	4.6
16	4,600	17,900	22,500	4,300	18,300	22,600	.4	4,300	17,200	21,500	- 4.4
17	2,700	14,000	16,700	2,800	13,800	16,600	- .6	2,800	13,100	15,900	- 4.8
18	2,000	8,540	10,540	2,000[2]	9,400	11,400	8.2	2,000[2]	8,800	10,800	2.5
Reference 11, Stringer A, Figure 4(b)											
PB-1	---	---	19,000	2,600	18,400	21,000	10.5	2,600	18,400	21,000	10.5
PB-14	---	---	17,740	2,600	15,600	18,200	2.6	2,600	15,600	18,200	2.6
PB-15	---	---	17,300	2,500	16,100	18,600	7.5	2,500	15,800	18,300	5.8
Stringer B, Figure 4(b)											
PC-1	---	---	21,700	2,500	19,700	22,200	2.3	2,500	19,400	21,900	0.9
PC-12	---	---	20,450	2,600	16,700	19,300	- 5.6	2,600	16,000	18,600	- 9.0
Reference 12											
1	22,400	14,100	36,500	22,400[3]	15,300	37,700	3.3	22,400[3]	13,200	35,600	- 2.5
6	4,300	14,100	18,400	4,300	13,400	17,700	- 3.8	4,300	12,900	17,200	- 6.5
Unpublished test results – Group B											
3	14,700	21,200	35,900	14,700[3]	23,300	38,000	5.8	14,700[3]	22,100	36,800	2.5
4	13,300	20,700	34,000	13,300[3]	22,200	35,500	4.4	13,300[3]	20,600	33,900	.3
5	13,300	19,300	32,600	13,300[3]	21,400	34,700	6.4	13,300[3]	19,000	32,300	- .9

1 $\frac{(\text{Total load})_{calc.} - (\text{Total load})_{exp.}}{(\text{Total load})_{exp.}} \times 100$

2 Experimental value used since panels had only 1 or 2 sheet bays which was considered too few for the nomogram of reference 10

3 Experimental value.

Reference 13

Panel	Experimental maximum stress: Sheet	Stringer	Average, psi	Calculated stress, $(J_T)_{sh}$ considered: Sheet, psi	Stringer, psi	Average psi	Diff. in average stress, %[1]	Calculated stress, $(J_T)_{sh} = 0$: Sheet psi	Stringer psi	Average psi	Diff. in average stress, %[1]
Stringer A, Figure 4(e)											
1	---	---	28,000	27,500	48,400	32,900	17.5	24,500	29,800	25,900	-- 7.6
2	---	---	25,000	27,500	40,400	30,800	23.2	13,100	13,100	13,100	-47.6
3	---	---	20,400	26,000	31,800	27,500	34.8	9,100	9,100	9,100	-55.4
4	---	---	13,500	13,300	13,300	13,300	- 1.5	7,100	7,100	7,100	-47.4
Stringer B, Figure 4(e)											
5	---	---	25,900	28,000	48,500	31,800	22.8	28,000	36,300	29,600	14.3
6	---	---	24,000	28,000	43,700	30,900	28.7	22,500	25,800	23,100	- 3.8
7	---	---	22,200	28,000	36,100	29,500	32.9	11,000	11,000	11,000	-50.4
8	---	---	13,600	14,100	14,100	14,100	3.7	7,200	7,200	7,200	-47.1
Stringer C, Figure 4(e)											
9	---	---	34,100	35,000	42,000	38,500	12.9	19,100	19,100	19,100	-44.0
10	---	---	17,200	18,700	18,700	18,700	8.7	10,200	10,200	10,200	-40.7

1 $\frac{(\text{Total load})_{calc.} - (\text{Total load})_{exp.}}{(\text{Total load})_{exp.}} \times 100$

2 Experimental value used since panels had only 1 or 2 sheet bays which was considered too few for the nomogram of reference 10.

3 Experimental value.

(3.3) *Reference 12*

Two of the 24S-T aluminum alloy panels reported in reference 12 were analyzed by the method presented in this report. The stringer section for these panels is shown in Fig. 4c, the dimensions are given in Table 1, and the panel constants are given in Table 2. The experimentally determined sheet load was used in computing the total load for panel 1, which had Alclad 24S-T aluminum-alloy sheet; the nomogram[10] was used in obtaining the sheet load for panel 6, which was fabricated with 24S-T sheet. The experimental and computed values are given in Table 3. They agreed within 4 per cent. With $(J_T)_{sh} = 0$, the calculated loads were 3 and 6 per cent too low for panels 1 and 6, respectively.

(3.4) *Unpublished Test Results—Group B*

Five Alclad 24S-T aluminum-alloy panels were tested to study the effect of length on the ultimate load of the panels. The comparison of computed and experimental loads was carried out for the three longest ones, panels

3, 4, and 5. The dimensions of these panels are given in Table 1.

The stringer section for these panels is shown in Fig. 4d and the panel constants are given in Table 2. The computed maximum total loads, Table 3, were from 4 to 6 per cent higher than the observed loads. When $(J_T)_{sh}$ was neglected, the computed total loads differed from the observed loads by -1 to 3 per cent.

(3.5) *Reference 13*

In reference 13, test results are reported for 576 24S-T aluminum-alloy panels with formed Z-stringers. The panels cover a wide range of lengths, stiffener spacings, and ratios of sheet thickness to stiffener thickness. Of these, ten panels were selected, representing three types of stringers (see Fig. 4e). The dimensions, computed from the nondimensional form of reference 13, are given in Table 1. The thickness of the sheet used in these panels was equal to, or greater than, the stiffener thickness. The stiffeners were formed from sheet and had no bulb, lip, or other stiffening element at the end of the flange. In addition, the outstanding flange was narrow.

The maximum stringer and sheet stresses were computed from the preceding theory and the nomogram of reference 10. The panel constants are given in Table 2. The median stress-strain curve for the stiffeners was used to correct for the reduced modulus. The stresses are listed in Table 3. The computed average stresses for the panels were 13 to 35 per cent greater than the measured stresses, except for the longest panels for which they were from 2 per cent too low to 9 per cent too high. The discrepancy may have been due to local instability of the stringers or to cross-sectional distortion accompanying primary failure, particularly for stringers A and B, which were attached to heavy sheet.

With $(J_T)_{sh} = 0$, the computed stresses were from 55 per cent less to 14 per cent greater than the observed values. The lack of agreement in this case would indicate that cross-sectional distortion localized in the web of the stringer was not predominant in these stringers with their narrow outstanding flanges.

(4) Conclusions

A comparison of computed and observed maximum loads for panels reinforced by Z-stringers of several designs leads to the following tentative conclusions:

(1) For panels reinforced by Z-stringers having a stringer thickness of two or more times the sheet thickness, the proposed method of computing stringer loads can be expected to give total loads accurate to within about 8 per cent. The computed total loads were lowered less than 8 per cent with the simplifying assumption $(J_T)_{sh} = 0$.

(2) For panels reinforced by Z-stringers having a bulb or lip at the end of the outstanding flange and having a stringer thickness equal to, or less than, the sheet thickness, the proposed method of computing stringer loads may give total loads up to 17 per cent too large; however, if used with $(J_T)_{sh} = 0$, it can be expected to be accurate to within about 8 per cent in many cases but cannot be relied on in all cases.

(3) For panels reinforced by Z-stringers having narrow outstanding flanges without a bulb or lip and having a stringer thickness equal to, or less than, the sheet thickness, the proposed method of computing stringer loads may give total loads up to 35 per cent too large. With $(J_T)_{sh} = 0$, the computed loads may be as much as 55 per cent low and as much as 14 per cent high.

Appendix A—Evaluation of $(J_T)_{sh}$

In order to evaluate $(J_T)_{sh}$ for the case where all the stringers rotate in the same direction, Fig. 2a, determine the energy stored in the sheet when the stringers have rotated through an angle θ about a center of twist S, Fig. 2a, where S is a distance s to the left of the rivet line. The following notation is used:

G = shear modulus $= E/2.6$
D = flexural rigidity of sheet $= Eh^3/10.92$
z = axial coordinate along stringer
x = transverse coordinate in sheet, with origin at rivet line
w = lateral deflection of sheet
b = stringer spacing
h = sheet thickness
L = effective panel length
θ_m = maximum twist of stringer relative to ends of panel of length L

Approximate the lateral deflection of the sheet by

$$w = \theta_m\left(s + x - \frac{3x^2}{b} + \frac{2x^3}{b^2}\right)\sin\frac{\pi z}{L}, \quad 0 \le x \le \frac{b}{2}$$

$$w = \theta_m\left(s + x + \frac{3x^2}{b} + \frac{2x^3}{b^2}\right)\sin\frac{\pi z}{L}, \quad -\frac{b}{2} \le x \le 0 \tag{1A}$$

From page 307 of reference 14, the energy stored in the sheet is

$$V = \frac{D}{2}\int_{z=0}^{L}\int_{x=-b/2}^{b/2}\left\{\left(\frac{\partial^2 w}{\partial x^2} + \frac{\partial^2 w}{\partial z^2}\right)^2 - 2(1-\nu)\left[\frac{\partial^2 w}{\partial x^2}\frac{\partial^2 w}{\partial z^2}\right] - \left(\frac{\partial^2 w}{\partial x \partial z}\right)^2\right\} dx dz \tag{2A}$$

Substituting Eq. (1A) into Eq. (2A) and performing the integration gives

$$V = \theta_m^2 D\frac{L}{b}\left(3 + 0.987\frac{b^2}{L^2} + 0.116\frac{b^4}{L^4} + 24.4\frac{b^2 s^2}{L^4}\right) \tag{3A}$$

The energy stored in a rod of torsion constant $(J_T)_{sh}$ and length L twisted through angles

$$\theta = \theta_m \sin (\pi z/L) \tag{4A}$$

is

$$V' = (\pi^2/4L)G(J_T)_{sh}\,\theta_m{}^2 \tag{5A}$$

Equating V and V', Eqs. (3A) and (5A) and solving for $(J_T)_{sh}$ gives

$$(J_T)_{sh} = bh^3\left[0.0952 + 0.289\left(\frac{L}{b}\right)^2 + 2.35\left(\frac{s}{L}\right)^2 + 0.0112\left(\frac{b}{L}\right)^2\right] \tag{6A}$$

Since b will ordinarily be less than L, the last term in Eq. (6A) can be neglected and Eq. (6A) rewritten

$$(J_T)_{sh} = B_0 + B_s s^2$$

where

$$\left.\begin{aligned} B_0 &= bh^3[0.0952 + 0.289(L/b)^2] \\ B_s &= 2.35bh^3/L^2 \end{aligned}\right\} \tag{7A}$$

In the case shown in Fig. 2b where the direction of stringer rotation alternates from stringer to stringer, determine the energy stored in the sheet when the lateral deflection is approximated by

$$w = \theta_m\sqrt{s^2 + \left(\frac{b}{\pi}\right)^2}\,\sin\frac{\pi z}{L}\left(\sin\frac{\pi x}{b} + \varphi\right) \tag{8A}$$

where $\varphi = \tan^{-1}(s\pi/b)$.

Substituting Eq. (8A) into Eq. (2A) and performing the integration gives

$$V = \theta_m{}^2\,D\,\frac{\pi^2 bL}{8}\,(s^2\pi^2 + b^2)\left(\frac{1}{L^4} + \frac{2}{L^2b^2} + \frac{1}{b^4}\right) \tag{9A}$$

Equating V, Eq. (9A), to V', Eq. (5A), and solving for $(J_T)_{sh}$ gives

$$(J_T)_{sh} = bh^3\left\{0.238 + 0.119\left(\frac{L}{b}\right)^2 + 0.119\left(\frac{b}{L}\right)^2 + \left(\frac{s}{L}\right)^2\left[1.175 + 2.35\left(\frac{L}{b}\right)^2 + 1.175\left(\frac{L}{b}\right)^4\right]\right\} \tag{10A}$$

Eq. (10A) can be rewritten

$$(J_T)_{sh} = B_0 + B_s s^2 \tag{11A}$$

where

$$B_0 = bh^3\left[0.238 + 0.119\left(\frac{L}{b}\right)^2 + 0.119\left(\frac{b}{L}\right)^2\right]$$

$$B_s = \frac{bh^3}{L^2}\left[1.175 + 2.35\left(\frac{L}{b}\right)^2 + 1.175\left(\frac{L}{b}\right)^4\right]$$

Appendix B—Evaluation of C

The torsion-bending constant C will be evaluated using the notation of Section (2.2) and Fig. 1. The following assumptions are made regarding the effect of the sheet on the constant C:

(1) The sheet has sufficient shear stiffness in its plane to force the center of twist to lie in the plane of the sheet.

(2) The axial rigidity of the sheet restrains warping of the stringer as though an additional area a were added to the stringer at the rivet line. This area a would equal the sheet area per stringer, bh, in the case of unbuckled sheet, and it would equal the effective incremental sheet area per stringer, $bh/2$, (corresponding to a small change in load) in the case of buckled sheet. (Fig. 6 of reference 15 gives about $0.4bh$ for simply-supported sheet, while Fig. 4 of reference 16 gives about $0.5bh$ for clamped sheet. A value of $0.5bh$ was used in all cases, since this was considered a sufficient approximation.)

Using Eq. (28) of reference 6 and the notation of the present report, the torsion-bending constant C about an arbitrary center S, Fig. 1, can be computed from the formula

$$C = \int_{u=-u_l}^{u=u_h} w_s{}^2 t\,du - \frac{1}{A+a}\left(\int_{u=-u_l}^{u=u_h} w_s t\,du\right) \tag{1B}$$

where

$$w_s = \int_0^u r_s\,du \tag{2B}$$

r_s is the distance from the center of twist S, Fig. 1, to the tangent line. It should be noted that $w_s = 0$ at the rivet line where $u = 0$. From Fig. 1,

$$r_s = r + s(dy/du) \tag{3B}$$

Substituting this in Eq. (2B) gives

$$w_s = \int_0^u r\,du + \int_0^u s\,(dy/du)\,du$$

giving

$$w_s = w + ys \tag{4B}$$

where

$$w = \int_0^u r\,du \tag{5B}$$

Substituting Eq. (4B) into Eq. (1B) gives

$$C = C_0 + 2Rs + Is^2 \tag{6B}$$

where

$$C_0 = \int_{u=-u_l}^{u=u_h} w^2 t\,du - \frac{1}{A+a}\left(\int_{u=-u_l}^{u=u_h} wt\,du\right)^2$$

$$R = \int_{u=-u_l}^{u=u_h} wyt\,du - \frac{1}{A+a}\times\left(\int_{u=-u_l}^{u=u_h} wt\,du\right)\left(\int_{u=-u_l}^{u=u_h} yt\,du\right)$$

$$I = \int_{u=-u_l}^{u=u_h} y^2 t\,du - \frac{1}{A+a}\left(\int_{u=-u_l}^{u=u_h} yt\,du\right)^2$$

The contribution to C of the bending stiffness in a direction normal to u is unaffected by the presence of the sheet or the location of the center of twist. It can

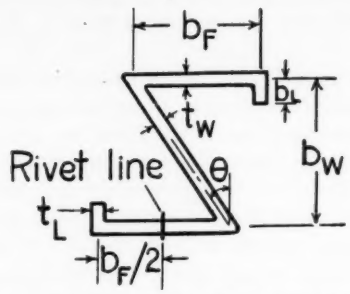

FIG. 5a. Stringers with equal flanges and lips.

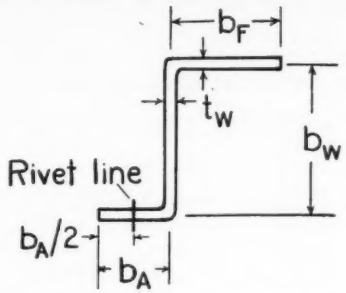

FIG. 5b. Stringers with unequal flanges and no lips.

be computed from Eq. (18), reference 6. The corresponding term in Eq. (1) will be small compared to the other terms, except possibly in the case of short panels using angle stiffeners. In doubtful cases, it should be computed and added to the value of C given in Eqs. (8) and (6B).

APPENDIX C—EVALUATION OF J_p

The quantity J_p is defined as the polar moment of inertia of the section about the center of twist S, Fig. 1. The sheet is taken into account by adding an effective sheet area a to the stringer at the rivet line. Then

$$J_p = \int_{u=-u_l}^{u=u_h} [(s+x)^2 + y^2] t \, du + as^2 \quad (1C)$$

$$= J_{p0} + 2M_y s + (A+a)s^2 \quad (2C)$$

where

$$J_{p0} = \int_{u=-u_l}^{u=u_h} (x^2 + y^2) t \, du$$

$$M_y = \int_{u=-u_l}^{u=u_h} xt \, du$$

$$A = \int_{u=-u_l}^{u=u_h} t \, du$$

APPENDIX D—EVALUATION OF s

In Eq. (10) the value of σ_{cr}/E is given as a function of the section constants and of the distance s from the center of twist to the rivet line. Both the numerator and denominator of the right side of Eq. (10) are functions of s. Let $f_n(s)$ be the numerator and $f_d(s)$ be the denominator; then

$$\sigma_{cr}/E = f_n(s)/f_d(s) \quad (1D)$$

$$\frac{d\left(\frac{\sigma_{cr}}{E}\right)}{ds} = \frac{f_d(s)\frac{df_n(s)}{ds} - f_n(s)\frac{df_d(s)}{ds}}{[f_d(s)]^2} \quad (2D)$$

When σ_{cr}/E is either maximum or minimum $d(\sigma_{cr}/E)/ds = 0$. Applying this to Eq. (2D),

$$f_d(s)[df_n(s)/ds] - f_n(s)[df_d(s)/ds] = 0 \quad (3D)$$

Substituting the numerator and denominator of Eq. (10) for $f_n(s)$ and $f_d(s)$, respectively, in Eq. (3D) gives Eq. (11).

APPENDIX E—CONSTANTS FOR PANELS WITH Z-STRINGERS

(1) Stringers with equal flanges and lips (see Fig. 5a):

$$J_T = {}^1/_3[t_W{}^3(2b_F + b_W) + t_L{}^3(2b_L)]$$

$$A = 2b_L t_L + t_W[2b_F + (b_W/\cos\theta)]$$

$$C_0 = {}^1/_{12}\left[t_W\left(\frac{b_F{}^2 b_W{}^3}{\cos\theta} + b_W{}^2 b_F{}^3\right) + t_L(3b_W{}^2 b_F{}^2 b_L + 10 b_F{}^2 b_L{}^3 + 9 b_W b_F{}^2 b_L{}^2 - 12 b_F b_W b_L{}^3 \tan\theta - 6 b_W{}^2 b_L{}^2 b_F \times \right.$$

$$\left. \tan\theta + 4 b_W{}^2 b_L{}^3 \tan^2\theta)\right] - \frac{1}{A+a}\left[\frac{t_W}{4}\left(\frac{b_F b_W{}^2}{\cos\theta}\right) + t_L\left(\frac{b_W b_L{}^2}{2}\tan\theta - b_L{}^2 b_F - {}^1/_2\, b_W b_F b_L\right)\right]^2$$

(See Eq. (5) for definition of a.)

$$R = {}^1/_6\left[t_L(2b_L{}^3 b_F - 3b_L{}^2 b_F b_W - 3b_W{}^2 b_F b_L + 3b_L{}^2 b_W{}^2 \tan\theta - 2b_L{}^3 b_W \tan\theta) + t_W\left(\frac{b_F b_W{}^3}{\cos\theta}\right)\right] -$$

$$\frac{1}{A+a}\left[\frac{t_W}{4}\left(\frac{b_F b_W{}^2}{\cos\theta}\right) + t_L\left(\frac{b_W b_L{}^2}{2}\tan\theta - b_L{}^2 b_F - {}^1/_2\, b_W b_L b_F\right)\right]\left[t_L(b_W b_L) + t_W\left({}^1/_2\frac{b_W{}^2}{\cos\theta} + b_W b_F\right)\right]$$

$$I = t_L({}^2/_3 b_L{}^3 + b_W{}^2 b_L - b_W b_L{}^2) + t_W\left({}^1/_3\frac{b_W{}^3}{\cos\theta} + b_W{}^2 b_F\right) - \frac{1}{A+a}\left[t_L(b_W b_L) + t_W\left({}^1/_2\frac{b_W{}^2}{\cos\theta} + b_W b_F\right)\right]^2$$

$$M_y = t_L(b_F b_L - b_W b_L \tan\theta) + t_W\left(b_F^2 + {}^1/_2\frac{b_F b_W}{\cos\theta} - b_W b_F \tan\theta - {}^1/_2 b_W^2\frac{\tan\theta}{\cos\theta}\right)$$

$$J_{p0} = t_L\left[{}^5/_2 b_F^2 b_L + b_W^2 b_L \tan^2\theta - 3b_F b_L b_W \tan\theta + {}^2/_3 b_L^3 + b_W^2 b_L - b_W b_L^2\right] + t_W\left[{}^7/_6 b_F^3 + {}^1/_4\frac{b_F^2 b_W}{\cos\theta} + {}^1/_3 b_W^3\frac{\tan^2\theta}{\cos\theta} - {}^1/_2 b_F b_W^2\frac{\tan\theta}{\cos\theta} + b_W^2 b_F\tan^2\theta - 2b_W b_F^2\tan\theta + {}^1/_3\frac{b_W^3}{\cos\theta} + b_W^2 b_F\right]$$

(2) Stringers with unequal flanges and no lips (see Fig. 5b):

$$J_T = ({}^1/_3)t_W^3\,[b_A + b_W + b_F]$$

$$A = t_W[b_A + b_W + b_F]$$

$$C_0 = \frac{t_W}{12}\left[b_A^2 b_W^3 + 3b_A^2 b_F b_W^2 - 6b_A b_W^2 b_F^2 + 4b_W^2 b_F^3\right] - \frac{t_W^2}{A + a}\left[\frac{b_A b_W^2}{4} + \frac{b_A b_W b_F}{2} - \frac{b_W b_F^2}{2}\right]^2$$

(See Eq. (5) for definition of a.)

$$R = \frac{t_W}{6}\left[b_A b_W^3 + 3b_A b_W^2 b_F - 3b_W^2 b_F^2\right] - \frac{t_W^2}{A + a}\left[\frac{b_A b_W^2}{4} + \frac{b_A b_W b_F}{2} - \frac{b_W b_F^2}{2}\right]\left[\frac{b_W^2}{2} + b_W b_F\right]$$

$$I = t_W\left[\frac{b_W^3}{3} + b_W^2 b_F\right] - \frac{t_W^2}{A + a}\left[\frac{b_W^2}{2} + b_W b_F\right]^2$$

$$J_{p0} = t_W\left[\frac{b_A^3}{12} + \frac{b_W^3}{3} + \frac{b_A^2 b_W}{4} + \frac{b_A b_F^2}{2} + \frac{b_A^2 b_F}{4} + b_W^2 b_F + \frac{b_F^3}{3}\right]$$

$$M_y = (t_W/2)[b_F^2 + b_A b_F + b_A b_W]$$

Acknowledgments

Acknowledgment is due to the Bureau of Aeronautics, Navy Department, whose research projects on sheet-stringer panels have provided the impetus and the necessary financial support for the work presented in this paper. The authors take this opportunity to acknowledge also the assistance of members of the Engineering Mechanics Section of the National Bureau of Standards, particularly A. E. Moss and G. Zibritosky, who performed the experimental work for the unpublished test results, groups A and B, used for comparison with the theory.

References

[1] Wagner, Herbert, *Verdrehung und Knickung von offenen Profilen*, pp. 329–343; Festschrift, T. H. Danzig, 1929.

[2] Kappus, Robert, *Drillknicken zentrisch gedrueckter Staebe mit offenem Profil im elastischen Bereich*, Luftfahrtforschung, Vol. 14, No. 9, pp. 444–457, October, 1937.

[3] Lundquist, E. E., and Fligg, C. M., *A Theory for Primary Failure of Straight Centrally Loaded Columns*, N.A.C.A. Rep. 582, 1937.

[4] Goodier, J. N., *Torsional and Flexural Buckling of Bars of Thin-Walled Open Section Under Compressive and Bending Loads*, Journal of Applied Mechanics, A.S.M.E., Vol. 9, No. 3, pp. A103–A107, September, 1942.

[5] Holt, M., *Twisting Failure of Centrally Loaded Open-Section Columns in the Elastic Range*, Alum. Res. Lab. P.T. Report No. 42-37, September 12, 1942.

[6] Ramberg, Walter, and Levy, Samuel, *Instability of Extrusions Under Compressive Loads*, Journal of the Aeronautical Sciences, Vol. 12, No. 4, pp. 485–498, October, 1945.

[7] Weibel, E. E., *Buckling of Stiffener and Elastic Sheet Combinations Under Pure Bending*, Journal of the Aeronautical Sciences, Vol. 12, No. 4, pp. 393–402, October, 1945.

[8] Shanley, F. R., *Inelastic Column Theory*, Journal of the Aeronautical Sciences, Vol. 14, No. 5, pp. 261–267, May, 1947.

[9] Stowell, Elbridge Z., *A Unified Theory of Plastic Buckling of Columns and Plates*, N.A.C.A. T.N. No. 5566, April, 1948.

[10] Levy, Samuel, McPherson, Albert E., and Ramberg, Walter, *Effect of Rivet and Spot-Weld Spacing on the Strength of Axially Loaded Sheet-Stringer Panels of 24S-T Aluminum Alloy*, N.A.C.A. T.N. No. 856, August, 1942.

[11] Niles, Alfred S., *Tests of Flat Panels with Four Types of Stiffeners*, N.A.C.A. T.N. No. 882, January, 1943.

[12] Ramberg, Walter, McPherson, Albert E., and Levy, Samuel, *Experimental Study of Deformation and of Effective Width in Axially Loaded Sheet-Stringer Panels*, N.A.C.A. T.N. No. 684, February, 1939.

[13] Rossman, Carl A., Bartone, Leonard M., and Dobrowski, Charles V., *Compressive Strength of Flat Panels with Z-Section Stiffeners*, N.A.C.A. A.R.R. 4B03, February, 1944; N.A.C.A. Wartime Report L-499.

[14] Timoshenko, S., *Theory of Elastic Stability;* McGraw-Hill Book Company, Inc., New York, 1936.

[15] Levy, Samuel, Goldenberg, Daniel, and Zibritosky, George, *Simply-Supported Long Rectangular Plate Under Combined Axial Load and Normal Pressure*, N.A.C.A. T.N. No. 949, October, 1944.

[16] Woolley, Ruth M., Corrick, Josephine N., and Levy, Samuel, *Clamped Long Rectangular Plate Under Combined Axial Load and Normal Pressure*, N.A.C.A. T.N. No. 1047 June, 1946.

Transient Loading of Airfoils at Supersonic Speeds

JOHN W. MILES*

University of California at Los Angeles

SUMMARY

Using the results for the pressure distribution over a supersonic airfoil due to a harmonic velocity distribution and the Fourier integrals for step and impulse functions, the pressure distribution and lift and moment coefficients have been calculated for the uniform entry of a flat plate into a sharp-edged gust and for the sudden deflection of a flap, the latter including the sudden pitching of the entire airfoil as a special case. Results are given in the form of algebraic equations plus curves for C_L and C_M for $M = 1$, $2^{1/2}$, 2, 4, and ∞.

NOTATION

C_L = lift coefficient, cf. Eq. (17)
C_M = mid-chord moment coefficient, cf. Eq. (25)
G = pressure-velocity Green's function, cf. Eq. (4)
I_n = cf. Eq. (7)
J_n = Bessel function of first kind, nth order
M = Mach Number
U = free-stream velocity
b = semichord
p = gage pressure
$\bar{p}$ = $p[-\rho(U^2/\beta)(w_0/U)]^{-1}$
t = time ($t = 0$ when leading edge meets gust or when flap is deflected)
w = vertical velocity of airfoil
w_0 = gust velocity, positive up
x = dimensionless chord variable, cf. Fig. 2
x_0 = coordinate of leading edge of flap
β = $(M^2 - 1)^{1/2}$
η = cf. Eq. (5)
μ = cf. Eq. (8)
$\bar{\mu}$ = cf. Eq. (13)
μ_0 = cf. Eq. (35)
ν = cf. Eq. (9)
$\bar{\nu}$ = cf. Eq. (33)
ξ = x as a variable of integration
ρ = air mass density
τ = cf. Eq. (19)
τ_0 = cf. Eq. (42)
ω = angular frequency of harmonic oscillation

VELOCITY DISTRIBUTION

THE VELOCITY DISTRIBUTION along an airfoil entering a sharp-edged vertical gust at time zero is given by the unit step function:

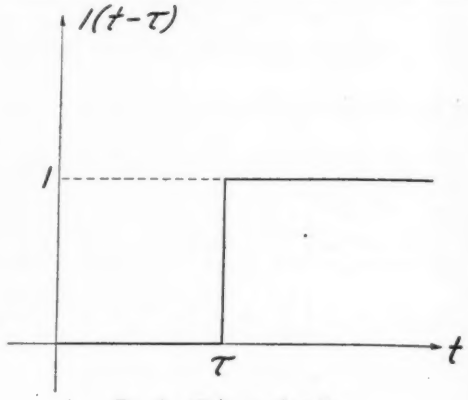

FIG. 1. Unit step function.

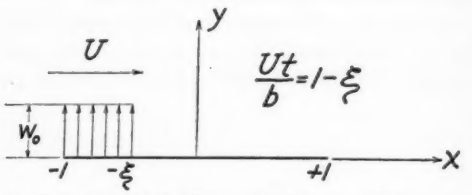

FIG. 2. Velocity distribution on airfoil at $(Ut/b) = 1 - x$.

$$w(x, t) = w_0 1[Ut - (x + 1)] \tag{1}$$

where the airfoil leading and trailing edges are at $x = \mp 1$, respectively, U is the relative wind velocity, and w_0 is the gust velocity. The unit step function is shown in Fig. 1. The leading edge of the airfoil meets the gust at time zero, and the velocity distribution at $Ut = 1 - x$ is shown in Fig. 2.

The unit step function may be expressed analytically by the Fourier integral[1]

$$1(\tau) = \lim_{\epsilon \to 0} \frac{1}{2\pi} \int_{-\infty}^{+\infty} \frac{e^{j\omega\tau}\, d\omega}{\epsilon + j\omega} \tag{2}$$

(Although Eq. (2) is improper for $\omega = 0$, this impropriety may be removed either by expressing Eq. (2) as a contour integral or by transforming to Dirichlet's integral,[1] but neither approach possesses any particular advantage in the present analysis.)

Received October 12, 1947.

* Assistant Professor of Engineering, Department of Engineering.

Pressure Distribution

It has been previously shown[2] that the pressure distribution along a two-dimensional (i.e., infinite span) airfoil due to a harmonic velocity distribution $w(x, t)$ (airfoil relative to fluid) of angular frequency ω is given by

$$p(x, t) = \frac{\rho U}{\beta}\left[w(x, t) + \int_{-1}^{x} w(\xi, t)\frac{\partial G}{\partial x}(x, \xi)d\xi + \frac{j\omega}{U}\int_{-1}^{x} w(\xi, t)G(x, \xi)d\xi\right] \tag{3}$$

$$G(x, \xi) = e^{-jM\omega\eta}J_0(\omega\eta) \tag{4}$$

$$\eta = (M/\beta^2)\,[(x - \xi)/U], \qquad \beta^2 = M^2 - 1 \tag{5}$$

where the notation of reference 2 has been changed slightly by introducing the variable η. Introducing Eqs. (1) and (2) in Eq. (3), partially reversing the order of integration, and taking the limit as ϵ approaches zero yields

$$p(x, t) = -\frac{\rho U^2}{\beta}\left(\frac{w_0}{U}\right)\left\{\mathbf{1}(\mu) - \frac{1}{2\pi\beta^2 U}\int_{-1}^{x}[I_0(x, \xi) - jMI_1(x, \xi)]d\xi\right\} \tag{6}$$

$$I_n = \int_{-\infty}^{+\infty} e^{-j\nu\omega}J_n(\eta\omega)d\omega \tag{7}$$

$$\mu = 1 - [(\xi + 1)/Ut] \tag{8}$$

$$\nu = M\eta - \mu t \tag{9}$$

The integral (7) may be evaluated from the standard result[3]

$$\int_0^{\infty} e^{-j\nu\omega}J_n(\eta\omega)d\omega = (\eta^2 - \nu^2)^{-1/2}\left\{[(\eta^2 - \nu^2)^{1/2} - j\nu]/\eta\right\}^n \tag{10}$$

where the positive root is taken if $\eta^2 > \nu^2$, and the positive imaginary root if $\eta^2 < \nu^2$. Using Eq. (10) it is found that

$$\begin{aligned} I_0 &= 2(\eta^2 - \nu^2)^{-1/2}, && \eta^2 > \nu^2 \\ &= 0, && \eta^2 < \nu^2 \\ I_1 &= -2j(\nu/\eta)\,(\eta^2 - \nu^2)^{-1/2}, && \eta^2 > \nu^2 \\ &= 0, && \eta^2 < \nu^2 \end{aligned} \tag{11}$$

Substituting Eq. (11) in Eq. (6) yields

$$p(x, t)\Big/\left[-\rho\frac{U^2}{\beta}\left(\frac{w_0}{U}\right)\right] = \bar{p}\,(x, t) = \left[\mathbf{1}(\bar{\mu}) - \frac{1}{\pi\beta^2 U}\,Rl\int_{-1}^{x}\left(1 - M\frac{\nu}{\eta}\right)(\eta^2 - \nu^2)^{-1/2}\,d\xi\right] \tag{12}$$

$$\bar{\mu} = 1 - [(x + 1)/Ut] \tag{13}$$

where only the real part of the integral is to be included in accordance with Eq. (11). Introducing the change of variable

$$u = \nu/\eta = u(x, \xi) \tag{14}$$

in Eq. (12) and observing that the integral in Eq. (12) is real only if u has a magnitude less than unity yields

$$\bar{p}(x, t) = [\mathbf{1}(\bar{\mu}) - (1/\pi)\textstyle\int_{-1}^{u(x,\,-1)}(1 - u^2)^{-1/2}\,du] \tag{15}$$

On carrying out the integration in Eq. (15), it is expedient to plot the variation of the variable u as the variable ξ is brought from the leading edge (-1) to the point at which the pressure is calculated (x). Eq. (14) may be regarded as a family of curves for each value of x, giving $\bar{\mu}$ as a function of ξ, where $\bar{\mu}$ is the family parameter. Actually, it is more convenient to plot Ut vs. ξ, since the curves are then straight lines. The points of interest are bounded by $\xi = -1$ and x and $u = \mp 1$, as shown in Fig. 3. It will be observed that the intersections of $u = \mp 1$ with $\xi = -1$ occur

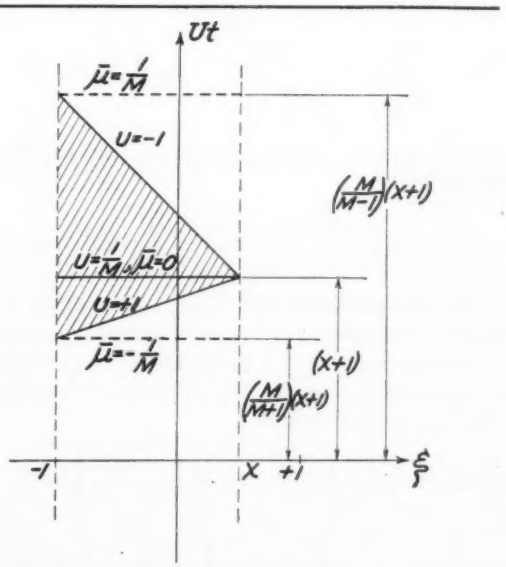

FIG. 3. Ut vs. ξ as given by Eq. (14).

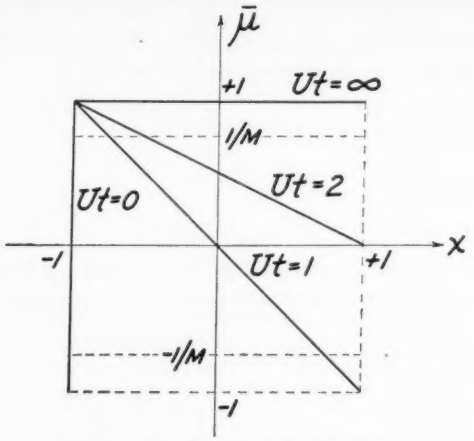

FIG. 4. $\bar{\mu}$ vs. x as given by Eq. (13).

at $\bar{\mu} = \pm 1/M$, respectively while $u = \pm 1$ and $\xi = x$ intersect at $\bar{\mu} = 0$. Hence, for any fixed time, the integration is carried out over a horizontal line in the shaded area of Fig. 3, and, if $\bar{\mu} < 0$, the lower limit of u in Eq. (15) is -1 and $\mathbf{1}(\bar{\mu}) = 1$, while, if $\bar{\mu} < 0$, the lower limit is $+1$ and $1(\bar{\mu}) = 0$. The result of integrating Eq. (15) is then

$$p(x, t) = 0, \qquad \bar{\mu} < -(1/M) \tag{16a}$$

$$= \frac{1}{\pi} \cos^{-1}\left[\frac{1 - M^2\bar{\mu}}{M(1 - \bar{\mu})}\right], \quad -\frac{1}{M} < \bar{\mu} < \frac{1}{M} \tag{16b}$$

$$= 1, \qquad \bar{\mu} > 1/M \tag{16c}$$

Lift Coefficient Due to Gust

Since the chord of the airfoil is 2, the lift coefficient is given by (since the pressure jump is $-2\bar{p}$):

$$C_{Lw} = \frac{\partial C_L}{\partial\left(\frac{w_0}{U}\right)} = \frac{L(t)}{\frac{1}{2}\rho U^2\left(\frac{w_0}{U}\right)2} = \frac{2}{\beta}\int_{-1}^{+1} \bar{p}(x)dx \tag{17}$$

Introducing the variable $\bar{\mu}$ from Eq. (13), Eq. (17) may be written

$$(\beta/4)C_{Lw} = (Ut/2)\int_\tau \bar{p}(\bar{\mu})d\bar{\mu} \tag{18}$$

$$\tau = 1 - (2/Ut) \tag{19}$$

The integral in Eq. (18) must be evaluated in three parts, corresponding to the three different pressure distributions of Eq. (16). To facilitate these integrations, $\bar{\mu}$ is plotted vs. x for various Ut in Fig. 4. Substituting Eq. (16) in Eq. (18) yields

$$\frac{\beta}{4} C_{Lw} = \frac{Ut}{2}\left\{\frac{1}{\pi}\int_{-1/M}^{+1/M} \cos^{-1}\left[\frac{1 - M^2\bar{\mu}}{M(1 - \bar{\mu})}\right] d\bar{\mu} + \int_{1/M}^{1} d\bar{\mu}\right\}, \quad \tau < -\frac{1}{M} \tag{20a}$$

$$= \frac{Ut}{2}\left\{\frac{1}{\pi}\int_{\tau}^{1/M} \cos^{-1}\left[\frac{1 - M^2\bar{\mu}}{M(1 - \bar{\mu})}\right] d\bar{\mu} + \int_{1/M}^{1} d\bar{\mu}\right\}, \quad -\frac{1}{M} < \tau < \frac{1}{M} \tag{20b}$$

$$= (Ut/2)\int_\tau^1 d\bar{\mu}, \qquad \tau > (1/M) \tag{20c}$$

The integral involving the arc cosine may be evaluated by introducing the change of variable

$$u(\bar{\mu}) = (1 - M^2\bar{\mu})/M(1 - \bar{\mu}) \tag{21}$$

whence

$$\frac{1}{\pi}\int_\tau^{1/M} \cos^{-1}\left[\frac{1 - M^2\bar{\mu}}{M(1 - \bar{\mu})}\right] d\bar{\mu} = \frac{\beta^2}{M\pi}\int_{-1}^{u(\tau)} \frac{\cos^{-1} u\, du}{(M - u)^2} = \frac{\beta^2}{M\pi}\left[\frac{\cos^{-1} u}{(M - u)}\right]^{u(\tau)} + \int_{-1}^{u(t)} (1 - u^2)^{-1/2}(M - u)^{-1} du\Bigg] =$$

$$\left\{\frac{1}{\pi}\frac{\cos^{-1}\left[M - \frac{\beta^2}{M}\left(\frac{Ut}{2}\right)\right]}{(Ut/2)} - \left(\frac{M - 1}{M}\right) + \frac{\beta}{2M}\left[1 - \frac{2}{\pi}\sin^{-1}(M\tau)\right]\right\} \tag{22}$$

$$\int_{1/M}^1 d\bar{\mu} = [(M - 1)/M] \tag{23}$$

where the last integral is given by Peirce 195.[4]

Substituting Eqs. (22) and (23) in Eq. (20) yields

$$\frac{\beta}{4} C_{Lw} = \left(\frac{\beta}{M}\right)\left(\frac{Ut}{2}\right), \quad \tau < -\frac{1}{M} \tag{24a}$$

$$= \left\{\frac{1}{\pi}\cos^{-1}\left[M - \frac{\beta^2}{M}\left(\frac{Ut}{2}\right)\right] + \left(\frac{\beta}{2M}\right)\left(\frac{Ut}{2}\right)\times\left[1 - \frac{2}{\pi}\sin^{-1}(M\tau)\right]\right\}, \quad -\frac{1}{M} < \tau < \frac{1}{M} \tag{24b}$$

$$= 1, \qquad \tau > (1/M) \tag{24c}$$

The values of $(\beta/4)C_{Lw}$ given by Eq. (24) are plotted vs. $(Ut/2b)$ for $M = 1, 2^{1/2}, 2, 4$, and ∞ in Fig. 5, where b is the semichord.

Moment Coefficient Due to Gust

The mid-chord moment coefficient (positive stalling) is defined by

$$C_{Mw} = \frac{\partial C_M}{\partial(w_0/U)} = \frac{M(t)}{{}^1/_2\rho U^2(w_0/U)2^2} = -\frac{1}{\beta}\int_{-1}^{1} x\bar{p}(x)dx \tag{25}$$

Introducing Eq. (13) yields

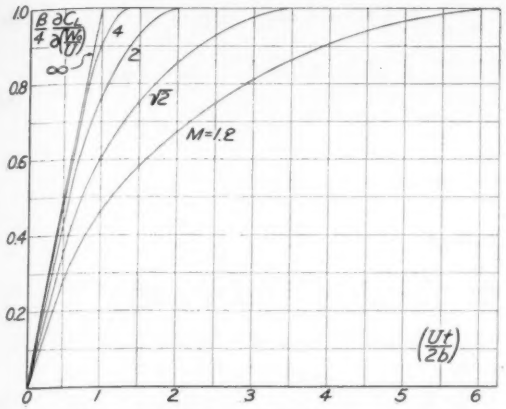

FIG. 5. $(\beta/4)\partial C_L/\partial(w_0/U)$ vs. $(Ut/2b)$ as given by Eq. (24).

$$\frac{\beta}{2} C_{Mw} = \frac{\beta}{4} C_{Lw} - \frac{1}{2}(Ut)^2 \int_\tau^1 (1 - \bar{\mu})\bar{p}(\bar{\mu})d\bar{\mu} \quad (26)$$

As in the case of Eq. (20), Eq. (26) must be evaluated separately for three different ranges of the parameter τ.

The integral involving Eq. (16b) is

$$\frac{1}{\pi}\int_\tau^{1/M} (1 - \bar{\mu}) \cos^{-1}\left[\frac{1 - M^2\bar{\mu}}{M(1 - \bar{\mu})}\right] d\bar{\mu} =$$

$$\frac{\beta^4}{\pi M^2}\int_{-1}^{u(\tau)} \frac{\cos^{-1} u du}{(M - u)^3} = \frac{-\beta^4}{2\pi M^2}\frac{\partial}{\partial M}\int_{-1}^{u(\tau)} \frac{\cos^{-1} u\, du}{(M - u)^2} \quad (27)$$

where the last integral may then be obtained by differentiating the integral in Eq. (22) with respect to M, treating $u(\tau)$ as independent of M during this operation. Substituting the results in Eq. (26) yields

$$\frac{M}{2} C_{Mw} = \left(\frac{Ut}{2}\right)\left(1 - \frac{Ut}{2}\right), \qquad \tau < -(1/M) \quad (28a)$$

$$= \frac{1}{2}\left(\frac{Ut}{2}\right)\left(1 - \frac{Ut}{2}\right)\left[1 - \frac{2}{\pi}\sin^{-1}(M\tau)\right] + \left(\frac{Ut}{2}\right)^2\left(\frac{1}{M^2} - \tau^2\right)^{1/2}, \quad -\frac{1}{M} < \tau < \frac{1}{M} \quad (28b)$$

$$= 0, \qquad \tau > (1/M) \quad (28c)$$

The values of $2\beta C_{Mw}$ given by Eq. (28) are plotted vs. $(Ut/2b)$ for $M = 1$, $2^{1/2}$, 2, 4, and ∞ in Fig. 6. Although it might be more logical to plot $(\beta/2)C_{Mw}$ (since all supersonic pressure coefficients presumably vary as $1/\beta$), it is evidently more convenient to use $(2/M)$ as the reference quantity.

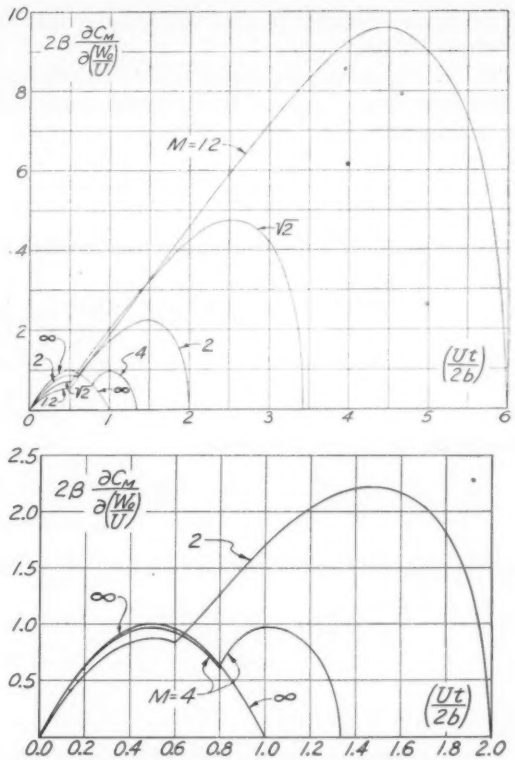

FIG. 6. $2\beta\partial C_M/\partial(w_0/U)$ as given by Eq. (28).

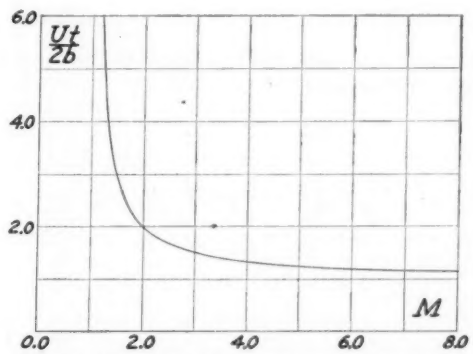

FIG. 7. $(Ut/2b)$ vs. M for attainment of total lift.

TIME TO REACH FULL LIFT

Full lift and corresponding zero mid-chord moment are reached at $\tau = 1/M$ or

$$(Ut/2b) = \left[\frac{M}{(M - 1)}\right] \quad (29)$$

so that equilibrium is attained as the airfoil just finishes entering the gust only for high Mach Numbers, with an increasing delay at small Mach Numbers (although the linearized theory used in the calculations of course breaks down on Mach Numbers too close to unity).

A plot of Eq. (29) is given in Fig. 7.

SUDDEN CHANGE IN ANGLE OF ATTACK

A problem quite analogous to the foregoing is the sudden change in angle of attack of some portion of the airfoil. If the sudden change of angle occurs over the entire chord it corresponds to a sudden gust loading over

the chord, as contrasted to the uniform entry into the gust treated in the foregoing.

The velocity distribution over the airfoil due to a sudden increase α_0 of angle of attack at time t_0 and location ξ_0 is given by

$$w(\xi, t) = U\alpha_0\delta(\xi - \xi_0)\, 1\,(t - t_0) \tag{30}$$

$$\left.\begin{aligned}\delta(\xi - \xi_0) &= 1, \quad \xi = \xi_0\\ &= 0, \quad \xi \neq \xi_0\end{aligned}\right\} \tag{31}$$

The pressure distribution is then given by modifying Eq. (6) to read

$$p(x, t) = -\frac{\rho U^2}{\beta}\,\alpha_0\left\{\delta(x - \xi_0) - \frac{1}{2\pi\beta^2 U}\int_{-1}^{x}\delta(\xi - \xi_0)\,[I_0(x, \xi) - jMI_1(x, \xi)]d\xi\right\} \tag{32}$$

where I_0 and I_1 are given by Eq. (11) if only ν is replaced by

$$\bar{\nu} = M\eta - (t - t_0) \tag{33}$$

Introducing the change of variable

$$w = 1 - [(x - \xi)/U(t - t_0)] \tag{34}$$

$$\mu_0 = 1 - [(x + 1)/U(t - t_0)] \tag{35}$$

and assuming that t_0 is independent of ξ_0 then yields the result

$$p(x, t) = -\frac{\rho U^2}{\beta}\,\alpha_0\left[\delta(x - \xi_0) - \frac{\beta}{\pi}Rl\int_{\mu_0}^{1}\delta(w - w_0)\,(1 - w)^{-1}\,(1 - M^2w^2)^{-1/2}\,dw + \frac{\beta}{\pi}Rl\int_{\mu_0}^{1}\delta(w - w_0)\,(1 - M^2w^2)^{-1/2}dw\right] \tag{36}$$

More general results may be obtained by specifying a velocity distribution with an appropriate dependence of t_0 on ξ_0, the previously treated entry of a sharp-edged gust being a special example.

Sudden Flap Deflection

The result, Eq. (36), will be applied to the sudden deflection of a flap extending from $x = x_0$ to $x = 1$, in which case Eq. (36) becomes

$$p(x, t) = 0, \; x < x_0 \tag{37a}$$

$$p(x, t) = -\frac{\rho U^2}{\beta}\,\alpha_0\left[1 - \frac{\beta}{\pi}Rl\int_{\mu_0}^{1}(1 - w)^{-1}\,(1 - M^2w^2)^{-1/2}\,dw + \frac{\beta}{\pi}Rl\int_{\bar{\mu}_0}^{1}(1 - M^2w^2)^{-1/2}\,dw\right], x > x_0 \tag{37b}$$

$$\bar{\mu}_0 = 1 - [(x - x_0)/Ut] \tag{38}$$

The evaluation of Eq. (37) is analogous to the evaluation of Eqs. (15) and (22) and leads to the following results (for $x > x_0$):

$$p(x, t) = -(\rho U^2/\beta)\alpha_0(\beta/M), \qquad \bar{\mu}_0 < -(1/M) \tag{39a}$$

$$= -\frac{\rho U^2}{\beta}\,\alpha_0\left\{\frac{1}{2} - \frac{1}{\pi}\tan^{-1}\left[\frac{(1 - M^2\bar{\mu}_0)}{\beta(1 - M^2\bar{\mu}_0^2)^{1/2}}\right] + \frac{\beta}{2M}\left[1 - \frac{2}{\pi}\sin^{-1}(M\,\bar{\mu}_0)\right]\right\}, \; -\frac{1}{M} < \bar{\mu}_0 < \frac{1}{M} \tag{39b}$$

$$= -(\rho U^2/\beta)\,\alpha_0, \qquad \bar{\mu}_0 > (1/M) \tag{39c}$$

The lift coefficient due to Eq. (36) is found to be

$$C_{L\alpha_0} = \frac{2(1 - x_0)}{\beta}\left\{1 - \frac{\beta}{\pi}Rl\left[\int_{r_0}^{1}(1 - \bar{\mu}_0)^{-1}\,(1 - M^2\,\bar{\mu}_0^2)^{-1/2}\,d\bar{\mu}_0 - \int_{r_0}^{1}(1 - M^2\,\bar{\mu}_0^2)^{-1/2}\,d\bar{\mu}_0 - \left(\frac{Ut}{1 - x_0}\right)\int_{r_0}^{1}\bar{\mu}_0\,(1 - M^2\bar{\mu}_0^2)^{-1/2}\,d\bar{\mu}_0\right]\right\} \tag{40}$$

$$C_{L\alpha_0} = [2(1 - x_0)/\beta]\ (\beta/M), \qquad \tau_0 < -(1/M) \tag{41a}$$

$$= \left[\frac{2(1-x_0)}{\beta}\right]\left\{\frac{1}{2} - \frac{1}{\pi}\tan^{-1}\left[\frac{(1 - M^2\tau_0)}{\beta(1 - M^2\tau_0^2)^{1/2}}\right] + \frac{\beta}{2M}\left[1 - \frac{2}{\pi}\sin^{-1}(M\tau_0)\right] + \frac{\beta}{\pi M^2}\frac{(1 - M^2\tau_0^2)^{1/2}}{(1 - \tau_0)}\right\},$$

$$-\frac{1}{M} < \dot{\tau}_0 < \frac{1}{M} \tag{41b}$$

$$= 2(1 - x_0)/\beta, \qquad \tau_0 < (1/M) \tag{41c}$$

$$\tau_0 = 1 - [(1 - x_0)/Ut] \tag{42}$$

It may be observed that, if $(\beta/2)(1 - x_0)^{-1}(\partial C_L/\partial\alpha_0)$ is plotted vs. $[Ut/(1 - x_0)b]$ (the time in flap lengths), the result is independent of x_0. This result is plotted in Fig. 8 for $M = 1.2, 2^{1/2}$, and 2.

The mid-chord pitching moment coefficient due to Eq. (37) is given by

$$C_{M\alpha_0} = \frac{1}{\beta}\left\{-\left(\frac{1 - x_0^2}{2}\right) + \frac{\beta}{\pi}Rl\left[\left(\frac{1 - x_0^2}{2}\right)\int_{\tau_0}^{1}(1 - \bar{\mu}_0)^{-1}\,d\bar{\mu}_0 - \left(\frac{1 - x_0^2}{2}\right)\int_{\tau_0}^{1}(1 - M^2\bar{\mu}_0^2)^{-1/2}\,d\bar{\mu}_0 - \right.\right.$$

$$\left.\left. Utx_0\int_{\tau_0}^{1}\bar{\mu}_0(1 - M^2\bar{\mu}_0^2)^{-1/2}\,d\bar{\mu}_0 - \frac{1}{2}(Ut)^2\int_{\tau_0}^{1}\bar{\mu}_0(1 - \bar{\mu}_0)(1 - M^2\bar{\mu}_0^2)^{-1/2}\,d\bar{\mu}_0\right]\right\} \tag{43}$$

$$C_{M\alpha_0} = -\frac{1}{\beta}\left(\frac{1 - x_0^2}{2}\right)\left\{\left(\frac{\beta}{M}\right)\left[1 - \frac{1}{2M^2}\frac{(Ut)^2}{(1 - x_0^2)}\right]\right\}, \quad \tau_0 < -\frac{1}{M} \tag{44a}$$

$$= -\frac{1}{\beta}\left(\frac{1 - x_0^2}{2}\right)\left\{\frac{1}{2} - \frac{1}{\pi}\tan^{-1}\left[\frac{(1 - M^2\tau_0)}{\beta(1 - M^2\tau_0^2)^{1/2}}\right] + \frac{\beta}{2M}\left[1 - \frac{1}{2M^2}\frac{(Ut)^2}{(1 - x_0^2)}\right]\left[1 - \frac{2}{\pi}\sin^{-1}(M\tau_0)\right] + \right.$$

$$\left.\frac{\beta Ut}{2\pi M^2(1 - x_0^2)}(3x_0 + 1 + Ut)(1 - M^2\tau_0^2)^{1/2}\right\}, \quad -\frac{1}{M} < \tau_0 < \frac{1}{M} \tag{44b}$$

$$= -(1/\beta)[(1 - x_0^2)/2], \qquad \tau_0 > (1/M) \tag{44c}$$

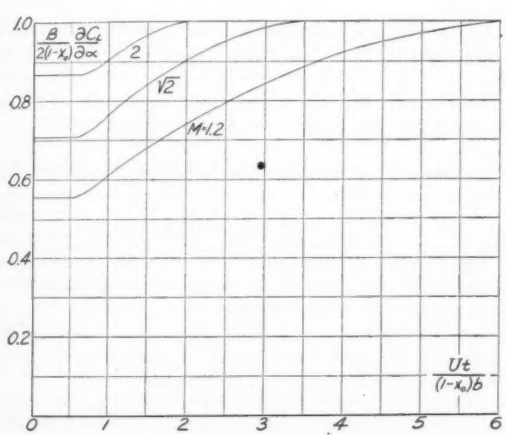

FIG. 8. $(\beta/2)(1 - x_0)^{-1}\,\partial C_L/\partial\alpha_0$ as given by Eq. (41).

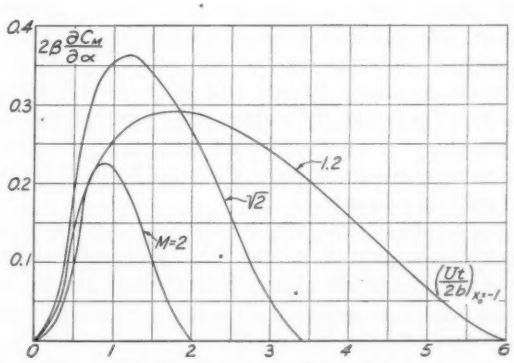

FIG. 9. $2\beta\partial C_M/\partial\alpha_0$ as given by Eq. (44) for $x_0 = -1$.

Evidently the behavior of $\partial C_M/\partial\,\alpha_0$ is sensitive to the value of x_0, and it is not possible to draw a universal curve, as in the case of $\partial C_L/\partial\alpha_0$. In Fig. 9, $2\beta(\partial C_M \div \partial\alpha_0)$ is plotted vs. $(Ut/2b)$ for $x_0 = -1$ and for $M = 1.2, 2^{1/2}$, and 2, corresponding to a suddenly imposed angle of attack of the entire airfoil. In Fig. 10, $2\beta(\partial C_M/\partial\alpha_0)/(1 - x_0^2)$ is plotted vs. $(Ut)/(1 - x_0)b$ for $x_0 = 0$ and for $M = 1.2, 2^{1/2}$, and 2, corresponding to the sudden deflection of a 50 per cent chord flap. It does not appear that the transient behavior of a super-

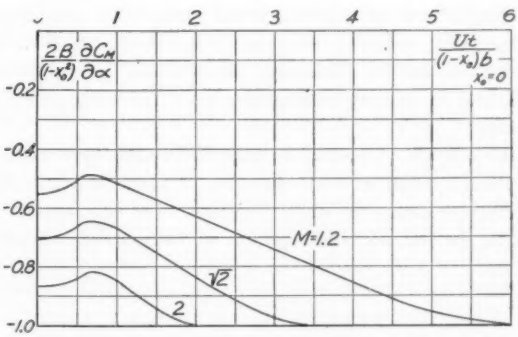

FIG. 10. $2\beta\partial C_M/\partial\alpha_0$ as given by Eq. (44) for $x_0 = 0$.

sonic airplane due to sudden pitching or flap deflection will present serious problems unless dynamic stability is marginal (except very close to $M = 1$, where the foregoing calculations are probably not too reliable).

The time in flap lengths $Ut(1 - x_0)^{-1}b^{-1}$ required for attainment of full lift and moment is evidently given by Eq. (27) and Fig. 7.

Comparison of Gust Entry and Sudden Angle of Attack

It is of interest to compare the results of Eqs. (24) and (28) with those Eqs. of (41) and (44) for $x_0 = -1$, the former representing the uniform penetration of a sharp-edged gust and the latter representing either the sudden application of an angle of attack $\alpha_0 = w_0/U$ or the sudden application of a gust w_0 over the entire chord at time zero. While the eventual lift and moment coefficients and time required to attain these coefficients is the same in both cases, the manner in which they are reached is quite different, the initial lift being finite in the latter problem.

Comparison with Subsonic Case

The incompressible transient loading problem differs markedly from the supersonic problem because of the influence of the wake in the former problem. It has been treated by Küssner,[5,6] Wagner,[7] Bryant and Jones,[8] and von Kármán and Sears.[9] Küssner treated the problem both theoretically[5] and experimentally;[6] Wagner treated the general problem of transient loading; Bryant and Jones used Wagner's results to compute the sudden imposition of the gust to the entire chord (i.e., the second problem treated in the present paper); and von Kármán and Sears treated the uniform gust entry.

The results of von Kármán and Sears for the lift coefficient are plotted in Fig. 11. Inasmuch as they proved that the lift always acts through the quarter chord during the gust entry, the quarter chord moment coefficient vanishes identically.

Extension to More General Loadings

The effects of more general gusts (i.e., not sharp-edged and uniform) may be calculated from the foregoing results by Duhamel integration.[1] A graphical method of accomplishing this end has been given by Jones.[10]

Bryant and Jones[8] have included elastic and stability considerations in their subsonic treatment, and their techniques may be used, together with the present results, to include such effects in the supersonic problem.

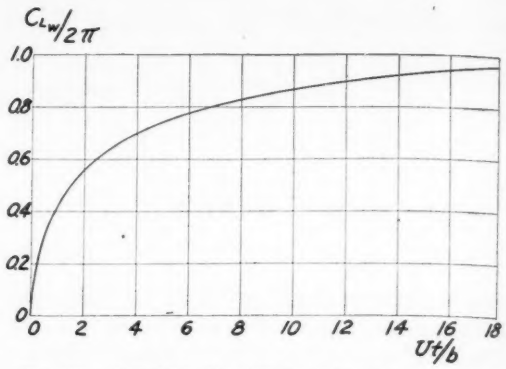

FIG. 11. $(1/2\pi)\partial C_L/\partial(w_0/U)$ for subsonic gust entry.

Recent Work

Since the foregoing was written, an A.A.F. translation of a paper by Schwarz[11] has appeared which contains the result, Eq. (16), and a general analysis similar to that of reference 2.

References

[1] von Kármán and Biot, *Mathematical Methods in Engineering;* McGraw-Hill Book Company, Inc., New York, 1940.

[2] Miles, J. W., *Aerodynamic Forces on an Oscillating Airfoil at Supersonic Speeds,* Journal of the Aeronautical Sciences, Vol. 14 No. 6 pp. 357–358 June 1947.

[3] Gray, Mathews and MacRobert, *Bessel Functions;* Macmillan and Co., London, 1931.

[4] Peirce, B. O., *A Short Table of Integrals;* Ginn and Co., New York, 1929.

[5] Küssner, H. G., *Zusammenfassender Bericht über den unstationären Auftrieb von Flugen,* Luftfahrtforschung Bd. 13, p. 410 1936.

[6] Küssner H. G., *Untersuchung der Bewegung einer Platte beim Eintritt ins ein Strahlgrenze,* Luftfahrtforschung, Bd. 13 p. 425, 1936.

[7] Wagner, H., *Dynamischer Auftrieb von Tragflügeln;* Z.A.-M.M., Bd. 5, p. 17, 1925.

[8] Bryant, L. W., and Jones, I. M. W., *Stressing of Aeroplane Wings Due to Symmetrical Gusts,* Brit. A.R.C., R & M 1690, 1936.

[9] von Kármán, T., and Sears, W. R. *"Airfoil Theory for Non-Uniform Motion,* Journal of the Aeronautical Sciences, Vol. 5, No. 10, pp. 379–380, August, 1938.

[10] Jones, R. T., *Calculation of the Motion of an Airplane Under the Influence of Irregular Disturbances,* Journal of the Aeronautical Sciences, Vol. 3 No. 12 p. 419, October, 1936.

[11] Schwarz L., *Plane Non-stationary Theory of the Wing at Supersonic Speed,* an Abstract of a Report with the Same Title, *U.S.A.A.F.* Translation F-TS-934-RE, Wright Field, March, 1947.

[12] Chang, C. C., *The Transient Reaction of an Airfoil Due to Change in Angle of Attack at Supersonic Speed,* I.A.S. Preprint No. 134.

[13] Biot, M. A., *Loads on a Supersonic Wing Striking a Sharp Edged Gust,* Cornell Aero. Lab. Report SA-247-S-7, January 17, 1948.

[14] Heaslet, M. A., and Lomax, H., *Two-Dimensional Unsteady Lift Problems in Supersonic Flight,* N.A.C.A. T.N. No. 1261, June, 1948.

Plastic Flow Characteristics of Aluminum-Alloy Plate*

L. J. KLINGLER† AND G. SACHS†

Case Institute of Technology

ABSTRACT

Commercial hot-rolled $1^1/_2$-in. 24ST aluminum plate possesses a marked degree of crystallographic anisotropy. Tensile tests at various orientations showed that the yield strength is only slightly dependent upon the crystallographic anisotropy. Ratios of the transverse strains to the longitudinal strain varied from -0.30 to -0.57, while for an isotropic material the ratio would be -0.50.

INTRODUCTION

TWO TYPES OF ANISOTROPY may be encountered in annealed metal. "Crystallographic anisotropy" results from a preferred orientation or "texture" in the crystal structure of the metal, while "mechanical anisotropy" results from a geometrically directional arrangement of certain phases, inclusions, porosities, cracks, etc. In addition to these two, any cold-worked metal develops a third type of anisotropy which may be termed "anelastic anisotropy." This type appears to be caused by a certain kind of residual stresses set up during the cold working. It can be reduced and seemingly eliminated by a stress relief anneal. A paper has been published recently[1] which discusses this type of anisotropy.

This paper will deal only with the first of these types—namely, the effect of the crystallographic anisotropy on the plastic flow properties.

Crystallographic anisotropy develops gradually in an initially (apparently) isotropic metal in proportion to the total reduction. This has been shown repeatedly by means of both tensile tests[2, 3] and x-ray investigations.[4, 5] Annealing a cold-worked metal results either in partial retention of the previous anisotropy or in the development of a new type of anisotropy. The relation between these annealing and cold-work textures is not definitely known.[4]

The degree of anisotropy in annealed metal depends upon a variety of factors, the most important of which are the following, listed in the order of decreasing importance: (1) degree of cold work, (2) temperature of the final anneal, and (3) temperature of the (penultimate) anneal before the final cold work.

Received May 13, 1948.

* The work reported in this paper was made possible by the Frederick Cottrell grant received from the Research Corporation, New York.

† Metals Research Laboratory.

The degree of anisotropy increases as the temperature of the final anneal increases and as the temperature of the penultimate anneal decreases. Generally, a metal reduced by more than 80 per cent in cold rolling or drawing, and subsequently annealed, exhibits a pronounced annealing texture.[5] However, certain metals have a low tendency to develop an annealing texture, probably because they contain heterogeneous particles (impurities, hard phases, oxides, etc.).

Materials subjected to hot work (rather than cold work) may be substantially free from crystallographic orientation and anisotropy. However, little is known about how hot working affects these phenomena. A few investigations on hot-rolled steel strip[6, 7] show the development of preferred orientation to be especially evident when the rolling was carried out below the A_3 temperature. The degree of preferred orientation was found to increase with the per cent reduction. The developed structure was found to be difficult to remove by heat-treatment.

At present, it is not known whether a wrought metal product can be obtained with such a low degree of crystallographic anisotropy that the deviations cannot be revealed by the common methods of testing.

To obtain a uniform piece of metal suitable for accurate fundamental investigations, it is general practice to process it from a cast ingot by a sequence of hot working, cold working, and annealing operations. In such a wrought metal product the type and magnitude of anisotropy, or directionality, is determined primarily by the two last operations as discussed above and, to a gradually decreasing degree, upon the preceding operations.

The laws of plasticity have been based on the assumption that a metallic body can be considered as isotropic. However, since it is known that metals may be highly anisotropic, it is not certain whether the test results offered as proof of certain laws of plasticity were influenced by anisotropy. Lode's tests[8] on tubes under internal pressure and longitudinal tension showed definite evidence of anisotropy, since the radial and circumferential strains were not equal for the case of pure longitudinal tension (pressure equal to zero). Taylor and Quinney,[9] in their tests on tubes subjected to torsion and tension, discarded materials that deviated considerably from complete isotropy as measured by change in volume of tubes under tension. However, all the tubes investigated showed some change in vol-

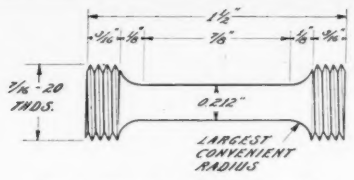

FIG. 1: TENSILE TEST SPECIMEN.

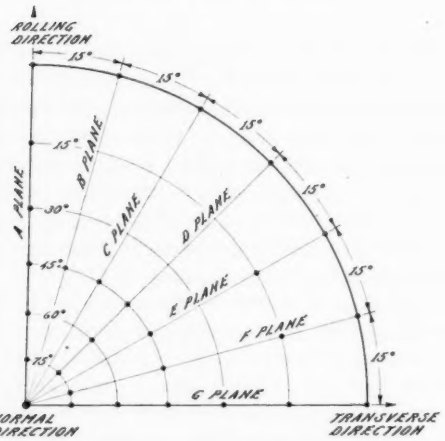

FIG. 2: STEREOGRAPHIC PROJECTION SHOWING ORIENTATION OF THE TEST SPECIMENS. POINTS REPRESENT THE SPECIMEN AXES.

ume, indicating that the radial and circumferential strains were not exactly equal.

No definite information is available on the effect of anisotropy on plastic flow. An attempt by Dorn[10, 11] to establish certain relations for sheet possessing different types of anisotropy has not yet progressed sufficiently to account for either the anisotropy in yield strength or the anisotropy in plastic flow which are observed.

It must be assumed, at the outset, that crystallographic anisotropy of a sheet (or plate) originates in the anisotropy of the crystallites. Single crystals are highly anisotropic;[12] face centered cubic crystals, for example, possess flow stresses in uniaxial tension which may differ in the ratio of almost two to one, depending upon their orientation.[13] A single crystal subjected to uniaxial tension generally strains so that the strain in one transverse direction is nearly zero—i.e., very much smaller than in the other transverse direction. Therefore, these features of anisotropy should be retained, over the limits of normal accuracy, in a commercial metal if it is to be considered anisotropic.

In commercial sheet the directionality in flow stress and the unequality of the two transverse strains, therefore, can be used as measures of the degree of crystallographic anisotropy.

This paper will report on the effect of the crystallographic anisotropy on the plastic flow properties of tension specimens taken at various orientations in a commercial 24ST aluminum-alloy plate.

Material and Procedure

A distribution of properties was made on a commercial $1^1/_2$-in. 24ST aluminum plate. The working schedule for $1^1/_2$-in. plate calls for hot rolling to size from the ingot, heat-treating, followed by cold straightening. The straightening process, however, amounts to less than 1 per cent cold work.

All tests were made on $1^1/_2$-in. threaded-end tensile specimens, as shown in Fig. 1.

The orientations of the specimens cut out of the plate are shown on the stereographic projection, Fig. 2. Points on this projection represent the intersection of straight lines from the center of the stereographic sphere with the surface of the sphere. The points may then be considered to represent the longitudinal axes of the specimens.

The positions of the specimens can be more easily identified by passing planes normal to the rolled surface of the plate at increments of 15° to the rolling direction. Thus, in this system, plane *A* is defined by the rolling direction and the normal direction, plane *B* is defined by a line in the rolling plane at 15° from the rolling direction and by the normal direction, and so forth to plane *G*, which is defined by the transverse and normal directions. Any specimen can then be located by giving the plane designation and the angle of elevation of the specimen axis from the rolling plane.

A number was stamped and a line was scribed on the end of each specimen blank after it was sawed from the plate, so that a record of its original position in the plate could be kept. All specimens were made in duplicate, the test section in all cases being taken in the middle of the plate. Some tests were discarded because of faulty technique, and some additional tests were made as checks.

All specimens were reheat-treated after machining, in the following manner: solution treatment, 920°F. for 45 min.; cold water quench; aged at least 4 days at room temperature. This treatment was carried out to standardize the heat-treatment of all the specimens and to remove any residual effects of machining.

The changes in diameter (from which the strains were calculated) were measured to the nearest 0.0001 in. with a vernier micrometer.

All of the specimens tested were found to exhibit one of the transverse principal strains, either the maximum or the minimum change in diameter, in a direction parallel to the rolling plane. This strain was designated as ϵ_2, with ϵ_1 being the strain along the longitudinal axis of the specimens and ϵ_3 being the third principal strain.*

Stress-strain curves were plotted of stress† versus the two principal transverse strains (conventional), as

* ϵ_1, ϵ_2, and ϵ_3 are the natural plastic strains, being defined as $\epsilon_1 = \ln(1 + e_1) \ldots$, etc., where e_1, e_2, and e_3 are the conventional strains after the elastic strain has been deducted.

† All stress values are true stress, defined as load divided by actual area.

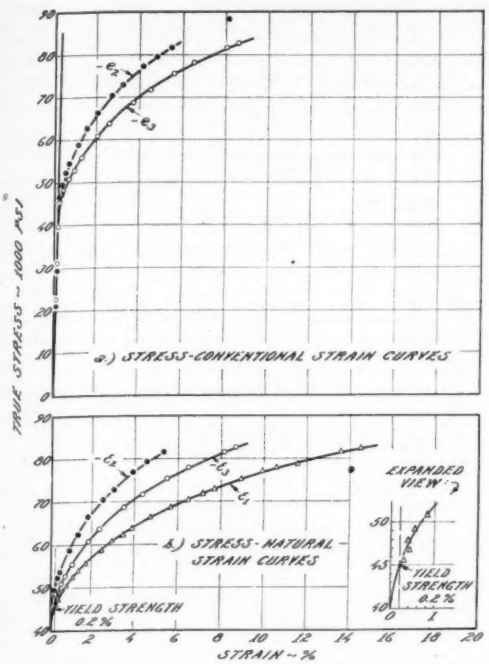

FIG. 3: REPRESENTATIVE STRESS-STRAIN CURVES IN TENSION FOR 1½ INCH 24ST ALUMINUM PLATE.

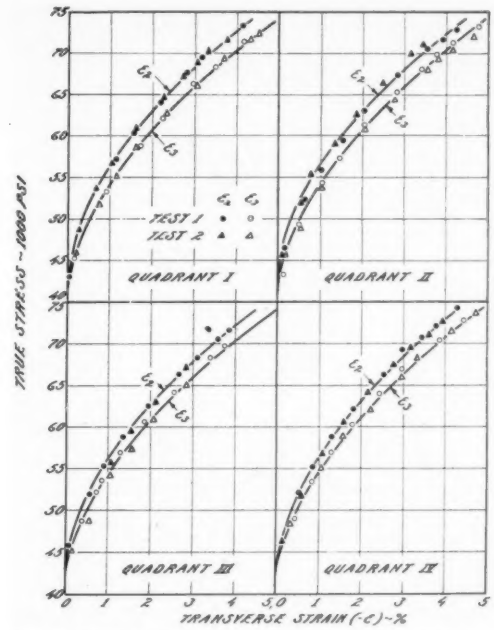

FIG. 4: STRESS-TRANSVERSE STRAIN CURVES IN TENSION FOR THE SAME ORIENTATION IN THE FOUR QUADRANTS OF A 1½ INCH 24ST ALUMINUM PLATE.

shown in Fig. 3a. The elastic strains were taken out, and the stress-strain curves were redrawn with stress as a function of the two natural strains, ϵ_2 and ϵ_3 (Fig. 3b). A stress-strain curve of stress versus ϵ_1 was then constructed from which the yield strength (0.2 per cent plastic strain) was determined, as shown in Fig. 3b.

A special series of tests was made to check the general symmetry of the plate—namely, that the anisotropy in each quadrant of the system of coordinates formed by the rolling direction, the transverse direction, and the normal direction was the same. Only four quadrants needed to be checked, since the test sections were all taken from the center plane of the plate. These tests were made on specimens located in the four possible *C* planes at an angle of 45° to the rolling plane.

It can be seen from the stress-strain curves in Fig. 4 that the belief in the general symmetry of the plate was valid. The values of each property measured were equal for all four quadrants, within the limits of accuracy and scatter. Therefore, only one quadrant, as represented in Fig. 2, need be considered.

Fig. 4 also shows that the degree of scatter encountered, resulting from nonuniformity of the aluminum plate, was small.

Results and Discussion

Yield Strength

The plate was found to exhibit a definite degree of anisotropy, which seems to be typical of aluminum-alloy plate. However, all yield strength (0.2 per cent plastic strain) values, Fig. 5, were found to be within ±5000 lbs. per sq.in. of an average value. The ob-

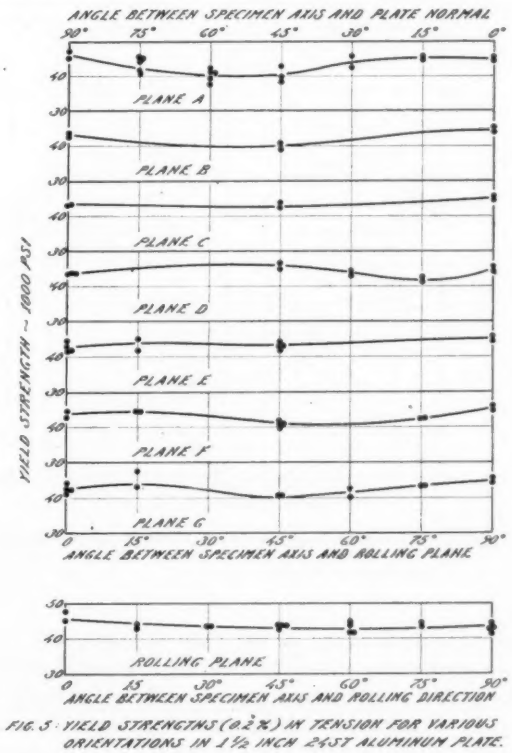

FIG. 5: YIELD STRENGTHS (0.2 %) IN TENSION FOR VARIOUS ORIENTATIONS IN 1½ INCH 24ST ALUMINUM PLATE.

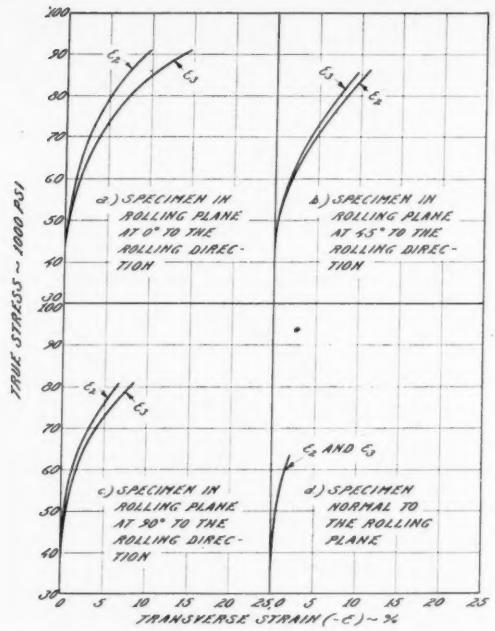
TRUE STRESS ~ 1000 PSI
TRANSVERSE STRAIN (-ε) ~ %
a) SPECIMEN IN ROLLING PLANE AT 0° TO THE ROLLING DIRECTION
b) SPECIMEN IN ROLLING PLANE AT 45° TO THE ROLLING DIRECTION
c) SPECIMEN IN ROLLING PLANE AT 90° TO THE ROLLING DIRECTION
d) SPECIMEN NORMAL TO THE ROLLING PLANE
ε2 AND ε3

FIG. 6: STRESS-TRANSVERSE STRAIN CURVES IN TENSION FOR VARIOUS ORIENTATIONS IN 1½ INCH 24ST ALUMINUM PLATE.

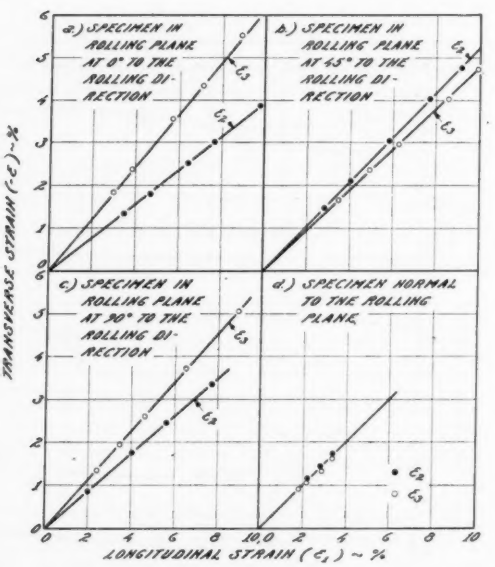
TRANSVERSE STRAIN (-ε) ~ %
LONGITUDINAL STRAIN (ε1) ~ %
a) SPECIMEN IN ROLLING PLANE AT 0° TO THE ROLLING DIRECTION
b) SPECIMEN IN ROLLING PLANE AT 45° TO THE ROLLING DIRECTION
c) SPECIMEN IN ROLLING PLANE AT 90° TO THE ROLLING DIRECTION
d) SPECIMEN NORMAL TO THE ROLLING PLANE

FIG. 7: TRANSVERSE STRAINS VS. LONGITUDINAL STRAIN FOR VARIOUS ORIENTATIONS IN 1½ INCH 24ST ALUMINUM PLATE.

served directionality in the yield strength was therefore small, since the scattering due to nonuniformity of the plate amounted to approximately ±2,000 lbs. per sq.in. Considering this uncertainty, the yield strength values in the rolling plane exhibited a directionality similar to that observed in previous investigations for severely cold-rolled and subsequently annealed, pure aluminum sheet.[4]

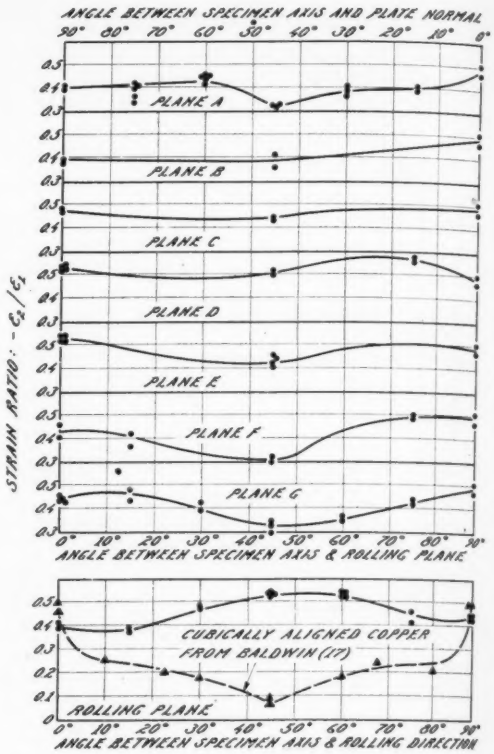

FIG. 8: STRAIN RATIO FOR VARIOUS ORIENTATIONS IN 1½ INCH 24ST ALUMINUM PLATE.

Strain Ratios

The strains differed considerably from those required for an isotropic metal—namely, that for any orientation:

$$\epsilon_2 = \epsilon_3 = -\epsilon_1/2$$

Curves of stress versus the two transverse strains, ϵ_2 and ϵ_3, are shown in Fig. 6 for specimens in the rolling plane at angles of 0°, 45°, and 90° to the rolling direction and for a specimen in the normal direction. These curves show the degree of anisotropy for the principal directions in the plate. They also serve to illustrate the different types of behavior encountered. The transverse strain, ϵ_3, was the larger transverse strain for most of the specimens tested. The longitudinal and transverse specimens, Figs. 6a and 6c, followed this pattern. The maximum transverse strain for some of the specimens was the strain ϵ_2 as illustrated in Fig. 6b for a specimen in the rolling plane midway between the longitudinal and transverse directions. A few specimens exhibited almost isotropic behavior in that the two transverse strains were practically equal, as shown for the normal specimen in Fig. 6d.

In Fig. 7, the data for the same curves are replotted, showing ϵ_2 and ϵ_3 as functions of ϵ_1. It can be seen from the last graphs that the points generally fall on a straight line. This means that, for the strains encoun-

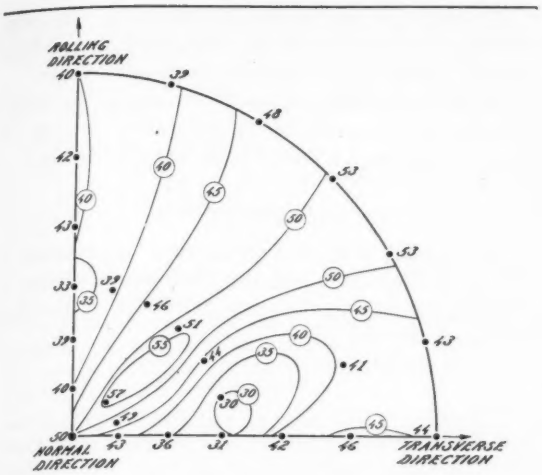

FIG. 9: STEREOGRAPHIC PROJECTION SHOWING THE PLASTIC ANISOTROPY ($-\epsilon_2/\epsilon_1 \times 100$) FOR VARIOUS ORIENTATIONS IN 1½ INCH 24ST ALUMINUM PLATE.

tered in the tensile test, the anisotropy remained practically constant for the duration of the test—i.e., independent of ϵ_1.

Taking the ratio ϵ_2/ϵ_1 as a measure of the anisotropy, the observed values are represented in Fig. 8, and again in Fig. 9, as one quadrant of a stereographic projection.

The latter representation shows that the values ϵ_2/ϵ_1 do not conform to a high degree of symmetry or to any relation that could be expressed by a simple algebraic formula. Such a condition is generally encountered in the plastic flow of single crystals. Consequently, it must be assumed that the texture of the plate possessed some preferred orientation. Thus, the structure of a plate may be considered as consisting of a mixture of crystals, a part of which was randomly oriented with the remainder more or less accurately aligned in certain preferred orientations.

The existence of preferred orientation was verified by an x-ray diffraction pattern taken in the normal direction at the center of the thickness of the plate. The material used for the x-ray pattern was reheat-treated in the same manner as the tensile specimens. This diffraction pattern, Fig. 10, shows preferred orientation comparable to that shown by aluminum that has been subjected to a considerable degree of cold work.[4]

It is impossible at present to predict the plastic behavior of a mixture of randomly oriented crystals and aligned crystals. Even a comparatively simple structure consisting of a symmetrical arrangement of a few crystals has not been analyzed in this respect to date. Some light is thrown on this problem by previous investigations. The largest degree of anisotropy is that exhibited by single crystals.[14,15] However, even for single crystals, experimentally determined strain ratios did not conform to calculated values based upon a single slip mechanism, as illustrated in Fig. 11. From

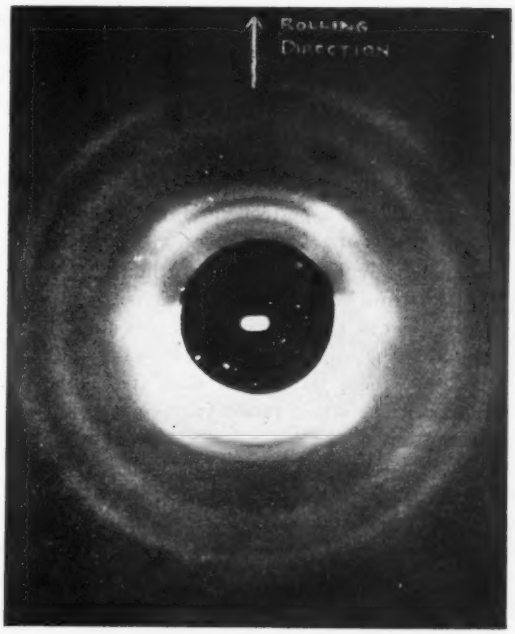

FIG. 10. X-ray diffraction pattern taken in normal direction at center of 1½-in. 24ST aluminum plate (integrating diffraction camera, Mo. radiation, 2.93 cm. sample to film distance).

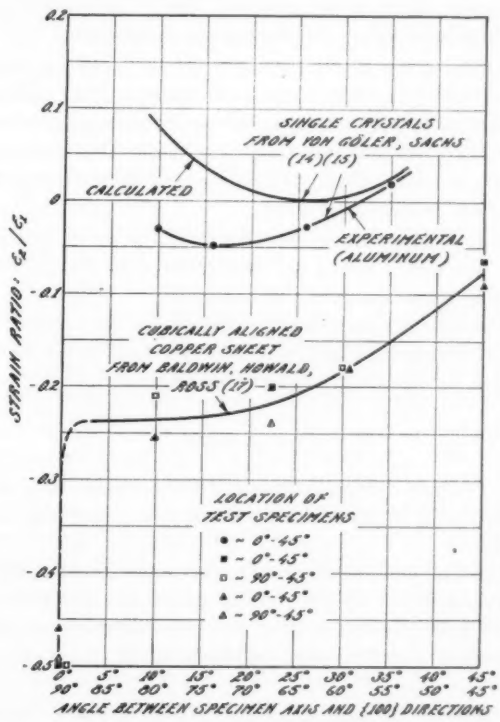
STRAIN RATIO: ϵ_2/ϵ_1
SINGLE CRYSTALS FROM VON GÖLER, SACHS (14)(15)
CALCULATED
EXPERIMENTAL (ALUMINUM)
CUBICALLY ALIGNED COPPER SHEET FROM BALDWIN, HOWALD, ROSS (17)
LOCATION OF TEST SPECIMENS
● ~ 0°-45°
■ ~ 0°-45°
□ ~ 90°-45°
▲ ~ 0°-45°
△ ~ 90°-45°
ANGLE BETWEEN SPECIMEN AXIS AND {100} DIRECTIONS

FIG. 11: STRAIN RATIO IN TENSION FOR VARIOUS ORIENTATIONS IN FACE CENTERED CUBIC METALS.

this data, it is evident that a small amount of imperfection in the crystal lattice will considerably alter the strain ratios.

Furthermore, the structure of annealed sheet of some face centered cubic metals approximates the crystallographic structure of a single crystal.[4,16,17] Such sheet is composed of crystals that are aligned with their cubic axes nearly parallel to the rolling, transverse, and normal directions of the sheet. Some authors claim that close to 100 per cent cubic alignment (i.e., the sheet being almost a perfect crystal) can be obtained by suitable processing.

The anisotropy in plastic flow exhibited by specimens taken from such sheet in various directions (in the plane of the sheet) has been measured by von Goeler and Sachs[4] and by Baldwin, Howald, and Ross.[17] As expected, these data show that (particularly for small strains) the strain ratios vary considerably with the orientation of the test specimen as shown in Fig. 11.* It can be further seen from Fig. 11 that, even though the sheet was presumably 100 per cent aligned, there is a marked difference in the strain ratios from those for single crystals of the same orientation. This deviation of the sheet specimens from the theoretical behavior of crystals is in the same direction but in a larger degree than the deviation shown between theoretical and actual crystals. This may be explained by the fact that specimens cut from an aligned sheet conform to symmetry more accurately than do specimens cut from single crystals; hence, more slip systems become operative during the deformation.

In Fig. 8 the strain ratios for copper sheet are compared with the strain ratios for specimens in various directions in the rolling plane of the aluminum plate. As to be expected from the X-ray study, this plate evidently does not display the same type of preferred orientation as the copper sheet.

It is obvious, therefore, that both the yield strength and the strain ratios are correlated with the crystallographic anisotropy of the material.

This investigation was conducted on only one lot of 24ST aluminum plate, so that variations might be expected for other lots and for other alloys.

Conclusions

(1) X-ray diffraction showed the presence of a definite degree of preferred orientation in aluminum-alloy plate.

(2) The yield strength values possessed only a slight directionality. In the rolling plane the variation of yield strength was similar to that exhibited by cold-rolled and annealed pure aluminum sheet.

(3) Ratios of the transverse strains to the longitudinal strains showed a marked degree of directionality similar in type to that exhibited by single crystals.

(4) It is impossible, at present, to predict the plastic behavior of a material (variations in yield strength and strain ratios) from a known preferred orientation.

Acknowledgments

The authors wish to express their appreciation to Dr. K. R. Van Horn and the Aluminum Company of America for making the x-ray diffraction pattern that appears in the text.

References

[1] Klingler, L. J., and Sachs, G., *Dependence of the Stress-Strain Curves of Cold-Worked Metals Upon the Testing Direction*, Journal of the Aeronautical Sciences, Vol. 15, No. 3, pp. 151–154, March, 1948.

[2] Phillips, A., and Dunkle, H. H., *Directional Properties in Rolled and Annealed Low Carbon Steel*, Trans. Am. Soc. Metals, Vol. 23, pp. 398–408, 1938.

[3] Mehringer, F. J., and MacGregor, C. W., *Effects of Cold Rolling on the True Stress-Strain Properties of a Low Carbon Steel*, Trans. Am. Inst. Mining Met. Engrs., Vol. 162, pp. 291–309, 1945.

[4] von Goeler, and Sachs, G., *Rolling and Recrystallization Textures of Regular Face Centered Metals*, Z. Physik, Vol. 41, pp. 873–888, 1927; Vol. 56, pp. 477–502, 1929.

[5] Goss, N. P., *Hot Working, Cold Working and Recrystallization Structure*, Trans. Am. Soc. Metals, Vol. 24, pp. 967–1036, 1936.

[6] Gensamer, M., and Vukmanic, P. A., *Preferred Orientations in Hot Rolled Low Carbon Steel*, Trans. Am. Inst. Mining Met. Engrs., Vol. 125, pp. 507–515, 1937.

[7] Goss, N. P., *Structural Changes in Low Carbon Steels Produced by Hot and Cold Rolling*, Trans. Am. Soc. Metals, Vol. 29, pp. 20–34, 1941.

[8] Lode, W., *Tests on the Effect of the Medium Principal Stress on the Flow of the Metals Iron, Copper, and Nickel*, Z. Physik, Vol. 36, pp. 913–939, 1926.

[9] Taylor, G. I., and Quinney, H., *The Plastic Distortion of Metals*, Phil. Trans. Roy. Soc., London, Vol. 230, pp. 329–362, 1931.

[10] Dorn, J. E., *Stress-Strain Relations for the Plastic Deformation of Anisotropic Metals*, ONR, Third Progress Report, N6-ori-111, Task IV, 1947.

[11] Avery, C. H., Tietz, T. E., and Dorn, J. E., *Investigations on the Validity of an Idealized Theory of Plastic Flow for Rolled Mild Steels*, ONR, Fourth Technical Report, N6-ori-111, Task IV, 1947.

[12] Schmid, E., and Boas, W., *Plasticity of Crystals*, Julius Springer, Berlin, 1935.

[13] Sachs, G., *The Physical Properties of Aluminum Crystals*, Z. Ver. deut. Ing., Vol. 71, pp. 577–584, 1927.

[14] Karnop, R., and Sachs, G., *Behavior of Aluminum Crystals Under Tension II, Experimental*, Z. Physik, Vol. 41, pp. 116–139, 1927.

[15] von Goeler, and Sachs, G., *Behavior of Aluminum Crystals Under Tension I, Geometrical Principles*, Z. Physik, Vol. 41, pp. 103–115, 1927.

[16] Koester, W., *Regular Development of Structure in Copper After Recrystallization*, Z. Metallkunde, Vol. 18, pp. 112–116, 1926.

[17] Baldwin, W. M., Howald, T. S., and Ross, A. W., *Relative Triaxial Deformation Rates*, Trans. Am. Inst. Mining Met. Engrs. Vol. 166, pp. 86–109, 1946.

* However, for large strains all orientations show a tendency to approach a strain ratio $\epsilon_2/\epsilon_1 = -0.5$. This indicates that for small strains the sheet acted as a single crystal, operating under single slip or double slip mechanism, but when a certain strain was reached, different for each orientation, multiple slip began to take place.

Full-Scale Free-Flight Ballistic Measurements of Guided Missiles

L. A. DELSASSO,* L. G. DE BEY,† AND D. REUYL‡

Ballistic Research Laboratories, Aberdeen Proving Ground

SUMMARY

Special problems arising in the instrumentation of full-scale free-flight tests are considered, particularly as pertaining to guided missiles. Applications of specialized optical and electronic equipment are reviewed in detail.

Under optical instrumentation such problems as the modification and application of acceleration cameras, photo-theodolites, and precision-plate cameras are discussed. In addition, the development of tracking telescopes using refractors and reflectors of large effective focal length in conjunction with special mounts for studying the behavior of missiles during the entire flight is considered; results obtained so far from these instruments are included. Brief reference is made to the methods for determining ballistic data, by means of high-speed motion-picture cameras, for aircraft rockets launched from airplanes.

Under electronic instrumentation, the use of radar for trajectory determinations and the modifications necessary on standard radar equipment for use in long-range guided missiles are discussed. The use of radio-doppler and the application to this field are considered in detail, and the problems and advantages encountered in this field are presented. The usefulness of microwave reflection doppler equipment is also reviewed. Finally, a comparison of the results obtained by the various systems of instrumentation is made.

OPTICAL METHODS

General

THE PROBLEMS to be solved in the measurement of guided missiles by optical methods are similar to those encountered in the fields of astrometry and planetary photography.

The determination of the trajectory of the missile can be conveniently made by instruments of moderate size. However, for the measurement of missile attitude and the observation of special phenomena, large instruments are needed. This need has led to the development of powerful instruments, similar to astronomical telescopes but differing in the design of mounts, drive mechanisms, and auxiliary instrumentation.

In general, the instruments used at White Sands Proving Ground do not represent the ideal instrumentation for the measurement problems to which they are applied. The urgency of the need for data has often been the determining factor in deciding upon the modification of existing methods and available instruments rather than the design of new ones. For obvious reasons the principle of overdetermination is applied for each set of instruments wherever possible.

Received April 28, 1948. This is a condensed version of a paper presented at the Annual Summer Meeting, I.A.S., Los Angeles, August 7–8, 1947.

* Chief, Ballistic Measurements Laboratory.

† Chief, Electronic Measurements Branch, Ballistic Measurements Laboratory.

‡ Chief, Optical Measurements Branch, Ballistic Measurements Laboratory.

Trajectory Measurements

For the measurement of position of the missile, as a function of time, the following types of instruments of moderate focal length were available at the start of the A-4 experiments:

(a) Acceleration or Bowen-Knapp cameras, fixed, of high-speed, ribbon frame, motion-picture type.

(b) Photo-theodolites, tracking, American-made Mitchell and Akeley types.

(c) Cine-theodolites, tracking, German-made Askania type.

(d) Ballistic cameras, fixed, of single plate, multiple exposure type.

The fixed cameras will, in general, yield results of greater accuracy than can be obtained with tracking instruments. However, the observable portion of the trajectory is limited for a given setup.

The photo-theodolite is therefore the preferred optical instrument for the measurement of trajectories of long ranges and high altitudes.

The Bowen-Knapp camera has been used extensively for trajectory measurements of rockets and is generally useful for problems that require observations at a high rate and over a considerable width of field. At White Sands two Bowen-Knapp camera systems of three stations each are used. For each launching site the stations are located approximately 1 mile to the South, East, and West, respectively.

A photograph of the camera is given in Fig. 1, showing means for adjustment in azimuth and elevation. The frame measures $5^1/_4$ in. in width, the height being variable in stages between 0.9 and 0.15 in. Corresponding exposure rates are 30 and 180 frames per sec., respectively, the lowest rate being used in most cases. The frame may be rotated in its own plane by means of the cradle mounting to have its long dimension roughly parallel to the projected path of the missile.

The camera may be equipped with a 7- or a 12-in. lens and is operated at a fixed exposure time of 0.0001 sec.

The timing equipment used with the camera consists of a disc rotating at a rate of 10 r.p.s. by means of an

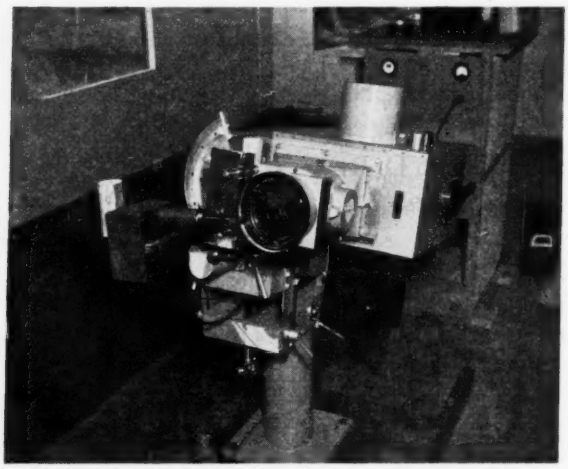

FIG. 1. Bowen-Knapp camera equipped with timing device, mounted in M-14 trailer.

1,800 r.p.m. synchronous motor operated at a crystal-controlled 60-cycle frequency. A portion of the circumference of the disc is photographed through the camera objective by means of an auxiliary optical system.

The present synchronization of the instruments of a set is achieved through the recording of a photoflash lamp, operated by the firing signal pulse by means of a thyratron circuit. Hence, the accuracy of synchronization is determined by the frame speed and amounts to $\pm 1/60$ sec.

Since the portion of the trajectory (the first 4,000 ft.) measured by the Bowen-Knapp system cannot be assumed to lie in a plane, the triangulation is carried out for individual points by reducing the measured film coordinates to azimuth and elevation angles. Measurements are made with a Mann comparator, specially built for this purpose, or with a Zeiss tool-maker's microscope. The probable error of an angular measurement is ± 0.1 mil under average conditions.

FIG. 2. Mitchell photo-theodolite.

The first tracking instruments at White Sands were of the Mitchell type (Fig. 2) and are located 6 miles South and West of the launching site, respectively.

The main features of this instrument are a focal length of 12 in., tracking by a single observer, and a maximum frame rate of 24 exposures per sec. The direction of the optical axis is recorded on each frame by means of dial counters operated through gear trains. Although possible backlash in the counterdrive gears causes this method to be undesirable, a change was deemed impractical under the circumstances.

The instrument has been modified by installing a $17\frac{1}{2}°$ shutter. By means of a slit in the shutter and a lamp and phototube arrangement, a pulse is generated at the instant of exposure and recorded on a Brush chronograph, together with signals of 1 and 32 pulses per sec. The firing signal is recorded on the chronograph tape also and, in addition, on the film in the same manner as for the Bowen-Knapp camera.

The measurements of the azimuth and elevation corrections are carried out by a projection method.[1] The space coordinates of the missile are calculated in the conventional manner. Calculated velocities are the average velocities for the small time intervals between measured frames. A detailed description is given in a separate report.[2] The internal consistency of the film measurements was found to be of the order of 0.2 mils.[3] When taken over time intervals of one sec., velocities may be determined with a probable error of about 1 per cent. The comparison of acceleration measurements made optically and from telemetered missile accelerometer data indicates excellent agreement between the two methods.[4]

The Askania cine-theodolite (Fig. 3) is superior to the American instruments because of the method of photographing directly the azimuth and elevation circles, thereby eliminating errors of the type caused by gear backlash in the other instruments. Additional features are the larger focal length lenses and a somewhat larger film frame. When operated in a set, all instrument shutters are synchronized by pulses received from a central station. However, a number of undesirable features are present—e.g., the inconsistent operation of the shutter, the intricate camera mechanism, and others.

At the present time one set of Askania instruments is operated at stations 7 miles NW, 7 miles NE, and 3 miles S from the launching position, respectively. Two of the instruments are equipped with 60-cm. lenses while the third has a Cassegrain reflector of 100-cm. focal length. A second set of 60-cm. instruments is operated at stations 9 miles NNW, 12 miles NE, and 3 miles S from the launching site. Either a 1, 2, or 4 pulse per sec. signal may be transmitted to the various stations for the tripping of the shutters. The shutter operation is again recorded in the same manner as was

described for the Mitchell photo-theodolite system. A timing accuracy of 0.001 sec. is obtained by this method. In addition, two instruments are set up for special purposes, such as the study of wind velocity and direction at high altitudes from vapor or smoke trails produced by the missile. Simultaneous recording will, in general, be difficult when the angle subtended by the trails exceeds the angular field of view. The use of wide field cameras is therefore recommended for this type of study.

The Askania instrumentation has been used to obtain rapid trajectory data of adequate, though possibly not maximum, accuracy. The methods of measurement and reduction are similar to those used for the Mitchell photo-theodolite records.[5]

In general, the Mitchell instrumentation will cover the trajectory of the A-4 through the point of burnout—i.e., to an altitude of about 30 miles. The Askania system will yield data generally to 40 or 50 miles. In many cases a single instrument may track and record to points considerably beyond these limits. The remaining portion of the trajectory may be determined by calculation, taking into account the variation of gravity and the rotation of the earth.[6]

The ballistic camera was developed at the Ballistic Research Laboratories for the study of bomb ballistics and is capable of giving data of high accuracy. The method is useful for other purposes also, provided that the light source is of sufficient intensity to register on a background that is necessarily dense because of multiple exposure.

In its original form the method called for two instruments mounted vertically at the end points of a measured base line.[7] The calibration of the instruments is carried out by means of stellar positions. Observations of the ballistic program are made by means of a system of shutters operated synchronously within the set of instruments and with the light source—e.g., a high intensity flashing light in the aircraft. Night programs are obviously more desirable, since the observations and the calibration may be carried out under almost identical conditions, and the shutter system can be omitted.

Further work on the development of this method has included the design of new cameras having larger plates (8 by 10 in.) and the modification of methods of measurement and reduction.

Initial experiments with a tilted camera method[8] are in progress at White Sands thereby also examining the possible use of this method for the study of long-range missiles.

At the present time two stations (Fig. 4) have been erected at White Sands at positions 3 miles East and West of the launching site. The cameras may be operated at rates of 1, 2, or 4 exposures per sec. Preliminary results indicate that the method may be useful by photographing the jet and the light emitted by the hot jet rudders. Also, suitable photographs have been made of vapor trails. It has been difficult up to now to obtain satisfactory images of the missile itself.

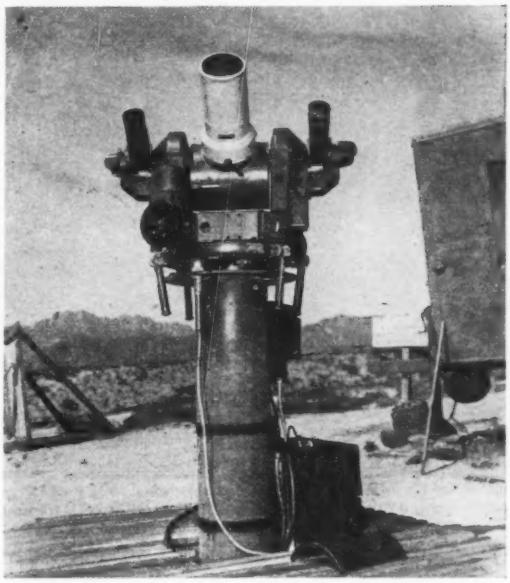

FIG. 3. Askania cine-theodolite.

A statement of the accuracy obtainable by the tilted method would be somewhat premature, in view of the early stage of present experiments. However, it may be of interest to mention the accuracy of the determination of lens distortion, using star positions for the purpose of calibration. It was found that the dispersion was given by an average residual of 2 or 3 sec. of arc. Allowing for the effect of other errors of measurement it may be possible to achieve an angular accuracy given by a probable error of ± 0.02 mil. Obviously, this

FIG. 4. Ballistic camera in tilted position, with shutter assembly and sky screen.

FIG. 5. Twin 4.5-in. tracking telescope on modified M-45 mount, showing recording and tracking instruments.

value will depend largely upon the accuracy with which the image of the missile, or of the jet, may be measured.

Attitude Measurements

A study of the attitude of the missile as a function of time may be undertaken in a number of different ways. The method described here involves the use of ground instrumentation exclusively, thereby avoiding problems encountered in the telemetering of data measured in the missile or the recovery of instruments carried by the missile.

For the study of roll, the only requirement is the securing of a clear record of suitable markings on the missile. However, for the determination of yaw and pitch it is evident that as a first approximation the accuracy of measurement will be directly proportional to the focal length. It is readily seen that the increase of focal length will call for a corresponding increase in objective diameter, thus causing new problems of engineering and operation. Furthermore, the image disturbances caused by the atmosphere tend to become so large that ultimately further increase in focal length would not yield any higher accuracy of measurement.

At the present time there are two instruments of different experimental type in operation at White Sands. The first instrument was designed around available optics and mounts. The second instrument was similarly designed for an existing mount for the purpose of testing a different optical system.

Because of the limitations of this equipment it has been difficult to obtain complete records from both stations. However, for a number of rounds, aerodynamic data during descent were obtained by one instrument in addition to measurements of the initial portion of the flight. The latter are used to check the functioning of the missile controls during burning and to determine the missile oscillations in free, near vacuum flight beyond the point of fuel cut off.

The major problem encountered in the design of a tracking telescope is caused by the combination of requirements of large focal length and accurate tracking.

The first telescope that was constructed consisted of a 4.5-in. refracting telescope, mounted on an M-45, 50-cal. gun turret.[9] In order to obtain a scale corresponding to large focal length, the telescope was equipped with an amplifying lens that served to convert the 60-in. focal length to an effective focal length of 200 in. This photographic refractor was equipped with a 35-mm. recording Eyemo motion-picture camera operated at a rate of about 15 exposures per sec. A pair of 20-power binoculars was used for tracking and a visual 4-in. telescope of 48-in. focal length was installed to be used for visual observations. The latter instrument has since been converted into a second photographic telescope, also with amplifying lens to give an effective focal length of 150 in.

The instrument was not intended for the measurement of position, and its counters give approximate values only of azimuth and elevation. Reliance is placed upon a time record used to tie in with other instrumentation for the determination of the position of the rocket at the time of each photograph. The timing is obtained by means of 60 and 1 per sec. neon lamp pips recorded on the edge of the film.

The instrument (Fig. 5) is located 8 miles SW of the launching site. In spite of the small field size it was found possible to track missiles of the A-4 type satisfactorily. A vital factor in obtaining good images of the missile is that of having proper lighting conditions; hence, for a given set of stations the time of firing is of the utmost importance. In view of the difficulty of adhering to a time schedule in experimental launchings, it is necessary to operate more than the minimum number of two stations to ensure a fair probability of good records.

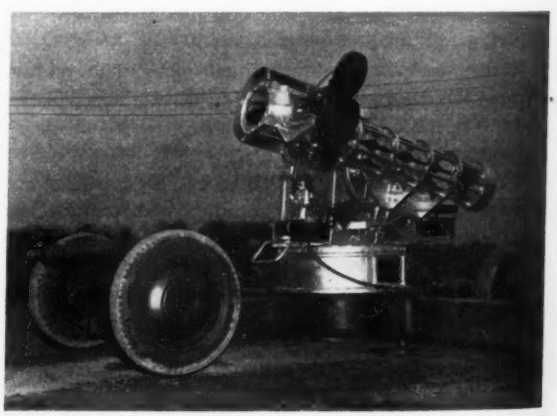

FIG. 6. Ten-in. telescope on modified M-45 mount showing mirror and recording camera.

When the construction of the second instrument was undertaken, the need for greater light-gathering power was satisfied by a parabolic mirror of 10-in. diameter. Used as a Newtonian Telescope, this mirror has a focal length of 80 in., but again an amplifying system was added to obtain an effective focal length of 280 in. A 35-mm. Akeley motion-picture camera was installed as the recording instrument. Photographed on the image frame directly are azimuth and elevation dials, as well as a time dial. The former are driven by selsyn motors; the latter, by a synchronous motor operated at a crystal-controlled frequency.

The telescope is mounted on an M-45, 50-cal. gun turret, on a 40-mm. gun carriage (Fig. 6), and located 7 miles NW of the launching site.

A sample record is given in Fig. 7. Measurements of tracking telescope records have been made for a number of rounds. In most cases these records have been made from individual stations; they therefore consist of the measurement of the projection of the missile axis on the plane of the photograph. However, adequate synchronization of the two telescopes has been accomplished recently, and calculations are in progress to determine the directions of the axis of the missile in space from the two sets of measurements.

A preliminary analysis of the results indicates that the axis of the A-4 image on the 4.5-in. records may be measured with a probable error of $\pm 0.7°$ when the missile is at a height of approximately 25 miles.

Film measurements have been made by means of a measuring microscope equipped with a rotating reticle or on the projected image.[1]

Special Measurements

The usefulness of a long focus instrument is enhanced by its application to special types of measurements. These include the ejection of apparatus, the separation of rockets in a stage system, the functioning of steering rockets, and a number of similar occurrences. Furthermore, it would be possible to record light signals emitted from the missile as a method of optical telemetering.

Successful records have been obtained of the tracking of apparatus ejected from the missile and brought down by parachute. War-head blowoffs, as well as evidence of functional failures, have been recorded.

Photographs showing detailed jet structure are being studied in conjunction with the analysis of the functioning of the missile motor. Spectrographic work on the jet has been initiated.

Future Work

The need for further research on optical methods of measurement and development of instrumentation is clearly indicated.

Improved synchronization will be achieved by the installation of pip timing on the Bowen-Knapp cameras and the synchronized operation of the Mitchell photo-theodolite shutters, both in progress.

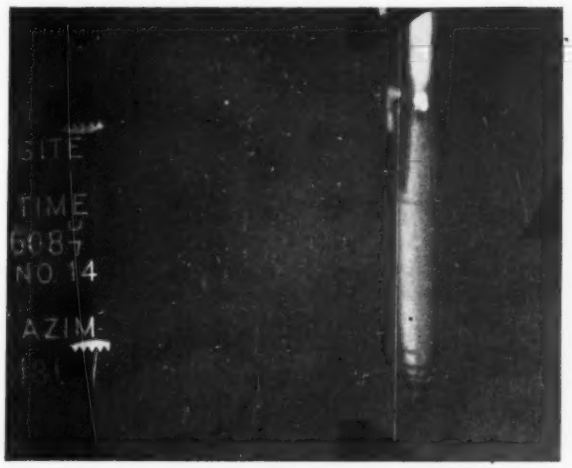

FIG. 7. Ten-in. tracking telescope record of A-4 missile made from Station N at a slant distance of approximately 8 miles, showing entire 35-mm. frame with dial readings of azimuth elevation and time counters.

The data recording system of the Askania cine-theodolites is being modified by the installation of Edgerton lamps for illumination of the circles. A project to equip a number of these instruments with an optical system of large focal length is in the design stage.

The study of design specifications for a precision photo-theodolite capable of yielding measurements of missiles at distances of 100 miles and more is being undertaken by the Panel on Test Range Procedures and Instrumentation.

Additional work is carried on to improve shutter synchronization of the ballistic camera system. Regarding further research on long focus instrumentation and methods of tracking, the construction of a 16-in. telescope on a 90-mm. antiaircraft gun mount has been completed. This instrument is of Newtonian type and will be provided with a means to vary the effective focal length between limits of 400 and 1,000 in. Projects including the design of a tracking telescope of Cassegrain type mounted on a SCR-547 radar set pedestal are in the planning stage. A number of additional problems have come up in connection with this work. They include the development of a beam distributing device to permit a single telescope to serve as a multiple-purpose recording instrument and the design of precision circles to make the instrument more nearly self sufficient. Future problems in conjunction with still longer ranges will require the development of methods of automatic positioning of the instruments operated in chain systems.

With regard to tracking problems, an investigation of methods of tracking may lead to the design of special optical systems.

Of fundamental importance in all projects involving photographic recording is the improvement of recording

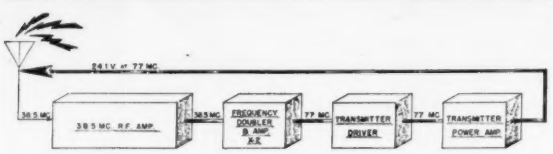

FIG. 8. Block diagram of transceiver.

techniques. As a part of a larger project an experimental study of photographic emulsions and light filters has been initiated through the courtesy and with the cooperation of the Eastman Kodak Company.

Plans for further research on spectrographic methods are being formulated on the basis of successful preliminary experiments.

ELECTRONIC METHODS

Radar Instrumentation

In the early part of the war it was discovered that many types of radar, and in particular such types as SCR-584, were capable of tracking projectiles in flight. A great deal of work was done in this field at Aberdeen to apply radar to ballistic measurements. When the first guided missile testing was undertaken, it was natural to extend this work to those tests. As the missiles under test increased in range, it soon became evident that it was no longer possible to track the missiles throughout their full flight by ordinary reflection radar. The solution of this difficulty was thought to be the use of beacons that had already been developed for a similar use in the case of aircraft. At this time the Ordnance Department requested the Signal Corps, through the Evans Signal Laboratory, to undertake this phase of the instrumentation because of the Corps' wide experience with both the ground equipment and the beacons. Since that time the Signal Corps has been handling this phase of the instrumentation problem at White Sands Proving Ground and has been successful in tracking the A-4 missiles throughout their entire flight.

It is expected that the Evans Signal Laboratory will report on this phase of the work in the near future and only a brief outline will be given here.

The equipment at the present time installed at White Sands consists of two modified SCR-584's with extended range and installed plotting boards. As an aid to tracking, especially during the early parts of the flight, two M-2 optical trackers have been installed in such a way as to permit them to position the radars on the missile during flight.

The plotting boards give an instantaneous plot of the path of the missile with moderate accuracy and will be particularly useful to follow the flight of missiles that are controlled from the ground.

In addition, the range, azimuth, and elevation angle information from each of the radars is recorded photographically on motion picture film which can be analyzed later. The information gained from the photographic records is sufficient to give satisfactory trajectory plots but, in general, is not accurate enough to give satisfactory first and second differences.

A DOPPLER SYSTEM FOR THE DETERMINATION OF VELOCITIES AND POSITIONS OF GUIDED MISSILES

General Description

The beacon doppler system in the most general form involves transmitting a radio frequency wave from the ground to the missile receiving and amplifying this signal, and transmitting back to the ground a second signal that bears a constant phase relationship to the signal received at the missile. Heterodyning of the transmitted and received signals yields the magnitude of the radio frequency doppler effect. In this system, instead of depending upon energy reflected from the missile body, as is the case when using any of the so-called reflection doppler systems, a signal of many times greater amplitude is radiated by a beacon in the missile, thus greatly extending the range of the system.

To distinguish between the system to be described and other systems that may be developed or used in the future, an alphabetical name has been assigned to this instrumentation. DOVAP, derived from Doppler Velocity and Position instrumentation, will be used hereafter in referring to the particular method of applying the doppler effect to be described in this paper.

Basically, DOVAP provides for transmitting a stabilized continuous radio frequency wave from a fixed ground station to the missile, doubling the frequency of this transmitted wave in the missile receiver and transmitting the doubled frequency from the missile to three or more fixed ground receivers. Fig. 8 is a block diagram of a typical missile beacon, which functions as a receiver and transmitter in the missile. By amplifying and doubling the received reference frequency and retransmitting this signal, fixed phase relationship is obtained and the technical difficulties encountered in attempting to receive and transmit on a common frequency are eliminated.

The frequency of the missile signal as received at each ground station is heterodyned with twice the frequency of the original transmitted ground signal. This is accomplished by receiving this reference frequency on a separate receiver at each ground station and doubling the frequency by the same method used in the missile receiver. The beat or doppler frequency is produced by mixing the radio frequency output from the two receivers. Land wires are used to transmit the doppler signals to a common point for the purpose of making permanent and continuous records on 35-mm. photographic film. Fig. 9 is a block diagram of one form of ground station equipment showing the method employed to combine the reference frequency and the

retransmitted frequency from the missile to produce the doppler beat.

In Fig. 10 a typical DOVAP field setup is depicted with the various ground stations located approximately as they are at the White Sands Proving Ground range.

Each doppler frequency cycle represents a change in path length from the transmitter to the missile to the ground receiver of one-half wave length of the reference frequency. From the differences in the change of path length to three or more receivers, the spatial coordinates of the missile at any instant may be computed by solving a group of equations representing the intersection of three or more ellipsoids (spheres if the transmitter is coincident with one of the receivers).

A detailed analysis of the mathematical concepts of the data reduction methods is beyond the scope of this report. Such reports have been prepared by T-4 S. Kusaka[10] and B. Garfinkel.[11] Only the generalized method will be presented here as it applies to the overall problem of obtaining ballistic data for the missile.

The data obtained by the DOVAP system in their final recorded form consist of a long and continuous series of doppler cycle sine waves from each receiving station and a time calibration of the film record. It will be assumed that the sine wave traces are continuous from the instant the missile leaves the ground, thus establishing one point on the trajectory whose coordinates are known. Almost any other known point would serve as well, and, in practice (since the doppler traces are not always continuous from the start of the trajectory), a point some few hundred or thousand feet along the trajectory, as determined by phototheodolites, is used.

Starting at the known point, each doppler cycle represents a change in the total distance from the transmitter to the missile and from the missile to one of the ground receivers of one wave length at 77 Mc. or approximately 12.5 ft. If n is the number of doppler cycles corresponding to any point along the trajectory, then $n\lambda$ is the total change of path distance as the missile moves from the known point to the point to be determined. It is, therefore, necessary to count (from the known point) the number of doppler cycles in each channel corresponding to each desired point along the trajectory. It is most convenient to refer to the points along the trajectory in terms of the time elapsing from the start of the flight. If the value of n is determined for successive time intervals—e.g., $^1/_2$ sec.—then the points determined will give the position of the missile at $^1/_2$-sec. intervals.

It may be shown that the coordinates (x, y, z) of any point P on the trajectory may be evaluated by the solution of two linear equations and one quadratic equation of the form

$$x = az + l$$
$$y = bz + m$$
$$Az^2 + 2Bz + Cz = 0$$

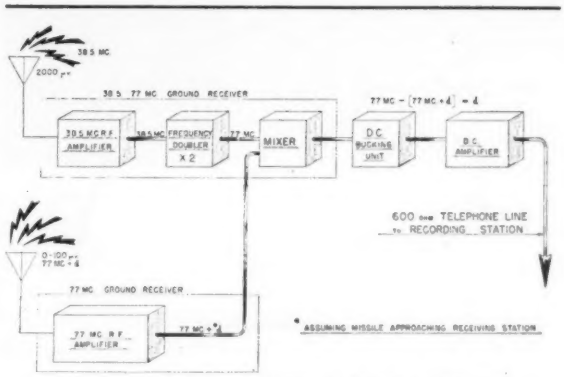

FIG. 9. Block diagram of ground station equipment.

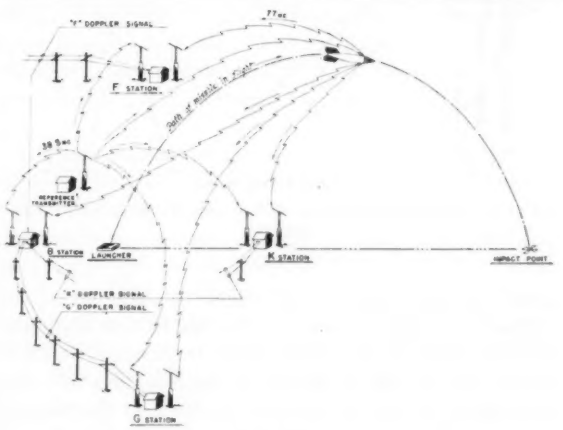

FIG. 10.

where A, B, C, a, b, l, and m are coefficients whose values may be determined from known factors involving the coordinates of the ground receiving and transmitting stations, the initial point, and the values of n obtained from the film record. The expressions for these coefficients are lengthy, and to obtain solutions for them by ordinary desk computing machines would involve weeks of computer time to arrive at the coordinates of a 100-point trajectory.

The solution has been programmed for the ENIAC electronic computing machine, and assurance has been given that an 800-point trajectory can be computed in the time of flight of the missile or approximately seven minutes. Following completion of the problem the machine may be arranged to print the coordinate data in tabular form. It will further tabulate the first and second differences between successive points from which the velocity and acceleration may be computed.

Recording Equipment

As has been previously pointed out, the DOVAP system measures radial change of distance from each of the ground stations. An examination of a typical A-4 trajectory will reveal that, in general, there are three

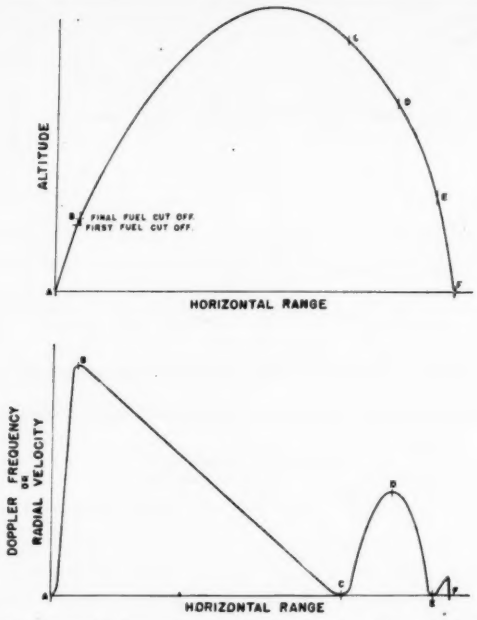

FIG. 11. Doppler frequency as a function of missile velocity and position.

points on the trajectory at which the tangent to the trajectory is perpendicular to the line from a particular ground station to the point on the trajectory. In other words, the missile is moving in such a direction that the radial change of distance is zero and the doppler frequency will also be zero.

Fig. 11 shows the approximate shape of a typical A-4 trajectory. Below the trajectory curve is plotted a curve of the doppler frequency throughout the trajectory.

The first point at which zero radial change of distance occurs is at the launching point or start of the trajectory. (For practical purposes it will be assumed that all ground receiving stations lie in the same plane and that the missile takes off in a direction perpendicular to this plane. Actually each ground receiving station may be at a different height, above or below the launching point, and accurate data reduction depends upon precise determination of the coordinates of each station.)

The missile reaches a point just beyond the peak of its trajectory before the doppler frequency again becomes zero. Between the launching point (*A*) and the point marked (*C*) on the curve the missile is moving away from all stations. From (*A*) to (*B*) the velocity of the missile and, hence, the doppler frequency are increasing rapidly because of the thrust of the burning jet. At point (*B*) the fuel is cut off, and the missile continues on its upward path with decreasing velocity until at last the force of gravity overcomes the vertical component of velocity and the peak of the trajectory is reached. The missile continues to move away from the receiving stations by virtue of the remaining horizontal component of velocity until the point (*C*) is reached. At this point the horizontal velocity and the vertical component of velocity due to the earth's gravitational field combine to give a net radial velocity of zero.

Between point (*C*) and the impact point (*F*) the velocity increases steadily, but, because of the geometric relation of the trajectory to the receiving stations, the radial velocity increases up to the point (*D*) and then decreases to zero again at the third point, marked (*E*).. Between (*E*) and (*F*) the radial velocity rises until the missile strikes at the impact point.

This somewhat detailed explanation of how the radial velocity and doppler frequency vary throughout the flight of the missile is presented here to show the need for d.c. response throughout the recording system. If the response were other than d.c., many cycles of doppler frequency would fail to record as the frequency approaches and becomes zero at each of the points discussed above. Furthermore, when the radial velocity is low and true velocity is comparatively high, each doppler cycle may represent a movement of the missile of several hundred or even several thousand feet. This is particularly true at the point (*E*) of Fig. 11. Thus the loss of a few cycles of doppler, either caused by miscounting of the final record or poor response of the recording system, may introduce large errors in the computed trajectory coordinates. After considering other parameters that affect the accuracy of the system, a permissable error of 1 cycle in 100,000 is allowed under present data reduction methods. Accordingly, the recording system has been designed to accomplish faithful reproduction of all doppler cycles present at the output of the ground receivers.

There is no known practical method of producing a so-called direct inking record of a.c. wave forms at frequencies as high as 800 or 1,000 cycles per sec. Photographic methods are more or less standard for this type of recording and were chosen because of their extreme flexibility and excellence of results.

The doppler frequency voltage from each ground station receiver is applied to the horizontal deflecting plates of a 3-inch cathode-ray tube, four of which are mounted side by side on a standard 19-inch rack panel. Conventional sweep voltages are not used during the recording process but may be applied to the vertical deflecting plates to spread the image of the doppler wave for the purpose of examination and analysis. The cathode-ray traces of the four tubes are photographed by means of a 35-mm. camera in which the film is passed behind the lens at a substantially uniform rate. The direction of motion of the image on the film is transverse to the direction of motion of the film so that the film motion supplies a time base for the recorded wave. In order that this time base may be accurately calibrated at all points along the record, a voltage of accurately known frequency derived from a time standard is caused to trip a small glow discharge

tube, mounted on the rack panel between two of the cathode-ray tubes, at 10 millisec. intervals. The recurring image on the film of this glow discharge results in a continuous row of time dots running parallel to the sine wave doppler traces and provides an accurate means of timing the events on the record with respect to the take-off or zero time. At each half-sec. interval following the start of the timing wave, a sharp pulse is superimposed on the wave to permit more rapid counting of long stretches of record. Furthermore, every twentieth such pulse is deleted to further facilitate counting. These half-sec. pulses are recorded by means of another glow discharge recording tube. (Special circuits cause the first half-sec. pulse to be transmitted from the blockhouse at the instant the A-4 lifts from the launching stand. This reference mark is considered to be zero time for all instrumentations in use at the White Sands Proving Ground.)

The doppler frequency has also been recorded on the film in the form of a small dot representing each cycle, just as the time standard signal is recorded. Experience has proved this type of recording to be less tedious from the standpoint of counting the total number of cycles in each record, especially when the counting is done by hand. With electromechanical methods of counting, the dot type of record may also be used successfully, but experience has again led to modifications so that the dots are replaced with dashes whose lengths are of approximately $^1/_2$-cycle duration. The amplified doppler signals trigger electronic switch circuits causing a glow discharge to take place in Sylvania R1130 recording tubes, one for each doppler channel. These tubes, along with the time standard dot trace tubes, are mounted on the cathode-ray tube panel in positions to cause their traces to be recorded on the film between the various sine wave traces. A representation of a typical section of a DOVAP recording is given in Fig. 12.

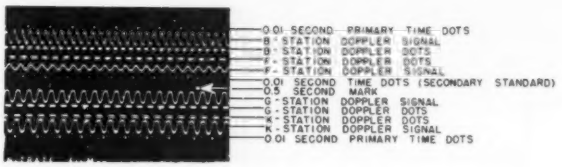
0.01 SECOND PRIMARY TIME DOTS
B - STATION DOPPLER SIGNAL
B - STATION DOPPLER DOTS
F - STATION DOPPLER DOTS
F - STATION DOPPLER SIGNAL
0.01 SECOND TIME DOTS (SECONDARY STANDARD)
0.5 SECOND MARK
G - STATION DOPPLER SIGNAL
G - STATION DOPPLER DOTS
K - STATION DOPPLER DOTS
K - STATION DOPPLER SIGNAL
0.01 SECOND PRIMARY TIME DOTS

FIG. 12. Typical section of DOVAP film record.

Description of Typical Records

Of the first 20 A-4 launchings at White Sands Proving Ground, as of the time of this writing, the DOVAP system has been used on the last 17, not having been used on rounds 1, 2, or 3. For these 17 rounds the DOVAP system has worked comparatively well, and reducible records have been obtained on all but three: An experimental telemetering transmitter in the missile blocked the doppler transmitter on round 5, the doppler signals were illegibly weak on round 7, and the missile doppler unit was not turned on because of failure of control lines to the missile on round 19.

No record has been perfect, there having been varying degrees of noise, interference, and fading in each film. Continued efforts of design and maintenance engineers have, however, consistently improved the DOVAP performance, with attendant lowering of the discontinuity of the records. Likewise, experience in reading the imperfect film records obtained to date has revealed methods of interpolation over record breaks and rough spots which make the final results closely approach the accuracy that would be obtained from a perfect film record. Figs. 13 and 14 show radial velocity and acceleration curves obtained from the DOVAP film record of A-4 round 17, which is the best record obtained to date. The mean scatter of the points is approximately 0.2 cycle per half sec. The probable error of radial velocity measurements made with these data is approximately 0.3 ft. per sec. at a velocity of 5,000 ft. per sec.

Overall accuracy of the DOVAP system in determining spatial coordinates is dependent upon many factors, not the least of which is the geometric relationship of the observing stations. There are four triplets of stations at White Sands Proving Ground (BFK, FKG, KGB, and GBF) which may be used to determine the trajectory coordinates. From analysis of the geometry of the stations it is to be expected that triplets BFK and BGK should give good agreement in the determination of the x coordinate, while triplets FKG and FBG should give good agreement for the y coordinate. All triplets should agree in the determination of the z coordinate. Below are tabular data for a particular A-4 round showing the coordinates of the trajectory near its peak as determined by each of the four triplets. Examination of these data shows that expectations are confirmed by actual measurements.

	Stations			
	BKF	BGK	FKG	FBG
x	65274	65201	66738	64504
y	−17998	−21257	−20224	−20222
z	612739	612646	612613	612753

An error in the determination of the distance u_i (transmitter to missile to receiver) for each of the stations equivalent to two doppler cycles would account for the greatest discrepancy observed above. This distance if determined from

$$u_i = C_i + n\lambda$$

where C_i is the distance from the transmitter to the launcher to the receiver, n is the number of doppler cycles, and λ is the doppler wave length. Thus, survey errors in obtaining C_i, miscounts in n, and improper assumptions as to the value of the doppler wave length may each contribute to an error in u_i. It is estimated

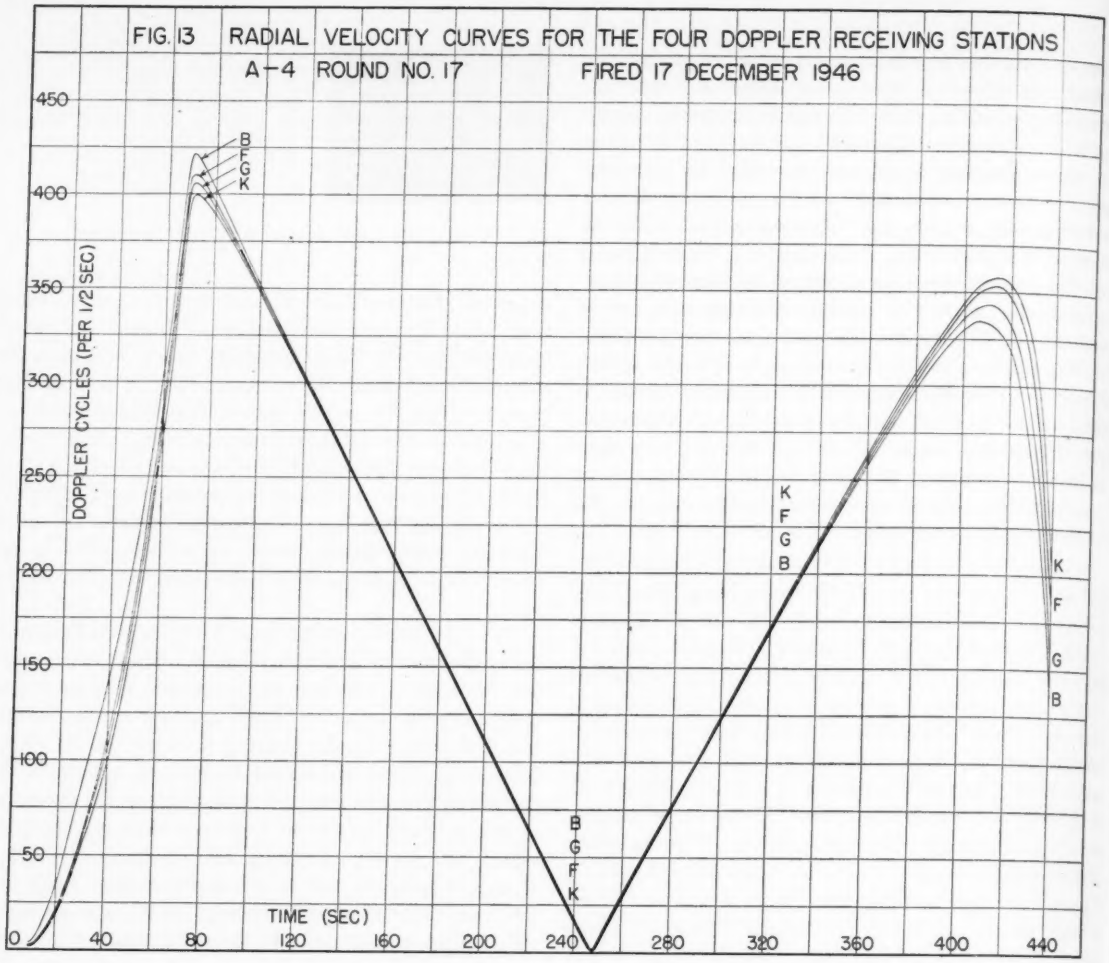
FIG. 13 RADIAL VELOCITY CURVES FOR THE FOUR DOPPLER RECEIVING STATIONS
A-4 ROUND NO. 17 FIRED 17 DECEMBER 1946
DOPPLER CYCLES (PER 1/2 SEC)
TIME (SEC)
B
G
F
K

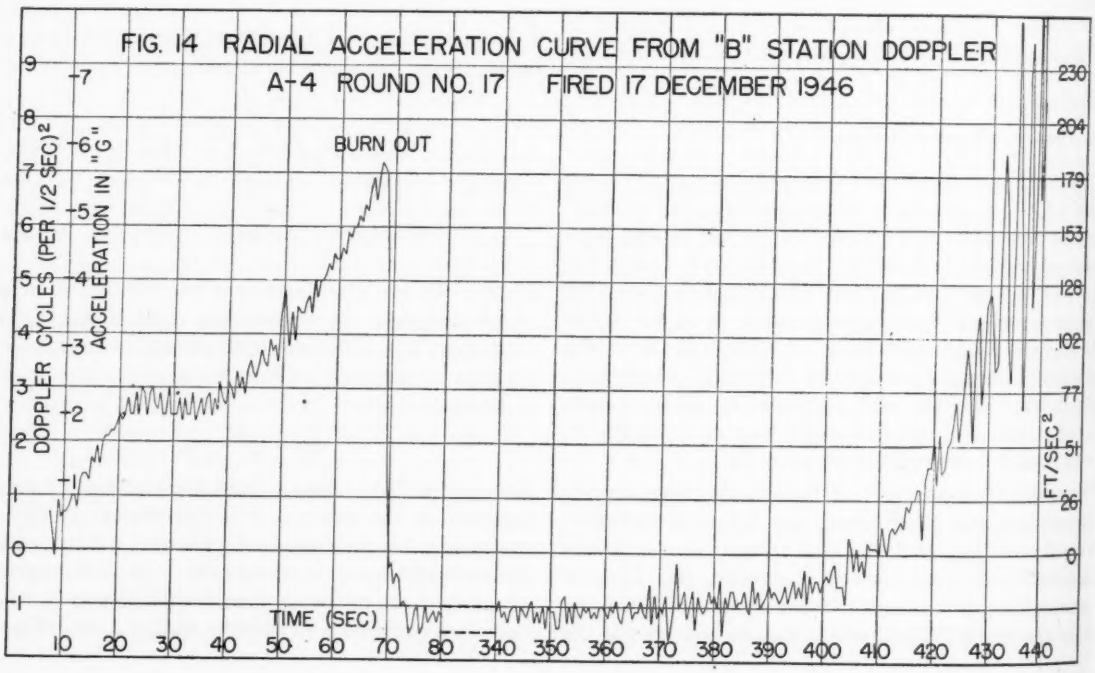
FIG. 14 RADIAL ACCELERATION CURVE FROM "B" STATION DOPPLER
A-4 ROUND NO. 17 FIRED 17 DECEMBER 1946
BURN OUT
DOPPLER CYCLES (PER 1/2 SEC)²
ACCELERATION IN "G"
FT/SEC²
TIME (SEC)

that survey errors may reasonably account for the equivalent of one-half cycle and errors in assuming the velocity of propagation in the ionosphere may account for about one-tenth of a cycle. Thus, the remaining error would appear to be due entirely to a total error in the doppler count of $1^4/_{10}$ cycles out of approximately 100,000 cycles, which seems to be entirely reasonable, considering the many factors that may contribute to such a miscount.

References

[1] Reuyl, D., *Full-Scale Free-Flight Ballistic Measurements of Aircraft Rockets by Optical Methods*, BRL Report in preparation.

[2] Hitchcock, H. P., and Reklis, V. M., *Trajectory of the Rocket A-4 During Burning Observed by Mitchell Photo-Theodolites*, BRL Report No. 639.

[3] Morse, A. P., *The Estimation of Dispersion from Differences*, BRL Report No. 557, 12 July 1945.

[4] Monthly summary No. 4–34, ORDCIT Project, Jet Propulsion Laboratory, California Institute of Technology.

[5] Physical Science Laboratory, *Report on the Method of Calculation of the Ballistic Characteristics of Rockets Launched at White Sands Proving Ground*, New Mexico College of A. and MA.

[6] Reklis, V. M., and Cassity, C. R., *The Calculation of Maximum Ordinate of an A-4 Rocket from the Conditions at Burnout*, BRL Report 655.

[7] Zug, R. S., *A Photometeoronic Method for Bomb Ballistics and for Measurements of the Flight Performance of Aircraft*, BRL Report No. 279, September 26, 1942.

[8] Atkinson, R. d'e., *Procedure for Calibrating a Tilted Ballistic Camera*, BRL Report, manuscript.

[9] Edson, J. B., *The Tracking Telescope*, BRL Report, manuscript.

[10] Kusaka, T-4 Shuichi, *Doppler Determination of Projectile Trajectory*, BRL Report No. 609.

[11] Garfinkel, Boris, *Doppler Determination of Position*, BRL Report No. 638.

Letter to the Editor

Dear Sir:

In the first part of the paper "On Airfoil Theory and Experiment" (Alan Pope, July, 1948, JOURNAL OF THE AERONAUTICAL SCIENCES) the author makes no mention of the effect of the trailing-edge angle on lift curve slope, and in the last two paragraphs of that section it is stated first that: "The highest lift curve slope is noted for the 63000 series, which also has the most rearward a.c.," and, immediately afterwards: "In general, it can only be said that airfoils whose minimum pressure peaks occur well back from the leading edge will have steeper lift curve slopes and more rearward aerodynamic center positions than the older forward pressure peak airfoils." This seems to be a contradiction, as the 63 series airfoils, although not very old, have forward suction peaks.

In the second part of the paper, the section on Drag, the author proposes a method of estimating section drag which, it seems to me, can be judged only as a rule of thumb on its ability to produce the right answer. Of the two major assumptions made, the first (that transition occurs at the minimum pressure position) is probably satisfactory at high Reynolds Numbers, but, in wind-tunnel tests at 2 to 3 million, transition is frequently further back, as must be well known to all who have done such tests, especially with transition indicators. The method of compensating for the initial thickness of the turbulent layer has no theoretical basis and can be judged only on results. Pope says that his results "came within $\Delta c_d = 0.0008$, and usually less than $\Delta c_d = 0.0004$, of the value measured in the tunnel," which, for a low-drag section, means a maximum error of 20 per cent and a probable error of less than 10 per cent, which seems hardly satisfactory. Figs. 1 and 2 herein show a comparison of the theory with further results of tests on $6x_1 - 012$ and 009 sections at $R = 34, 9 \times 10^6$, and zero lift, taken from the same report *ACR L5CO5* quoted by Pope. At 3 million the error is generally worse than 10 per cent, but at 9 million (outside the range 1 to 7 million mentioned by Pope) the agreement is good. Correction for the fact that the minimum pressure is at $0.4c$, $0.47c$, and $0.63c$ for 64, 65, and 66 series airfoils, respectively, makes little difference.

Fig. 3 demonstrates clearly that transition may not coincide with the minimum pressure peak. It shows, at $R = 3$ million and 9 million, the transition point on a flat plate having the same drag (by Squire and Young's method) as the experimental drag of the sections tested. It will be seen that at 9 million Pope's assumption is justified; at 3 million transition would have to be about $0.10c$ behind the minimum pressure point.

I suggest that the only conclusion to be reached is that, while Pope's method may give good agreement in certain cases, it would be wiser in general to use a method having a better theoretical basis.

F. CHEERS
Division of Mechanical Engineering
National Research Council
Ottawa, Canada

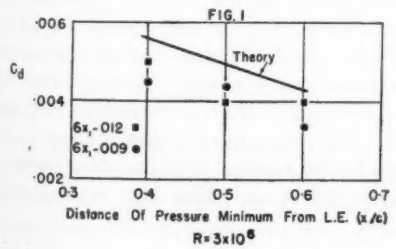

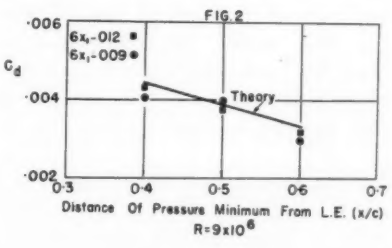

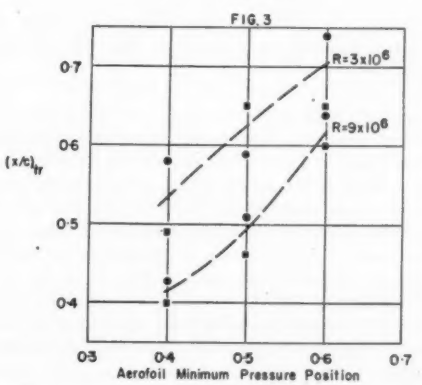

Transition Position Of Flat Plate Having Drag Of Aerofoils In Figs. 1 & 2

The Optimum Proportions of a Long Unstiffened Circular Cylinder in Pure Bending*

HERBERT BECKER†

Fairchild Engine and Airplane Corporation

SUMMARY

The problem of determining the radius and wall thickness of a minimum weight circular cylinder under pure bending is encountered during the design of a missile fuselage. Selection of any of the three common plastic moduli (secant, reduced, and tangent) for use in the buckling stress equation will yield approximately the same optimum design proportions. Furthermore, small deviations from the optimum design geometry will lead to minor weight increases. A simplified design procedure is presented which depends upon the applicability of the secant modulus theory, for which substantiating evidence is available. However, since it is not conclusive, the use of the simplified design procedure, which yields a near-optimum design with little effort, must be considered uncertain until such a time as further evidence is available to support the secant modulus theory.

In the analysis it is assumed that the buckling stress is linearly proportional to t/R, in agreement with existing data. Discussion of departures from this rule is omitted.

The development, which is entirely analytic, employs the three-parameter method of describing stress-strain curves. This leads to expressions for shell radii and weights which are easily compared for each of the three plastic modulus theories.

INTRODUCTION

When a long cylinder of small radius is subjected to a pure bending moment, the wall required to resist this load may be quite thick. Therefore, in the interest of weight minimization, it is desirable to know the optimum proportions of the cylinder cross section or, in other words, the combination of shell radius and wall thickness which will have a minimum area and which will have just sufficient strength to withstand the applied moment before the cylinder buckles.

This problem is encountered in the design of missile fuselages, which usually are of small radius and are required to support large bending moments. The expendable nature of missiles, in addition to their performance requirements, accentuates the weight problem considerably.

Received April 9, 1948.

* The author wishes to express his appreciation to George Parsons, of the Pilotless Plane Division, for the impetus he imparted to the writing of this article by his contention that appreciable variations in the shape of the material stress-strain curve would have little influence upon the optimum design weight. Credit is due George Gerard, of New York University, for originating the graphic solution, depicted in Fig. 1, of differential equations of the form of Eq. (3) involving stress and modulus as the variables. This was done several years ago during discussions between Mr. Gerard and the author concerning the problem of optimum design.

† Structures Engineer, Pilotless Plane Division.

The conditions for an optimum design require an expression for the critical buckling stress of a long circular cylinder in pure bending. As indicated by the data contained in references 1 and 2, a good approximation to this stress is obtained from Eq. (1a) for $E_e = E$ in the elastic range. Consequently, the relationship presented in Eq. (1a) will be used for the critical buckling stress during the development of the optimum design theory. An analysis of the applicability of Eq. (1a) is beyond the scope of this report. A discussion of possible variations in K and the existence of an exponent for t/R different from unity are items outside the range of this investigation and will be omitted. It will be assumed, for the purposes of analysis, that Eq. (1a) is correct.

The choice of a plastic modulus cannot be made with certainty at this time. However, it is demonstrated that, for an optimum design or for small departures from the optimum proportions, little weight discrepancy exists as a result of varying the modulus between E_s and E_t, which probably represent the limits within which the correct modulus should lie. The choice of modulus does have a strong influence upon the applicability of the simplified design procedure, which was developed because of its rapidity and simple data requirements. The material elastic modulus and yield stress are the only properties required for the use of the simplified design procedure in comparison to a need for the complete stress-strain curve (up to, and including, the knee) for the more precise theory.

Evidence for the applicability of the secant modulus exists; however, it does not appear to be conclusive. Since the simplified design procedure assumes the secant modulus to be correct in the plastic range, its usefulness is questionable at present.

The development of the design theory, which is analytic as opposed to graphic, utilizes the three-parameter description of stress-strain curves presented in reference 3, with the symbols altered to agree with the $\sigma - \epsilon$ notation for stress and strain. The use of σ_1/σ_t for the material stress-strain curve shape factor occurs frequently throughout the paper and is preferred because it utilizes two physical characteristics of the material instead of the abstract n employed throughout reference 3. The derivations of the analytic optimum stress equations are incidental to the main thesis of the article and, for this reason, have been segregated in the Appendix.

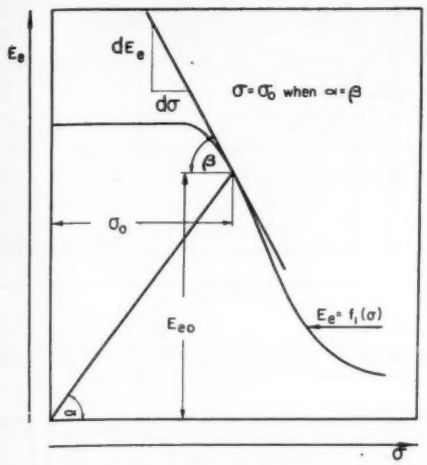

FIG. 1. Graphic solution of the optimum design equation, $(dE_e/d\sigma) + (E_e/\sigma) = 0$.

SYMBOLS

E = elastic modulus, lbs. per sq.in.
E_e = effective modulus (secant, reduced, tangent), lbs. per sq.in.
K = coefficient in critical buckling stress equation
K_L = buckling stress coefficient used in reference 2; magnitude is σ/E
K_R = coefficient in optimum radius equation
L = shell length, in.
M = external bending moments, in. lbs.
R = shell radius, in.
W = shell weight, lbs.
n = shape parameter for stress-strain curve $\{=1 + [0.3853/\log_{10}(\sigma_1/\sigma_2)]\}$ [reference 3, Eq. (29)]
t = shell thickness, in.
ϵ = strain, in. per in.
ρ = density, lbs. per cu.in.
σ = critical buckling stress = applied bending stress, lbs. per sq.in.
σ_1 = stress, on material stress-strain curve, at $E_s = 0.7E$ (Fig. 7), lbs. per sq.in.
σ_2 = stress, on material stress-strain curve, at $E_s = 0.85E$ (Fig. 7), lbs. per sq.in.
σ_{yp} = yield stress, as described by the 0.002 set criterion

Subscripts

o = optimum design
r = reduced modulus theory
s = secant modulus theory
t = tangent modulus theory

Superscripts

Prime (′) is unprimed quantity multiplied by E_s/E. (E, σ_1, and σ_2 are the three parameters used to describe stress-strain curves analytically.)

THEORY

Fundamental Equation

In order to determine the optimum proportions of a circular shell under bending forces, two conditions need to be satisfied: The applied and allowable stresses should be equal, and the shell weight must be a minimum consistent with the design requirements. These conditions may be expressed in the forms

$$\sigma = KE_e(t/R) \tag{1a}$$
$$\sigma = M/\pi R^2 t \tag{1b}$$
$$W = 2\pi\rho LRt = \text{a minimum} \tag{1c}$$

The minimization of W results in a differential equation in R and t for which there is no solution corresponding to an optimum design when the stress and modulus terms are employed. However, logarithmic differentiation of Eqs. (1) will yield expressions that can be reduced to a differential equation in σ and E_e. This leads indirectly to an optimum design through the prior determination of an optimum stress.

Logarithmic differentiation of Eqs. (1) yields

$$(d\sigma/\sigma) + (dR/R) - (dE_e/E_e) - (dt/t) = 0 \tag{2a}$$
$$(d\sigma/\sigma) + 2(dR/R) + (dt/t) = 0 \tag{2b}$$
$$dW/W = (dR/R) + (dt/t) = 0 \tag{2c}$$

These three equations involve four unknowns. The geometric terms may be eliminated, leaving an equation involving only σ and E_e, and their differentials:

$$(dE_e/d\sigma) + (E_e/\sigma) = 0 \tag{3}$$

This is the fundamental equation that must be satisfied in order to obtain an optimum shell design.

From the stress-strain curve of the shell construction material, E_e is expressible as $E_e = f_1(\sigma)$. Since Eq. (3) may be written in the form $E_e = f_2(\sigma)$, the value of σ which satisfies both these functional relations simultaneously is the optimum operating stress for the material.

Eq. (3) may be solved graphically as in Fig. 1. The plot of E_e against σ is derived from the material stress-strain curve with little difficulty. However, it is possible to solve Eq. (3) analytically using the three-parameter equations of reference 3. Analytic expressions, for the pertinent quantities to be developed below, tend to eliminate the errors accrued during cross-plotting. In addition, they are useful for evaluating effects caused by variations in the quantities appearing in the equations. For these reasons the development of the optimum design theory will be entirely analytic. The symbolism of reference 3 has been altered to conform with the $\sigma - \epsilon$ notation for stress and strain, and the analytic derivations of the optimum stress equations may be found in the Appendix, where equation numbers are preceded by capital A.

Optimum Stress Equations

The most suitable modulus to use for E_e probably would be E_s, E_r, or E_t.

Assumption 1: $E_e = E_s$.—Through substitution of E_s for E_e in Eq. (3), a simple optimum-design relation is obtainable. Upon application of the stress-strain-modulus relationships ($E_s = \sigma/\epsilon$, $E_t = d\sigma/d\epsilon$) to the following slightly modified form of Eq. (3),

$$\frac{dE_e}{d\sigma} + \frac{E_e}{\sigma} = \frac{dE_s}{d\epsilon}\frac{d\epsilon}{d\sigma} + \frac{1}{\epsilon} = 0$$

the solution follows readily. Since

$$\frac{dE_s}{d\epsilon} = \frac{d}{d\epsilon}\left(\frac{\sigma}{\epsilon}\right) = \frac{1}{\epsilon}\left(\frac{d\sigma}{d\epsilon} - \frac{\sigma}{\epsilon}\right) = \frac{1}{\epsilon}\left(E_t - E_s\right)$$

then

$$(1/\epsilon)(E_t - E_s)(1/E_t) + (1/\epsilon) = 0$$

from which

$$E_s/E_t = 2 \qquad (4)$$

The graphic determination of σ_0 from Eq. (4) is accomplished easily by plotting E_s/E_t versus σ and by determining the value of σ at which this ratio equals 2. The analytic solution of Eq. (3), as presented in the Appendix, requires that

$$\sigma_{s0}/\sigma_1 = [7/3(n-2)]^{1/(n-1)} \qquad (A6)$$

The dependence of σ_{s0}/σ_1 upon the stress-strain curve shape parameter, σ_1/σ_2, is delineated in Fig. 2. For reference, Fig. 5 contains a table listing several numerical values of n for corresponding values of σ_1/σ_2.

Assumption 2: $E_e = E_r$.—In this case the optimum design relationship embracing the various moduli [corresponding to Eq. (4) above and Eq. (5) below] will be omitted, since it is much too complicated for a graphic solution. The analytic solution of Eq. (3) for $E_e = E_r$ leads to the expression,

$$\frac{\sigma_{r0}}{\sigma_1} = \left(\frac{7(2n-3)}{3n(n-2)^2}\right)^{1/(n-1)} \qquad (A7)$$

This curve is also plotted in Fig. 2.

Assumption 3: $E_e = E_t$.—As is shown in the Appendix,

$$[(E/E_t) - 1] = n[(E/E_s) - 1] \qquad (A9)$$

By applying this expression to Eq. (3) and including the stress-strain-modulus relationships, a correspondence is obtained among the elastic, secant, and tangent moduli, and the shape factor, n, viz.:

$$EE_t/E_s^2 = 1 - (1/n) \qquad (5)$$

This equation may be solved graphically in a manner analogous to that used for Eq. (4).

The analytic optimum stress equation for $E_e = E_t$,

$$\sigma_{t0}/\sigma_1 = [7/3n(n-2)]^{1/(n-1)} \qquad (A8)$$

is plotted in Fig. 2, together with the corresponding curves for $E_e = E_s$ and $E_e = E_r$.

Comparison Formulas

Examination of Eqs. (A6), (A7), and (A8) reveals the following equalities:

$$\sigma_{s0}/\sigma_1 = (n)^{1/(n-1)}(\sigma_{t0}/\sigma_1) \qquad (6a)$$

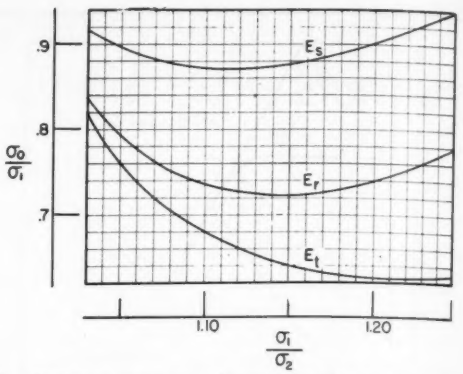

FIG. 2. Optimum stress as a function of the shape parameters (σ_1 and σ_2) and effective modulus.

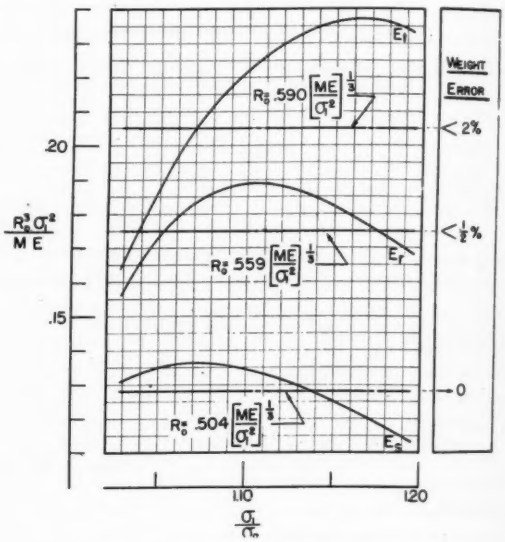

FIG. 3. Design chart for all three moduli.

$$\sigma_{r0}/\sigma_1 = [(2n-3)/(n-2)]^{1/(n-1)}(\sigma_{t0}/\sigma_1) \qquad (6b)$$

These equations permit rapid evaluation of the differences among the magnitudes of σ_0/σ_1 arising from the three choices of E_e for a particular material.

Optimum Design

Shell Radius.—Eqs. (1) may be combined into a form suitable for the optimum design of a long cylinder in pure bending. From Eqs. (1a) and (1b),

$$M/\pi R^2 t = (M/\pi R^3)(R/t)$$

and

$$R/t = KE_e/\sigma$$

or

$$R^3 = MKE_e/\pi\sigma^2 \qquad (7)$$

This relation, when modified slightly, provides a simple method for the determination of the shell radius. Since

$$E_e/\sigma^2 = (E/\sigma_1^2)[(E_e/E)/(\sigma/\sigma_1)^2]$$

then Eq. (7) may be revised to read

$$R^3\sigma_1^2/ME = (K/\pi)[(E_e/E)/(\sigma/\sigma_1)^2] \qquad (7a)$$

The optimum radius is obtained from Eqs. (7) or (7a) when $E_e = E_{e0}$ and $\sigma = \sigma_0$. Since the right side of Eq. (7a) is determined uniquely for any particular value of σ_1/σ_2 when $\sigma = \sigma_0$, then the optimum design curves of Fig. 3 may be drawn from which it is possible to construct nomograms for rapid design work.

The shell thickness is obtainable from Eq. (1b), after σ_0 has been found through use of the relation

$$\sigma_0 = \sigma_1(\sigma_0/\sigma_1)$$

Shell Weight.—According to Eq. (1c),

$$W = 2\pi\rho LRt \qquad (1c)$$

From Eqs. (1a) and (1b),

$$\sigma = KE_e(t/R) = M/\pi R^2 t$$

or

$$Rt = (MR/K\pi E_e)^{1/3}$$

By substituting Rt into Eq. (1c) and utilizing Eq. (7), the shell weight is found to be

$$W = 2\pi\rho L(M^2/\pi^2 KE_e\sigma)^{1/3} \qquad (8)$$

The shell weight will be a minimum when $\sigma = \sigma_0$.

The largest weight difference will exist between the shells designed on the bases of secant modulus and tangent modulus theories, with the reduced modulus design weight lying between them. The ratio of the tangent modulus optimum weight to the secant modulus optimum weight is equal to

$$W_{t0}/W_{s0} = (E_{s0}\sigma_{s0}/E_{t0}\sigma_{t0})^{1/3} \qquad (9)$$

In the Appendix it is shown that

$$E/E_{s0} = 1 + (3/7)(\sigma_{s0}/\sigma_1)^{n-1} \qquad (A3)$$

From Eq. (6a),

$$(\sigma_{s0}/\sigma_1)^{n-1} = [(n)^{1/(n-1)}(\sigma_{t0}/\sigma)]^{n-1}$$

or

$$\sigma_{s0}/\sigma_1 = (n)^{1/(n-1)}$$

Also,

$$\frac{E}{E_{s0}} = 1 + \frac{3}{7}\,n\left(\frac{\sigma_{t0}}{\sigma_1}\right)^{n-1} = \frac{E}{E_{t0}} \qquad (A4)$$

Consequently, $E_{s0} = E_{t0}$ and

$$W_{t0}/W_{s0} = (n)^{1/3(n-1)} \qquad (9a)$$

(Analytically, $E_{r0} \neq E_{s0}$. However, since the difference between the optimum moduli is less than $^1/_4$ per cent for $\sigma_1/\sigma_2 < 1.200$, then for all practical purposes, $E_{r0} = E_{s0} = E_{t0}$.)

According to Eq. (8) the optimum-weight ratios for the secant and tangent modulus theories will be much closer to unity than will the corresponding stress ratios. Both these ratios have been plotted in Fig. 4, which demonstrates that for $\sigma_1/\sigma_2 < 1.14$ ($n > 8$) the maximum weight discrepancy between the two theories is less than 10 per cent, whereas the stress discrepancy is nearly three times as great. This range of σ_1/σ_2 corresponds to that in which most of the high-strength metal alloys will be found.

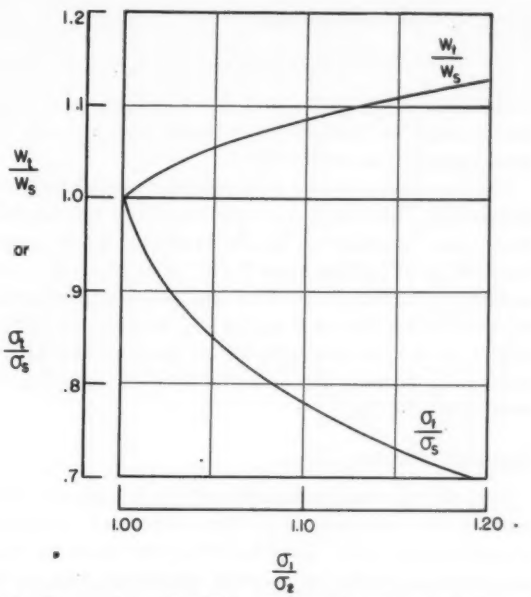

FIG. 4. Comparison of weight and stress discrepancies between the secant and tangent modulus theories.

Nonoptimum Design

The effect upon W produced by deviations of R from the optimum value may be obtained with the aid of Eqs. (7) and (8).

$$W/W_0 = (E_{e0}\sigma_0/E_e\sigma)^{1/3} \qquad (10)$$

and

$$\frac{R}{R_0} = \left(\frac{E_e}{E_{e0}}\left[\frac{\sigma_0}{\sigma}\right]^2\right)^{1/3} = \frac{\sigma_0/\sigma}{W_0/W}$$

or

$$(R/R_0) \times (W/W_0) \times (\sigma/\sigma_0) = 1 \qquad (11)$$

The result of plotting W/W_0 against R/R_0 is depicted in Fig. 5 for several values of σ_1/σ_2. The curves for the secant, reduced, and tangent modulus theories are practically coincident for each value of σ_1/σ_2 and appear as single lines in the figure.

The plotting procedure requires the determination of σ_0/σ_1 (for the particular value of σ_1/σ_2) and the selection of several arbitrary values of σ/σ_1. From these stress ratios, E/E_0 and E/E_e (corresponding to σ_0/σ_1 and σ/σ_1, respectively) are computed, using Eqs. (A3), (A4), and (A5). Then W/W_0 may be calculated from the expression

$$\frac{W}{W_0} = \left[\frac{(E/E_e)/(\sigma/\sigma_1)}{(E/E_{e0})/(\sigma_0/\sigma_1)}\right]^{1/3} \qquad (10a)$$

and R/R_0 is obtainable from

$$R/R_0 = (W_0/W)[(\sigma_0/\sigma_1)/(\sigma/\sigma_1)] \qquad (11a)$$

The values of W/W_0 and R/R_0 calculated in this fashion may be plotted as ordinate and abscissa on graph paper, as shown in Fig. 5.

The computations for this plotting procedure yield information concerning the dependence of the bending stress upon variations in the shell radius. These curves have also been plotted upon Fig. 5, from which it is now possible to determine the effect of a nonoptimum operating stress upon the shell radius and weight. As in the case of the weight ratio graphs, all three moduli lead to stress ratio curves that lie virtually along one line for each value of σ_1/σ_2.

Choice of Modulus

The effective modulus applicable in the plastic range probably is close to one of the three discussed during the preceding analysis. Some basis may be found for using the secant modulus, in recently published data on the buckling stresses developed in axially compressed curved magnesium-alloy panels.[5] These data show good agreement with a buckling stress equation of the form

$$\sigma = KE_s(t/R) \qquad (12)$$

which is identical to Eq. (1b) with $E_e = E_s$. This suggests the possibility of applying the secant modulus theory to shells in bending, since the shape and size of the buckles in an axially compressed cylinder resemble closely those formed in a shell of the same geometry sustaining bending loads (cf. reference 2).

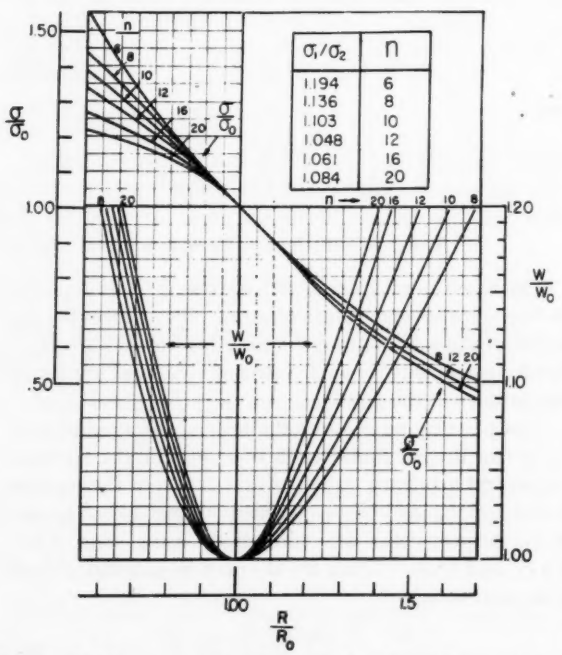

FIG. 5. Weight, stress, and radius variations for all three moduli.

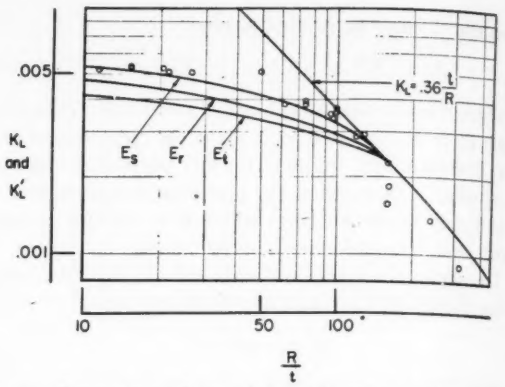

FIG. 6. Comparison of test data with secant, reduced, and tangent modulus theories for critical buckling stress.

Additional evidence to support the use of the secant modulus may be derived from references 1 and 2, which contain data on shells in bending wherein the range of buckling strains extends from small elastic values to extremely large plastic values. The elastic range equation is represented by the straight line of Fig. 6, in which the buckling coefficient used in reference 2 is plotted as a function of R/t. The symbol K_L is used to distinguish this coefficient from the K appearing in Eq. (1a), since $K_L = K(t/R)$ in the elastic range.

The magnitude of K_L in the plastic range will have to be modified in order to bring the theory into closer agreement with the test data. Assuming the secant modulus to be applicable, then the modified value of K_L will be

$$K'_L = K_L(E_s/E) \qquad (13)$$

The buckling stress equation of reference 2 is

$$\sigma = K_L E \qquad (14)$$

in the elastic range or upon the straight line of Fig. 6. In the plastic range, K_L in Eq. (14) must be replaced by K_L', in which case the new buckling stress equation becomes

$$\sigma' = K_L'E = [K_L(E_s/E)]E = K_L E_s \qquad (14a)$$

As is demonstrated in the original paper on the secant modulus theory,[4] σ' is the stress taken from the material stress-strain curve at the same strain as σ/E. Thus, dividing Eq. (14a) by Eq. (14) leads to a simple expression for K_L':

$$\sigma'/\sigma = K_L'/K_L \qquad (15)$$

Values of K_L' taken from the test data of reference 1 appear in Fig. 6, together with the theoretical curves for the secant, reduced, and tangent modulus.

The stress-strain data for 17S-T aluminum-alloy sheet, which appear in reference 6 and which were used to construct these curves, do not extend beyond a strain corresponding to $R/t = 40$. Consequently, it was

necessary to obtain large strain data with the three-parameter method [Eq. (A1) in the Appendix].

In reference 1 the test data are presented in the form of σ plotted against R/t. In reference 2 the values of σ were divided by E ($= 10^7$ lbs. per sq.in.) in order to permit the plot of K_L versus R/t. The same procedure was used for the test points of Fig. 6. However, since E for the alloy shown in Fig. 7 is equal to 1.067×10^7 lbs. per sq.in., the points of reference 1 were divided by this value before they were plotted on Fig. 6, which indicates the applicability of the secant modulus to be justified and bolsters the contention that Eq. (12) is applicable to the determination of the critical buckling stress of a long cylinder in pure bending.

Simplified Design Procedures

A fairly good approximation to the optimum design proportions may be obtained by using the expressions for R_0 which appear on the straight lines of Fig. 3. The weight discrepancies involved, compared to the minimum value at optimum design, are indicated on the graph. The use of the secant modulus theory leads to negligible error, as may be easily verified by using Fig. 5.

On the assumption that $\sigma_{yp} = \sigma_1$ (where σ_{yp} is the stress corresponding to 0.002 set), a further simplification is possible; the yield stress may be used, instead of σ_1, in the equations for R_0 shown in Fig. 3. In this case the expression for the optimum shell radius becomes

$$R_0 = K_R(ME/\sigma_{yp}^2)^{1/3} \tag{16}$$

When

$$E_e = E_s, \quad K_R = 0.504$$
$$E_e = E_t, \quad K_R = 0.559$$
$$E_e = E_t, \quad K_R = 0.590$$

On the hypothesis that the use of the secant modulus is permissible, assuming $\sigma_{yp} = \sigma_0$ will lead to little weight error as compared to the minimum design. On the other hand, considerable weight discrepancies are realizable using $\sigma_{yp} = \sigma_0$ in conjunction with the reduced modulus or with the tangent modulus. This is evident from Table 1, which contains a comparison of the weight errors for several materials using $\sigma = \sigma_{yp}$ in Eqs. (7) and (8) instead of $\sigma = \sigma_0$ (in which case $E_e = E_{e0}$). Obviously, the weight discrepancies are supportable for $E_e = E_s$. The average secant modulus theory error is 6 per cent, compared to the minimum reduced modulus theory error of 16 per cent. The rest of the errors, except for the 21 per cent E_r discrepancy, are 30 per cent or more and cannot be read on the graph of Fig. 5.

A simple, rapid design procedure may be devised on the basis of these data. R_0 may be computed from Eq. (16) using $K_R = 0.504$, or

$$R_0 = 0.504(ME/\sigma_{yp}^2)^{1/3} \tag{17}$$

The shell thickness then may be determined from Eq. (1b) in the form

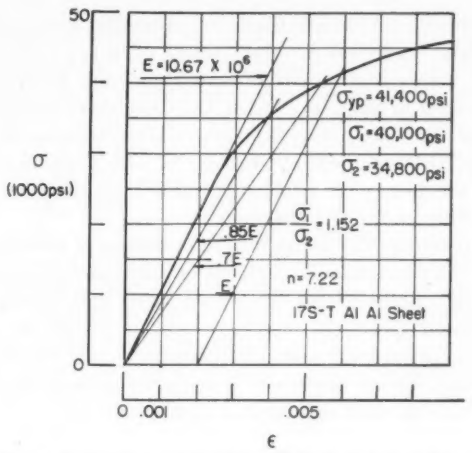

FIG. 7. A stress-strain curve for 17S-T aluminum-alloy sheet.

$$t_0 = M/\pi R_0^2\sigma_{yp} \tag{18}$$

This method has the advantage of eliminating the need for a stress-strain curve of the structural material to be used for the shell, which is necessary for the determination of σ_1, and using the yield stress instead, which is one of the fundamental mechanical properties usually furnished by the material manufacturer.

DISCUSSION.

Simplified Design Procedure

For design purposes, a rapid, reasonably close approximation to the optimum proportions is more desirable than a precise, slightly more involved calculation procedure. Since Eqs. (17) and (18) are readily adaptable to the construction of design curves for the various structural materials and yield a near-optimum shell geometry, it would be worth while to examine, in some detail, the factors affecting the applicability of these equations.

It was assumed, in developing the simplified design equations [Eqs. (17) and (18)], that $\sigma_{yp} = \sigma_1 = \sigma_0$, and it was shown that the weight error involved in such an assumption is small if $E_e = E_s$. This is apparent from Fig. 2, wherein it is demonstrated that σ_{s0}/σ_1 does not depart very much from unity and from Eq. (10a), which indicates that the error will be reduced considerably because of the cube root. As is evident from Table 1, $\sigma_{yp} \rightarrow \sigma_1$ for the materials listed, and any discrepancy between the two stresses will be reduced to a minute value by the cube root of Eq. (10a). Obviously, then, the primary factor controlling the use of the simplified design equations is the choice of the secant modulus for E_e.

Although evidence to indicate the accuracy of such a choice has been presented, it cannot be considered conclusive because of the nature of the data. The tests described in reference 1 were conducted upon both tubes

and sheets, for which there undoubtedly was a considerable variation in the values of σ_1/σ_2 and σ_{yp}. These errors alone could account for a large portion of the scatter in the data. Also, the three theoretical K_L' curves were determined from material stress-strain data, which, although perhaps typical of 17S-T aluminum-alloy sheet, may deviate considerably from the material properties of the test specimens.

Apparently, the solution to the problem of the choice of E_e can come only through the examination of existing test data and perhaps the construction and testing of additional specimens. At any rate, it cannot be answered conclusively now. Consequently, the use of the simplified design procedure is not substantiated by the test data but only is indicated as a possibility.

Limitations of Applicability

The problem investigated in this paper is the determination of the lightest weight shell that will support a specific pure bending moment. It was assumed tacitly that the pure shell is the lightest type of construction which could be found to support the applied moment. Within a certain range of moments this will be true. However, as the shell radius is required to increase with the applied moment, a critical radius will be attained beyond which some other type of construction will be lighter. Consequently, it is apparent that only one band of the bending moment spectrum has been investigated in this report. It is necessary to analyze additional types of construction—such as stringer, or longeron, stiffened shells—to determine their applicable moment ranges. When this has been done, a particular bending moment becomes identified with a particular type of construction which will yield an optimum design for that moment.

Obviously, the optimum designs obtained for pure bending must be modified for shells subjected to additional loads from axial, torsional, and transverse shearing forces. In order to evaluate these effects, it might be useful to determine the requirements for an optimum design pertinent to each separate loading condition. The axial case is important in missile design because of the large power-plant thrust developed. However, it might be difficult to determine a simplified design procedure for axially compressed cylinders, since data in the plastic range are difficult to find, as a result of which

Table 1 - Comparison of weight errors, using $\sigma_{yp} = \sigma_1 = \sigma_0$ for all three plastic modulus theories.

Item	Effective Modulus Theory	Aluminum Alloy Sheet					Stainless Steel Sheet		
		17 S - T[a]	24 S - T[b]		75 S - T[b]		Stainless W[c]	Type 301[d]	Type 304[d]
		Room Temp.	Room Temp.	400°F	Room Temp.	400°F	Room Temp.	Room Temp.	Room Temp.
E (10^6 psi)		10.67	10.50	9.60	10.42	9.35	28.30	26.00	25.68
σ_1 (10^3 psi)		40.10	45.60	35.30	72.60	31.00	191.0	33.10	30.60
σ_2 (10^3 psi)		34.80	41.25	32.30	69.10	28.25	171.0	30.10	25.20
σ_{yp} (10^3 psi)		41.40	46.00	36.00	71.50	31.75	185.0	37.05	36.70
σ_1 / σ_2		1.152	1.106	1.093	1.033	1.088	1.117	1.100	1.213
n		7.22	9.83	10.95	18.10	11.50	9.08	10.30	5.55
σ_0 / σ_1	Secant	.878	.872	.874	.894	.875	.872	.873	.910
	Reduced	.724	.733	.740	.787	.744	.729	.735	.748
	Tangent	.640	.674	.687	.754	.693	.663	.669	.686
σ_0 (10^3 psi)	Secant	35.20	39.75	30.85	65.00	27.10	161.7	28.90	27.85
	Reduced	29.05	33.40	26.10	57.30	23.05	139.2	24.30	22.85
	Tangent	25.60	30.70	24.25	54.90	21.50	126.6	22.15	19.15
σ_{yp} / σ_0	Secant	1.175	1.157	1.168	1.100	1.172	1.142	1.282	1.318
	Reduced	1.425	1.377	1.380	1.247	1.377	1.330	1.525	1.606
	Tangent	1.615	1.498	1.485	1.279	1.477	1.460	1.672	1.917
R / R_0	Secant	.82	.83	.81	.86	.80	.85	.69	.75
	Reduced	.60	.58	—	—	—	.65	—	—
	Tangent	—	—	—	—	—	—	—	—
W / W_0	Secant	1.04	1.04	1.07	1.04	1.07	1.03	1.13	1.07
	Reduced	1.19	1.21	—	—	—	1.16	—	—
	Tangent	—	—	—	—	—	—	—	—

a - Figure 7 b - Alcoa Aluminum Research Laboratories Data c - Allegheny Ludlum Steel Corporation Data

d - Smith, R., Wyche, E. H., and Gorr, W. W., - "A Precipitation-Hardening Stainless Steel of the 18 Per Cent Chromium, 8 Per Cent Nickel Type", AIMME Publication No. 2006, February, 1946.

the applicable modulus would be uncertain. Some additional test data would be necessary to clarify this point.

Conclusions

The optimum radius of a long circular shell resisting a pure bending moment may be expressed as

$$R_0 = K_R(ME/\sigma_{yp}^2)^{1/3} \tag{16}$$

When

$$E_e = E_s, \quad K_R = 0.504$$
$$E_e = E_r, \quad K_R = 0.559$$
$$E_e = E_t, \quad K_R = 0.590$$

If the coefficient for the tangent modulus is used in Eq. (16) and the secant modulus is found to be applicable, the weight discrepancy will be 10 per cent or less (in excess of the secant modulus theory weight) for most structural materials. Evidently, then, knowledge of the correct plastic modulus is not necessary for optimum design.

The variation of σ/σ_0 and $W/\dot{W}_0$ with R/R_0 is independent of the choice of modulus, and for small departures from the optimum design geometry the weight increase is negligible. Consequently, it is not necessary to know which plastic modulus is correct for small departures from the optimum design.

The use of the simplified design procedure assumes that $\sigma_0 = \sigma_{yp}$. This is a reasonable assumption only if the secant modulus is applicable in the plastic range. The evidence to support this contention is not conclusive. Consequently, it will be necessary to obtain additional support for the applicability of the plastic modulus theory before the simplified design procedure can be used with complete freedom. Should the applicability of the secant modulus be demonstrated, then the simplified design procedure would provide a rapid, close approximation to the optimum shell proportions, requiring only a knowledge of the applied moment, the material elastic modulus, and the material yield stress as defined by the 0.002 set criterion.

Appendix A

(Derivations of the analytic stress, strain and modulus relations are based upon the three-parameter method of describing stress-strain curves.)

Modulus Relationships

From reference 3, Eq. (2),

$$\epsilon = (\sigma/E) + C(\sigma/E)^n \tag{A1}$$

From reference 3, Eq. (7),

$$C(\sigma_1/E)^{n-1} = (1 - m_1)/m_1 = 3/7 \tag{A2}$$

since m_1 is equal to 0.7 [reference 3, Eq. (22)].

Multiplying Eq. (A1) by E/σ leads to

$$E/E_s = 1 + C(\sigma/E)^{n-1}$$

However,

$$C\left(\frac{\sigma}{E}\right)^{n-1} = C\left(\frac{\sigma_1}{E}\right)^{n-1}\left(\frac{\sigma}{\sigma_1}\right)^{n-1} = \frac{3}{7}\left(\frac{\sigma}{\sigma_1}\right)^{n-1}$$

Consequently,

$$E/E_s = 1 + (3/7)(\sigma/\sigma_1)^{n-1} \tag{A3}$$

From Eq. (15) of reference 3,

$$E/E_t = 1 + (3/7)n(\sigma/\sigma_1)^{n-1} \tag{A4}$$

From Eq. (18) of reference 3,

$$\frac{E}{E_r} = \frac{1}{4}\left[1 + \sqrt{1 + \frac{3}{7}n\left(\frac{\sigma}{\sigma_1}\right)^{n-1}}\right]^2 \tag{A5}$$

Optimum Stress Equations

Using the secant modulus in Eq. (3)

$$\frac{dE_e}{d\sigma} = \frac{-(3/7)(n-1)(\sigma/\sigma_1)^{n-1}E/\sigma}{[1 + 3/7(\sigma/\sigma_1)^{n-1}]^2} = \frac{-E_e}{\sigma} = \frac{-E/\sigma}{1 + (3/7)(\sigma/\sigma_1)^{n-1}}$$

or

$$(3/7)(n-1)(\sigma/\sigma_1)^{n-1} = 1 + (3/7)(\sigma/\sigma_1)^{n-1}$$

from which

$$\sigma_{s0}/\sigma_1 = [7/3(n-2)]^{1/(n-1)} \tag{A6}$$

When $E_e = E_r$,

$$dE_e/d\sigma = -4 \times \frac{(3/7)n(n-1)(\sigma/\sigma_1)^{n-1}E/\sigma}{[1 + \sqrt{1 + (3/7)n(\sigma/\sigma_1)^{n-1}}]^3\sqrt{1 + (3/7)n(\sigma/\sigma_1)^{n-1}}}$$

or

$$\frac{3}{7}n(n-1)\left(\frac{\sigma}{\sigma_1}\right)^{n-1} = \left[1 + \sqrt{1 + \frac{3}{7}n\left(\frac{\sigma}{\sigma_1}\right)^{n-1}}\right]\sqrt{1 + \frac{3}{7}n\left(\frac{\sigma}{\sigma_1}\right)^{n-1}}$$

from which

$$\sigma_{r0}/\sigma_1 = [7(2n-3)/3n(n-2)^2]^{1/(n-1)} \tag{A7}$$

Using $E_e = E_t$ in Eq. (3),

$$\frac{dE_e}{d\sigma} = -\frac{(3/7)n(n-1)(\sigma/\sigma_1)^{n-1}E/\sigma}{[1+(3/7)n(\sigma/\sigma_1)^{n-1}]^2} = -\frac{E/\sigma}{1+(3/7)n(\sigma/\sigma_1)^{n-1}}$$

or

$$\sigma_{t0}/\sigma_1 = [7/3n(n-2)]^{1/(n-1)} \qquad \text{(A8)}$$

Incidental Equation

The expression to be derived below is used in conjunction with Assumption 3: $E_e = E_t$.

Revising Eqs. (A3) and (A4) to read

$$(E/E_s) - 1 = (3/7)(\sigma/\sigma_1)^{n-1}$$
$$(E/E_t) - 1 = (3/7)n(\sigma/\sigma_1)^{n-1}$$

and dividing the first into the second, leads to the relation

$$[(E/E_t) - 1] = n[(E/E_s) - 1] \qquad \text{(A9)}$$

References

[1] Younger, J. E., *Principle of Similitude as Applied to Research on Thin-Sheet Structures*, Aeronautical Engineering (Trans., A.S.M.E.), pp. 163–169, October-December, 1933.

[2] Lundquist, E. E., *Strength Tests of Thin-Walled Duralumin Cylinders in Pure Bending*, N.A.C.A. T.N. No. 479, December, 1933.

[3] Ramberg, W., and Osgood, W. R., *Description of Stress-Strain Curves by Three Parameters*, N.A.C.A. T.N. No. 902, July, 1943.

[4] Gerard, G., *A Secant Modulus Method for Determining Plate Instability Above the Proportional Limit*, Journal of the Aeronautical Sciences, Vol. 13, No. 1, pp. 38–44, 48, January, 1946.

[5] Schuette, E. H., *Buckling of Curved Sheet in Compression and Its Relation to the Secant Modulus*, Journal of the Aeronautical Sciences, Vol. 15, No. 1, pp. 18–22, January, 1948.

[6] Heimerl, G. J., and J. Albert Roy, *Column and Plate Compressive Strengths of Aircraft Structural Materials—17S-T Aluminum Alloy Sheet*, N.A.C.A. Wartime Report L-20 (ARR L5F08), June, 1945.

Announcing a New Department . . . Readers' Forum

It has been suggested by several members of the I.A.S. Editorial Committee that the *Journal* open a special department to fill the need for the more immediate communication of essential results of research in the greatly expanded and accelerated fields of the aeronautical sciences. Therefore, it has been decided to establish a new department, the "Readers' Forum," which will include letters to the editor for the quick publication of (1) brief reports of important findings in aeronautical sciences and (2) discussions of papers published in the *Journal*.

Specifications for Submission of Material

(1) All letters should be accompanied by a suggested short title, giving some indication to the reader of the subject under discussion.
(2) These letters should not exceed 800 words in length.
(3) Publication will be completed 6 to 8 weeks after receipt of the material.
(4) The Editorial Committee will not hold itself responsible for the opinions expressed by the correspondents, and no proofs will be sent to the authors.
(5) All letters should be double-spaced.

It is hoped that the new department may be started with the January, 1949, issue of the *Journal*. Contributions should be sent to:

Editor, Journal of the Aeronautical Sciences
2 East 64th street
New York 21, New York

The Relative Merits of Rotary Compressors

D. G. SAMARAS* AND R. A. TYLER†
National Research Council of Canada

SUMMARY

The relative merits of various types of rotary compressors are assessed in the light of the available test data that could be considered sufficiently reliable for the purpose. The theoretical grounds on which such an analysis may be legitimately made are discussed, and the strict requirements of the theory are relaxed sufficiently to enable a graphical comparison to be made on the simple basis of small stage efficiency and load factor. The resulting curves are interpreted with due allowance for the necessary departure of this representation of the test data from that required by the theory. It is concluded that the various types of rotary compressors are each characterized by a particular value of the load factor at which the efficiency for the corresponding compressor type is a maximum and departure from which involves a comparatively rapid loss of efficiency. Furthermore, the data analyzed and the theoretical considerations indicate that the maximum efficiency increases from one compressor type to another of lower characteristic load factor. As a result of this it would appear that the axial-flow compressor is, currently, more efficient than the centrifugal type to the extent of about 10 per cent.

NOTATION

φ	= $Q/[(\pi/4)D^2(1-\nu^2)u]$, flow coefficient
ψ	= $2gH/u^2$, pressure coefficient
Q	= rate of volume flow (cu.ft. per sec.)
D	= rotor tip diameter (ft.)
ν	= hub-diameter ratio, taken as zero for centrifugal compressors
u	= rotor tip speed (ft. per sec.)
H	= stage head (ft.lbs. per lb.)
l	= $(2gH)^{3/4}/2\sqrt{\pi}N\sqrt{Q}$, load factor
N	= rotor speed of rotation (r.p.s.)
Re	= Reynolds Number
Ro	= Roughness Number
M	= Mach Number
Γ	= circulation (sq.ft. per sec.)
$\frac{P_u}{P_u}$	= compressor overall total pressure ratio
η_∞	= small stage efficiency
$\eta_{tot.}$	= overall compressor efficiency
L	= energy added to the fluid (ft.lbs.)
q	= volume (cu.ft.)

INTRODUCTION

THE PRESENT CENTURY has seen a shift of emphasis from the class of machinery covered by the term "reciprocating" to the class that may be referred to as "rotary" machinery. Since the turn of the century, notable and far-reaching advances have taken place in this field, outstanding among which has been the development of the gas-turbine power plant for power and propulsive purposes. At the heart of the gas-turbine power plant lies the rotary compressor, fulfilling, as it does, a vital pumping function on which the power plant depends for its ability to do work. Various types of rotary compressors have been developed, the more important of which are the axial and centrifugal "dynamic flow" compressors, which depend for their operation on rotating blades or vanes, and rotary displacement compressors involving a positive displacement of the fluid by rotating mating lobes or gear teeth.

The selection of the particular type of compressor to be employed in a given power plant is based on an engineering compromise between the various demands of performance, space, weight, economy, and cost and depends on the duty the machine is called upon to perform. For a particular application one type may be expected to meet the requirements of such a compromise more satisfactorily than any other. In the field of aircraft gas turbines, where the initial demand is for high performance at high efficiency, the choice is confined, at the present time, to the axial and centrifugal types. Each of these compressor types has its own advantages and disadvantages. The relative importance of the pros and cons is likely, in the future, to undergo considerable change as the development of new high-speed aircraft forms proceeds and advances in turbine design and performance continue, but today the choice between the two compressor types appears to be a difficult one and a matter for argument. Some engineers favor a combination of the two types, and power plants embodying this view are in production. The National Research Council of Canada has for some years past considered the relative merits of the axial type, and its advantages and disadvantages have been discussed previously.[1, 2] Much verbal controversy has centered around the question of the relative merits of the two types, but nowhere in the literature does there appear to be a systematic analysis of the problem leading to definite conclusions based on a sound theoretical foundation. The purpose of the present paper is to examine the problem in a scientific manner and, as a result, by making intelligent statistical use of the reliable experimental data available, to put the merits of each compressor in the right perspective.

For completeness, the examination includes all machines that could be categorized as "rotary pumps" and for which reliable data were available. These include (besides the two types of main interest) turbine pumps, Roots and Lysholm blowers, "angular" compressors, and propellers. Centrifugal and axial-flow compressors

Received October 1, 1947. Revised and received April 6, 1948.

* In Charge of Gasdynamics.
† Assistant Research Engineer.

have had, of course, wide application in fields other than that of gas-turbine power plants, and these applications (e.g., radial superchargers for reciprocating aircraft engines, axial-flow cooling fans) have also been included. Similar methods to those of the present paper have been used previously by Weber[3] in examining the specific speed of water turbines, centrifugal pumps, windmills, and propellers and by Sörensen[4] in correlating data on steam turbines.

Similarity

The conclusions drawn from a statistical examination of experimental data as to the general laws relating the behavior of particular machines are legitimate only if comparison is made in accordance with the principle of similarity. Physical similarity may be said to exist in measurable physical phenomena that appear in geometrically similar constructions and which result from the same physical causes. Geometric similarity between two constructions implies that each construction can be represented by the same construction if appropriate changes are made in the scale of length used to measure them. Time similarity can be specified by a similar definition. Complete physical similarity requires, in addition to geometric and time similarity, that the dynamic, energetic, chemical, and electrical fields of the systems compared also be similar. Completely physically similar processes are not only described by the same analytical expressions but are represented by the same mathematical functions leading to the same characterizing nondimensional parameters. In practice, because of the complexity of the processes involved, it is necessary to sacrifice a certain amount of rigidity in the application of the similarity principle. Flow systems are compared which are not strictly similar in the complete sense defined above but are similar in their essential features. That is to say, only a few of the processes involved are considered as important, the remainder or secondary processes being disregarded with the corrections required to be made by their omission being always kept in mind. Thus, depending chiefly on the nature of the problem, the important processes are separated from those of secondary importance and are used as the basis for analysis. For the sake of simplicity, it is convenient to deal only with the case of a perfect gas; the results obtained will apply approximately to saturated vapors.

The most general characteristics of a rotary compressor are the flow coefficient φ, the pressure coefficient ψ, and the small stage efficiency η_∞. (For the definition of these and subsequent symbols see "Notation.") It has been experimentally found, recently, by Hablützel[5] that, for low Mach Numbers, the performance characteristics of a rotary compressor are not appreciably affected by the substitution of water for air as the flow medium, and from a nondimensional analysis of the flow[6] it has been established that

$$\psi = f_1(\varphi, Re, M, Pr, Ro) \quad (1)$$

$$\eta_\infty = f_2(\varphi, Re, M, Pr, Ro) \quad (2)$$

for systems in which the conditions of essential similarity, outlined above, obtain. Between various systems of such a nature the functions f_1 and f_2 will vary in form, although they still will be dependent on the same variables. Such systems are considered in this paper to be exemplified by the various types of rotary compressors.

Considering the flow medium as a particular ideal gas, the influence of the Prandtl Number is unimportant and may be neglected, although it is important to bear in mind that, among the secondary processes ignored in the above relationships, those involving other heat transfer nondimensional parameters (e.g., the Nusselt Number *Nu* and Grashof Number *Gr*) may assume importance in flows involving large density and temperature variations. Examples involving such flows must not be compared with other examples of the same system, on the basis of the above relationships, unless due allowance be made for this divergence.

The influence of the Reynolds Number *Re* is of considerable importance. A great deal of effort has been directed toward deriving the effect of Reynolds Number on the characteristics of axial-flow compressors, and a large amount of experimental data exists.[7] Unfortunately, little work appears to have been done on centrifugal and other types of compressors in this respect, although a fundamentally similar behavior would be expected to exist. Fig. 1 shows the results obtained on axial-flow compressors. The optimum efficiency increases rapidly with Reynolds Number up to value for *Re* of about 10^5, beyond which the influence of Reynolds Number, although still apparent, is considerably less. The influence of compressibility in these tests was avoided by the use of low Mach Numbers, and the Reynolds Number used is based on the mean axial velocity and the blade chord.

Mostly because of the difficulty of separating the respective influences of the Reynolds and Mach Numbers, quantitative information regarding the latter is meager. The results of Encke[8] show the combined influence of the two parameters on compressor characteristics. Qualitatively, the effect of Mach Number would appear to result in a greater sensitivity of the pressure coefficient ψ and the efficiency η to a change in flow coefficient, with increase of Mach Number. The characteristic curves of the compressor become steeper and the choking mass flow decreases. At high values of the Mach Number, greater than a certain critical value depending on the compressor, the efficiency falls rapidly with the large increase of rotor resistance and the dissipation of energy in shock waves.

The influence of surface roughness, characterized by the nondimensional parameter *Ro*, has been extensively investigated.[9, 10] The roughness number *Ro* is usually taken to be the ratio of the statistical mean height of the

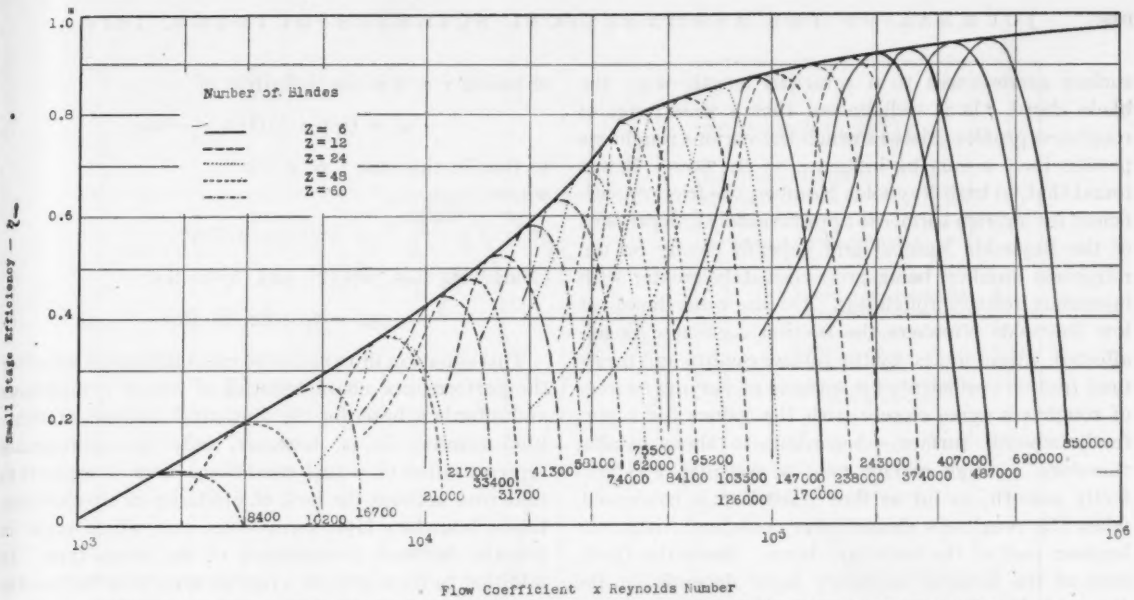

FIG. 1. Variation of the efficiency with flow coefficient for Reynolds Numbers from 8,000 to 850,000.

TABLE I

EXPERIMENTAL PERFORMANCE DATA FOR ROTARY COMPRESSORS

POINT NUMBER	CATEGORY	TYPE	SOURCE OF INFORMATION	FLUID FLOW QUANTITY LBS/sec	ROTOR SPEED R P M	STAGE HEAD, FT AIR COLUMN	MAXIMUM OVERALL EFFICIENCY	OVERALL PRESSURE RATIO	SMALL STAGE EFFICIENCY η_c	ROTOR TIP DIAMETER FT	ROTOR TIP SPEED FT/SEC	FLOW COEFFICIENT ϕ	REYNOLDS NUMBER $R_e \times 10^{-6}$	$\phi R_e \times 10^{-6}$	TIP MACH NUMBER	SPECIFIC SPEED OF ROTATION, N_s	LOAD FACTOR $\xi = \psi/\eta_c$
1	TURBINE PUMP		"POWER" MAY 1947	79 H_2O	1750	114500	38	5.15	48							0196	93.3
2	"		" " "	89 H_2O	3500	402150	38	4.580	50							0387	37.3
3	"		PUMPS" KRISTEL & ANNETT	229 H_2O	1750	50800	48	2.83	53							0504	19.90
4	LYSHOLM COMPRESSOR		BUSHIPS 338 VOL 14B	2.5	16080	10.070	48	1.38	50							0285	20.1
5	"		" " "	8.3	16000	10730	533	1.75	57							0381	29.2
6	ROOTS BLOWER	MARSHALL MARK 22 CABIN BLOWER	RAE REPORT ENG NO 4128	10.5	7000	8310	475	1.2	48							0322	31.0
7	"	ARGUS ENGINE SUPERCHARGER	BUSHIPS 338 VOL 14A	68	7000	3870	80	1.19	80							0383	25.3
8	"	ALLISON C3 SUPERCHARGER	RAE REPORT ENG NO 4128	45	3600	4815	835	1.2	835							0523	19.1
9	"	ALLISON C2 SUPERCHARGER	" " "	87	3600	3200	880	1.13	880							1011	9.89
10	CENTRIFUGAL COMPRESSOR	HERCULES SUPERCHARGER	ICE REPORT 1539	115	14700	13350	73	1.57	745	1.105	850	0308	8.01	185	708	154	6.50
11	"	MERLIN 46 SUPERCHARGER	RAE REPORT ENG NO 4103	238	25300	28690	78	2.48	780	804	1200	.0874	9.95	488	837	215	4.65
12	"	D.V.L. SUPERCHARGER	R.T.P. TRANSLATION 1944	125	14800	9850	72	1.40	80	850	864	.0725	3.80	291	584	203	4.93
13	"	DAIMLER-BENZ SUPERCHARGER	" " "	115	22000	17715	68	1.84	70	854	986	.0445	5.38	249	813	.1865	5.36
14	"	WEB COMPRESSOR	MAKERS' DATA	2220	16000	47000	78	4.0	77							297	3.48
15	"	IMPELLER A	NACA TECH NOTE NO 1313	384	19099	12700	78	1.73	80 *	1.00	780	.1034	8.04	821	743	384	3.78
16	"	" B	" " "	414	18150	15980	81	1.825	825 *	1.00	943	.1119	5.40	804	740	296	3.92
17	"	" C	" " "	325	15400	13800	80	1.68	815 *	1.00	810	.1164	5.18	580	844	244	4.11
18	"	CENTRIFUGAL COMPRESSORS TESTED BY BRUNO ECK	VENTILATOREN FIG 177	1376	1895	3890	775	1.165	780	4.53	450	.055	13.04	717	394	200	5.00
19	"		" FIG 178	330	3090	3240	73	1.115	73	2.53	410	.040	9.93	395	382	173	5.78
20	"		" FIG 180	120	8090	1030	80	1.037	80	925	395	.175	1.74	304	294	512	1.95
21	"		" FIG 181	39	2380	420	68	1.015	68	1.196	148	.070	1.12	078	.132	225	4.44
22	" *		" FIG 182	48	4585	1100	57	1.040	57	1.093	282	.080	1.82	109	234	240	4.17
23	"	SINGLE STAGE SULZER MEDIUM LIFT PUMP	SULZER TECH REVIEW NO 1947	2850 H_2O	1460	35200	765	2.27	79	888	33.5	038	3.2	122	<<1	200	5.00
24	AXIAL FLOW COMPRESSOR	BROWN BOVERI-ADDING SET NEUCHATEL STATION	BROWN BOVERI REVIEW VOL XXVII NO4	8230	3020	3390	865	4.38	80							.746	1.34
25	"	24 BLADE NACA COOLING FAN	NACA REPORT 729	818	3800	780	88	1.027	88	1.75	330	428	.1505	.0844	295	842	1.18
26	"	12 BLADE NACA COOLING FAN	NACA ARR NO 1132	831	3900	823	88	1.018	90	1.75	330	351	1183	0385	295	1.00	1.00
27	"	ARMSTRONG SIDDELEY A.S.X.	MAKERS' DATA	2780	8000	4375	855	5.81	89	1.713 †	718	828			842	817	1.08
28	"	METRO-VICKERS F2	"	2580	7400	4330	893	3.915	89	1.574 †	810	984	218	.1435	548	945	1.00 c
29	"	AXIAL COMPRESSORS TESTED BY BRUNO ECK	VENTILATOREN FIG 189				80	$\Psi = 1$	80	$\psi = .333$		.140				1.785	.504
30	"		" FIG 190				84	$\Psi = 2$	84	$\psi = .47$		250				1.478	678
31	"		" FIG 191				77	$\Psi = 5$	77	$\psi = .70$		370				.73	1.37
32	"	B M W P-3302	PERSONAL INFORMATION FROM PROF FAF SCHMIDT	1850	9000	5180	81	3.033	835 *	1.74 †	820	400	.175	.070	734	73	1.37
33	"	B M W 003A	U.S. AIR MAT COM TRANS NO FTS-1364-RE	2230	9500	5800	78	3.4	815	1.74 †	985	530	245	.130	775	.818	1.22
34	"	JUNKERS JUMO 004	AIRCRAFT ENGINES OF THE WORLD 1946	2580	8500	4485	60	3.0	830	1.07 †	742	378	228	.132	664	.980	1.04
35	"	PARSONS 23 STAGE BLAST FURNACE BLOWER	JOURNAL OF INST OF IRON AND STEEL VOL 158 P 104	725	6000	1860	84	3.04	860							.691	1.45
36	AIRSCREWS	HAMILTON 3155-8 SIX BLADES	NACA ARR NO 1123			$C_{P\,max}$ .0875	79	$C_{T\,max}$ .109	79	10.00	< 300		< 19.2		< .27	3.44	.391
37	"	HAMILTON 3155-8 EIGHT BLADES	" " "			" .0780	71	" .100	71	10.00	< 300		< 19.2		< .27	3.38	.295
38	"	HAMILTON 6130 THREE BLADES	U.S. ARMY AIR CORPS MAT DIV ACTR NO 4349		1000	" .0920	755	" .134	755	10.00	525		33.6		.47	3.81	.293
39	"	BUREAU AERONAUTICS 5868-8	NACA REPORT 842		1000	" .0580	720	" .142	720	10.00	525		30.8		.47	3.76	.270
40	"	HAMILTON 5101 THREE BLADES	U.S. ARMY AIR CORPS MAT DIV ACTR NO 4389		1000	" .0960	835	" .149	835	10.00	525		35.9		.47	3.55	.282
41	ANGULAR COMPRESSOR	HEINKEL-HIRTH HH DII	LILIENTHAL-GESELLSCHAFT BER 171	1120	9500	21350	833	2.07	850							.350	2.79

a PLOTTED .025 LOWER IN FIG 2 TO ACCOUNT FOR COLLECTOR CHAMBER LOSSES † ROTOR NO 1

surface excrescenses to a principal length—e.g., the blade chord. It is well known that a wide range of roughness profiles exists in which the various roughness profiles have a varying influence on the flow. It was found that, at high Reynolds Number, the friction coefficient for a rough surface is approximately independent of the Reynolds Number and depends chiefly on the roughness number, being proportionately greater with increasing relative roughness. On the other hand, at low Reynolds Numbers the friction coefficient is unaffected, within limits, by the surface quality and measured friction coefficients for surfaces of varying degrees of roughness agree closely with the values for a perfectly smooth surface. According to these results, therefore, a rough surface may be considered as perfectly smooth, as far as flow resistance is concerned, when the roughness elements are contained within the laminar part of the boundary layer. Since the thickness of the laminar boundary layer depends on the Reynolds Number, there exists a value of *Re* for a given value of *Ro*, below which the surface behaves as if it were smooth. In this range of Reynolds Numbers, therefore, the influence of roughness may be ignored. At greater Reynolds Numbers it must be taken into account.

An important standpoint from which the relative merits of various compressors may be assessed is that of efficiency. Rather than take the overall or the stage efficiency as a guide, the small stage efficiency η_∞ is considered in this paper as most suitable for comparative purposes. The small stage efficiency may be defined[11] as the ratio of the elemental work of compression to the elemental shaft input work and corresponds to the stage efficiency of a compresssor containing an infinite number of stages and producing the same overall pressure ratio as the compressor under consideration. It is related to the overall efficiency $\eta_{tot.}$, which includes irreversible losses through friction, throttling, leakage, etc., by the equation

$$\eta_{tot.} = [(p_{2i}/p_{1i})^{(\gamma-1)/\gamma} - 1]/[(p_{2i}/p_{1i})^{/(\gamma-1)/\gamma\eta_\infty} - 1] \tag{3}$$

For centrifugal and axial flow compressors η_∞ is a few per cent higher than the overall efficiency (see Table 1).

In the past, comparison of diverse groups of rotary machinery, such as hydraulic turbines, etc., has been made on the basis of specific speed as the measure of comparison. In the present examination a factor is used, hereinafter termed the *load factor*, which is defined as the inverse of the specific rotational speed[12] and given by the expression

$$l = (2gH)^{3/4}/2\sqrt{\pi}N\sqrt{Q} \tag{4}$$

In terms of the nondimensional compressor characteristics this becomes

$$l = \psi^{3/4}/\varphi^{1/2}(1 - \nu^2)^{1/2} \tag{5}$$

For centrifugal compressors the convention is followed of taking $\nu = 0$ in the definition of

$$\varphi = Q/[(\pi/4)D^2(1 - \nu^2)u]$$

so that in this case $l = \psi^{3/4}/\varphi^{1/2}$ where

$$\varphi = Q/[(\pi/4)D^2u]$$

Comparing Eqs. (1), (2), and (5) we have

$$\eta_\infty = f_3(l, Re, M, Ro) \tag{6}$$

This equation illustrates the main influences affecting the performance characteristics of rotary compressors and affords a basis for the statistical analysis of measured results. It is, however, only an approximate representation of actual conditions, since it neglects to take into account the lack of similarity in tip clearance losses, boundary-layer formations, etc., which occur in practice between compressors of the same type. In addition to these effects, a further error is introduced in the final analysis by the neglect of similarity in mechanical losses. It is well known that similarity of bearings and lubrication is entirely different from the hydraulic similarity of compressors and is governed by further nondimensional parameters. Because of the lack in the available experimental data of the information required to include this effect and because of its relatively small influence on the main process of compression, lack of mechanical similarity has been disregarded in the results presented in this paper, and a small stage efficiency based on an overall efficiency including mechanical losses has been used.

The available data, which are considered sufficiently reliable to enable conclusions to be drawn with reasonable confidence as to their accuracy, are tabulated in Table 1. Where possible, the relevant values of the Reynolds and tip Mach Numbers have been included. For the centrifugal compressors the Reynolds Number is based on impeller tip speed (considered a sufficiently close approximation to the actual relative fluid velocity at the impeller tip) and the tip diameter. Given an infinite number of data for each compressor type, Eq. (6) requires, for its adequate representation, an infinite series of three-dimensional surfaces for every value of the fifth variable. In practice, the data available are severely limited in number and have been represented two-dimensionally in Fig. 2 by plotting the small stage efficiency η_∞ against the load factor l for each type of compressor without discrimination of the variation of the other variables in each system. The true variation of η_∞ with l at constant values of the other parameters, for each system of common compressor type, is therefore obscured by a certain amount of scatter, the magnitude of which to a certain extent can be judged from the tabled values of these parameters and the foregoing remarks concerning their influence. Such judgment or reasoned estimation has been exercised in drawing the curves individual to each system through the scattered points.

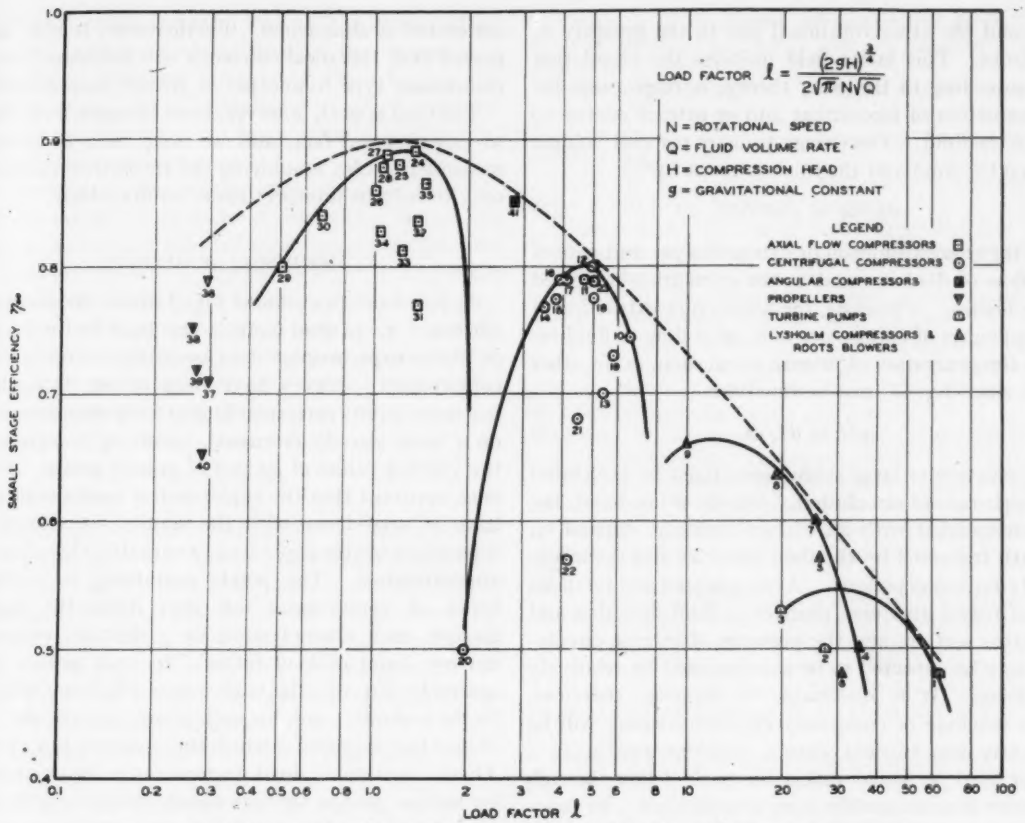

FIG. 2. Variation of the small stage efficiency with the load factor of rotary compressors.

Until now, the discussion has been concerned only with individual systems (namely, particular types of rotary compressors) involving a certain degree of similarity within themselves. It is perhaps relevant here, before discussing the implications of Fig. 2, to examine briefly the theoretical grounds for differences between the separate systems—i.e., to extend the analysis to include the comparison of one system (compressor type) with another. All types of compressors have a common fundamental characteristic—namely, the addition of energy to a gas stream. The efficiency with which this process is effected is intimately bound up with the compressor type insofar as the flow path and attendant opportunities for irreversible loss vary from one type to another.

ENERGY ADDITION TO A FLUID BY A ROTOR

The first clear presentation of the theory of operation of rotary machinery was given by Zeuner[13] in 1899. This theory is the well-known hydraulic or filament theory postulating a steady and uniform flow through the machine. The assumption of steady flow implies an independence of time for the fluid flow and the energy transfer between rotor and fluid. The condition of uniformity implies that every fluid filament enters and leaves the machine under similar conditions. Thus the velocity at entrance is the same for all fluid filaments— that is, the velocity is uniform in direction and magnitude over the plane of entrance. Similar conditions apply at the exit. These assumptions imply conditions from which there is, in practice, considerable deviation. The theory, however, has been widely used in the design of rotary compressors, although recent advances in aerodynamics and gas dynamics have contributed new concepts to its refinement. Keller[14] investigated the transient and periodic fluctuations that invalidate the assumption of steady flow. These periodic phenomena have been shown to induce premature choking and to have detrimental effects on the flow quantity.[15] The assumption of uniform flow ignores the velocity and pressure distributions set up by the rotor blades and the presence in actual machines of extensive blade, hub, and casing boundary layer.

Further important contributions to the refinement of the original approximate theory have been made by Müller,[16, 17] Spannhake,[18] and others, according to which the flow in the rotor outside the blades is not considered as vortex-free. As in the case of the airplane wing, the blades are considered as discontinuities in the velocity field and may be replaced by a vortex distribution.[17] The absolute velocity field may then be analyzed into two fields—one uniform and irrota-

tional and the other rotational due to the presence of the blades. This latter field includes the circulation that, according to the wing theory, is responsible for the production of forces that add or extract energy to or from the fluid. The energy transfer per unit volume between the fluid and the rotor is given by[17]

$$dL/dq = \rho(d\Gamma/dt) \tag{7}$$

Thus, the energy addition or extraction per unit rate of mass flow of fluid is equal to the circulation produced by the blades. Therefore, the addition or extraction of large amounts of energy per unit mass flow of fluid requires the generation of intense circulation, or, in other words, since Eq. (7) can be rewritten

$$gH = d\Gamma/dt \tag{8}$$

the production of large stage heads must be associated with high rate of circulation. On the other hand, the losses associated with an energy exchange depend on the path traversed by the fluid particles and the intensity of circulation present. A complicated and tortuous path of travel involving changes of fluid direction and fluid cross section, and the presence of intense circulation, may be expected to be accompanied by relatively high losses. It is reasonable to suppose, therefore, that a machine of comparatively high loading will be inherently less efficient than a machine producing a smaller head per stage, unless the path of flow through the latter is considerably more complicated. In practice, high stage heads and flow path complication go hand in hand. Thus, in the turbine pump, the fluid completes a full circle in its travel while suffering a continuous series of impacts from successive vanes with the consequent generation of intense circulation. The delivery head is high (see Table 1). In the centrifugal compressor the loading is lower, and the fluid path, although involving at least two 90° bends and considerable change in flow area, is less complicated. The fluid particles are acted upon by the blades only in the relatively short distance of their travel from the impeller eye to the impeller tip, with a consequently smaller generation of circulation and vorticity. In the axial-flow compressor with a comparatively small energy transfer per stage the circulation is lower still, and, furthermore, the flow path is comparatively direct and uncomplicated.

There are grounds for expecting therefore that, in practice the turbine pump will be inherently and inevitably less efficient than the centrifugal compressor, which in its turn will be similarly less efficient than the axial-flow compressor.

Elaborating this statement, it is reasonable to suppose that there exists an upper limit to the efficiency of a particular type of compressor which is intimately bound up with the nature of that compressor.

This efficiency represents an ideal efficiency, greater values than which are impossible to achieve in practice unless the particular compressor type with which it is associated is abandoned. Furthermore, it is to be expected that this ideal efficiency will decrease from one compressor type to another of greater stage loading.

The final appeal, however, must be made from theory to experimental fact, and we must turn to recorded, measured results, employing the theoretical indications only to help us interpret these results wisely.

Discussion of Results

As previously mentioned Fig. 2 shows the small stage efficiency η_s plotted against the load factor l for the available experimental data covering various types of compressors. Curves have been drawn through the scattered points corresponding to each compressor type on a basis already discussed, involving recognition of the varying values of Re and M in each group. It is at once apparent that the experimental points tend to behave in accordance with the simple, theoretical considerations of this paper to a remarkably close degree of approximation. The points pertaining to particular types of compressors fall into distinctly separate groups, each characterized by a definite, reasonably narrow, band of load factor. In each group, as required by Eq. (6), the variation of efficiency with load factor is similar, and, for each group, a particular value of load factor exists for which the efficiency is maximum. These "optimum" load factors range from about 40 for turbine pumps, through about 20 for rotary displacement blowers, 5 for centrifugal compressors, to about 1 for axial flow compressors. Also, in accordance with the indications of the previous section, the maximum efficiency increases from one compressor type to another of lower characteristic load factor. In view of this excellent correlation with theoretical considerations, it is considered that the practical ideal efficiency corresponding to a given compressor type, the existence of which was mooted in the previous section, may in fact be a real concept, and the authors have ventured to include in Fig. 2 an envelope curve representing their considered opinion, based on the experimental evidence, of the variation of this ideal efficiency between various types of compressor. It is at once obvious, if this curve is accepted, that the axial-type compressor offers the greatest possible returns for development and appears to have a margin of efficiency in hand over its nearest rival, the centrifugal compressor, of approximately 10 per cent.

For completeness, points have been included to represent the propeller. For this group the efficiency variation with load factor is obscure. This efficiency, for the sake of a consistent comparison, has been taken to be the aerodynamic efficiency of the propeller under static conditions, given by

$$\eta_{\text{aero.}} = \sqrt{2/\pi}\,(C_T^{3/2}/C_P) \tag{9}$$

where C_T and C_P are the usual thrust and power coefficients, measured under static conditions. Although

the envelope curve has been extended to include these points, it is perhaps doubtful whether they represent a specific type of rotary compressor distinct from the axial-flow type. It is interesting to note, however, that they are characterized by a definite load factor, which is of the order of 0.3.

The position of the point representing the Heinkel-Hirth-Oll angular compressor is interesting in that, as would be expected, it falls between the centrifugal- and axial-type groups with a load factor of 2.8. As a point of interest, the load factor of the D.V.L. supersonic compressor[19] was computed to be 2.3. It was not included in Fig. 2, however, as being unrepresentative because of the very low efficiency resulting from fundamental errors in its design.

Conclusions

Every type of rotary compressor is characterized by a distinct, relatively narrow, band of load factor.

For each type of rotary compressor a particular load factor exists for which the efficiency is a maximum.

The maximum efficiency is intimately linked with the nature of the particular type of compressor and increases from one type of compressor to another of lower characteristic load factor.

On the basis of recorded, measured results, the axial-flow compressor would appear to be, currently, more efficient than the centrifugal type, to the extent of about 10 per cent.

References

[1] Samaras, D. G., *Thermodynamic Performance Considerations of Jet Propulsion*, National Research Council of Canada Report ME-57, February, 1942.

[2] Samaras, D. G., *Present Achievements and Future Developments in Aircraft Gas Turbine Engines*, Engineering Journal, July, 1946.

[3] Weber, M., *Die spezifische Drehzahlen und die anderen Kenngrösser der Wasserturbinen, Kreiselpumpen, Windräder und Propeller als dimensionsfreie Kenngrössen der Ähnlichkeitsphysik*, Schiffbau, Bd. 31, 1930.

[4] Sörensen, E., *Hydraulische Ähnlichkeit von Dampfturbinenstufen*, Z.V.D.I., Bd. 78, Nr. 48, December, 1934.

[5] Hablützel, E., *The Law of Similitude for Flow Problems, Its Experimental Verification and Application to Mechanical Engineering*, Sulzer Review, No. 1, 1947.

[6] Eckert, B., *Ähnlichkeitsbetrachtungen an Strömungmaschinen für Gase*, Luftfahrtforschung, Bd. 18, H. 11, 1941.

[7] Eckert, B., *Überblick über Forschungsergebnisse des Forschungsinstituts für Kraftfahrwesen und Fahrzeugmotoren, Stuttgart, an axial durchströmten Verdichtern*, Lilienthal Gesellschaft für Luftfahrtforschung, Bericht 171, 1943.

[8] Encke, W., *Axialverdichter*, Lilienthal Gesellschaft für Luftfahrtforschung, Bericht 171, October, 1943.

[9] Relf, E. F., *Experiments on the Effects of Surface Roughness*, Fifth International Congress of Applied Mechanics, 1938.

[10] Sörensen, E., *The Effect of Wall Roughness on the Performance of Turbo-Machinery*, Forschung, Vol. 8, No. 1 (R.T.P. Trans. 1550) 1937.

[11] Samaras, D. G., *Isentropic efficiency factor of cooled frictional compression*, R.A.E. Tech. Note Eng. 231, December, 1943.

[12] Eck, B., *Ventilatoren;* Berlin, 1937.

[13] Zeuner, G., *Theorie der Turbinen;* Leipzig, 1899.

[14] Keller, C., *Kinetic Energy Losses Behind Blade Grids As Result of Periodic Variation in the Circulation*, R.T.P. Trans. 1883, 1934.

[15] Samaras, D. G., *Choking Effects in an Oscillating Flow* (unpublished), 1947.

[16] Müller, W., *Allgemeine Sätze über die Strömung in Kreiselradern und Turbinen*, Z.A.M.M., Bd. 7, H. 5, October, 1927.

[17] Müller, W., *Wirbelschichten und Zirkulationen*, Zeit. f. Techn. Physik, 1924.

[18] Spannhake, W., *Dreidimensionale Turbinentheorie und Prandltsche Tragflügeltheorie*, Fifth International Congress of Applied Mechanics, 1938.

[19] Weise, A., *Überschallaxialverdichter*, Lilienthal Gesellschaft für Luftfahrtforschung, Bericht 171, October, 1943.

Notice to Contributors

Manuscripts submitted for publication *must* be double- or triple-spaced originals. There should be wide margins on both sides of the sheets and triple spacing around formulas to allow for the marking of directions for the printer.

Original drawings (jet black India ink on white paper or tracing cloth) should accompany the manuscript. *(Blueprints are not acceptable.)* Photographs *must be* on glossy white paper.

Only the simplest formulas should be typewritten; all others should be carefully written in pen and ink. The difference between capital and lower-case letters and Greek symbols should be clearly distinguished.

See the Inside Back Cover of this issue for further details.

Services of the Libraries of the Institute of the Aeronautical Sciences

The services of the Libraries are available to all members of the Institute, to Corporate Members, to advertisers in the AERONAUTICAL ENGINEERING REVIEW and AERONAUTICAL ENGINEERING CATALOG, and, under usual library limitations, to the public. Four specialized services are available.

The Paul Kollsman Lending Library

This lending library service makes available, *without charge*, the latest and more important aeronautical books.

Members may request the loan of any aeronautical or technical book they wish to borrow. Through an exchange agreement with the Engineering Societies Library, any book on general engineering may be borrowed from its great collection of over 160,000 volumes.

A photostating service is available at usual library rates.

Applications for membership in the library and further information will be sent on request.

The W. A. M. Burden Reference Library

This reference library contains over 12,000 aeronautical books, magazines, pamphlets, and reports gathered from world-wide sources and is one of the most complete aeronautical libraries in the world. Material from this library is not available for loan but may be used for reference purposes.

The Pacific Aeronautical Library

6715 Hollywood Boulevard
Los Angeles 28, California

Established in cooperation with the aircraft companies the library serves. The leading aircraft companies in or near Los Angeles participate in its support and operation.

This service library for aeronautical research is available to the public for reading privileges. Source material includes aerodynamic and structural research reports, as well as books on drafting, production methods, history, and allied sciences. It furnishes books, periodicals, and pamphlet material to the participating aircraft companies to supplement their engineering libraries.

Technical Information Service

This service has experienced personnel under the supervision of trained aeronautical engineers to compile any information desired. The services range from listing specialized reference books to the preparation of exhaustive bibliographies, digesting of reports, and general surveys of any aeronautical subject. Some of the available services are:

Bibliographies on any aeronautical subject.
Reports on any aeronautical subject.
Digests of aeronautical books, papers, periodicals, and references.
Translations.
Engineering investigations of special aeronautical subjects.
Biographies of individuals engaged in aeronautics.
Photostats of any aeronautical or general engineering material.
Microfilms made on special order.
Photographs made from the Institute's photographic collection.
Drawings and tracings made.

In addition to the services mentioned any commission which comes within the scope of the Service will be accepted. Special arrangements may be made for work requiring several weeks or months.

Translators are available for accurate transcriptions of all foreign language data. Translations are carefully edited by trained engineers.

Reproductions of any material in the collections of the Institute may be ordered at standard photostat rates.

INSTITUTE OF THE AERONAUTICAL SCIENCES, INC.

2 EAST 64TH STREET, NEW YORK 21, N.Y.